Flexible piezoelectric composites
Bridging the gap between materials and applications

Deutz, Daniella

DOI
10.4233/uuid:3ed1b44e-44f4-4b84-abd1-34722d106c22

Publication date
2017

Document Version
Final published version

Citation (APA)
Deutz, D. (2017). *Flexible piezoelectric composites: Bridging the gap between materials and applications*. [Dissertation (TU Delft), Delft University of Technology]. https://doi.org/10.4233/uuid:3ed1b44e-44f4-4b84-abd1-34722d106c22

FLEXIBLE PIEZOELECTRIC COMPOSITES

BRIDGING THE GAP BETWEEN MATERIALS AND APPLICATIONS

FLEXIBLE PIEZOELECTRIC COMPOSITES

BRIDGING THE GAP BETWEEN MATERIALS AND APPLICATIONS

Proefschrift

ter verkrijging van de graad van doctor
aan de Technische Universiteit Delft,
op gezag van de Rector Magnificus prof. ir. K. C. A. M. Luyben,
voorzitter van het College voor Promoties,
in het openbaar te verdedigen op vrijdag 27 oktober 2017 om 12:30 uur

door

Daniella Bayle DEUTZ

Ingenieur Luchtvaart en Ruimtevaart,
Technische Universiteit Delft, Delft, Nederland,
geboren te Charleston, South Carolina, Verenigde Staten van Amerika.

Dit proefschrift is goedgekeurd door de

promotors: Prof. dr. W. A. Groen en Prof. dr. ir. S. van der Zwaag

Samenstelling promotiecommissie:

Rector Magnificus	voorzitter
Prof. dr. W. A. Groen	Technische Universiteit Delft
Prof. dr. ir. S. van der Zwaag	Technische Universiteit Delft
Onafhankelijke leden:	
Prof. dr. D. M. de Leeuw	Universiteit Groningen
Prof. dr. ir. J. R. van Ommen	Technische Universiteit Delft
Prof. dr. M. Zeman	Technische Universiteit Delft
Dr. S. Fritsch	Universit*é* Paul Sabatier, Frankrijk
Overig lid:	
Dr. ir. E. Tempelman	Technische Universiteit Delft

Printed by: ProefschriftMaken || www.proefschriftmaken.nl

Front & Back: Bregje Jaspers

This project has received funding from the European Union's Seventh Framework Programme for research, technological development and demonstration under grant agreement no 310311.

ISBN 978-94-6295-722-0

An electronic version of this dissertation is available at
http://repository.tudelft.nl/.

To Jelmer

Forever - is composed of Nows
'Tis not a different time
Except for Infiniteness
And Latitude of Home

From this – experienced Here
Remove the Dates – to These
Let Months dissolve in further Months
And Years – exhale in Years

Without Debate – or Pause
Or Celebrated Days
No different Our Years would be
From Anno Dominies

Emily Dickinson

CONTENTS

1

INTRODUCTION

The good thing about science is that it’s true whether or not you believe in it.

Neil deGrasse Tyson

1.1. THE RISE OF PIEZOELECTRICITY

MICROPHONES, parking sensors, quartz watches, fuel injectors and inkjet printers all rely on the remarkable phenomenon known as the piezoelectric effect, found in various crystals, ceramics, polymers and even in bone. It was discovered in 1880 by French physicist Pierre Curie, working with his older brother Jacques, who discovered that putting pressure on these materials generates electricity (the name comes from ’$\pi\iota\epsilon\zeta\epsilon\iota\nu$’, Greek for squeezing or pressure).

1.1.1. THE PIEZOELECTRIC EFFECT

Pierre Curie started conducting chemistry experiments at the age of 20 with Jacques, focusing on the structure of crystals. The Curie brothers suspected the key to piezoelectricity was crystal asymmetry, and would only be found in materials with non- centrosymmetric crystal structures. They tested any crystals they could get their hands on, including quartz, topaz, cane sugar, rochelle salt, and tourmaline. To pick up the tiny, 10^{-12} C, range piezoelectric charges they invented the Piezoelectric Quartz Electrometer, which Marie Curie would use in the 1890’s to aid her discovery of radioactivity. Their hunch turned out to be right. Armed with the electrometer they soon uncovered the ***direct* piezoelectric effect**, by which non-centrosymmetric, piezoelectric materials convert mechanical energy into electrical energy:

$$D = dT + \epsilon^T E \tag{1.1}$$

for a non-zero electric field E, where D is the electric displacement, d represents the piezoelectric charge coefficient, T is the applied mechanical stress, and ϵ^T is the relative permitivitty or dielectric constant of the material under constant stress, T [1].

Intrigued by the discovery, the mathematician Gabriel Lippman went on to demonstrate that there should be a *converse* piezoelectric effect [2], linking an applied electric field to a deformation of the crystal. The Curie brothers rushed to test Lippman's theory, and their experiments confirmed that piezoelectric materials can also convert electrical energy into mechanical energy, according to the ***indirect*** **piezoelectric effect**:

$$S = s^E T + dE \tag{1.2}$$

for a non-zero external mechanical stress, where S is the strain and s represents the compliance of the piezoelectric material under constant field E.

For the next 30 years or so there was little interest in piezoelectricity. It was obscure even among crystallographers, the theory was prohibitively mathematically complex, and no publicly visible applications had been found for any of the piezoelectric crystals the Curie's identified. Like many scientists at the time, Pierre Curie moved on to investigating electro-magnetism, yet he did uncover one more process integral to piezoelectricity; the effect of temperature on paramagnetism and paraelectricity now known as *Curie's law* and the **Curie temperature** (T_C [°C]): the critical temperature at which ferromagnetic materials cease to be ferromagnetic and ferroelectric materials cease to be ferroelectric.

1.1.2. FIRST PRACTICAL APPLICATION

Piezoelectric materials finally took off just after World War I with sonar, when Paul Langevin developed an ultrasonic transducer for use on submarines based on thin quartz crystals (Fig. 1.1). The quartz crystal resonates and emits a high frequency 'chirp' underwater, and by timing the return signal, the ocean depth or ping distance is measured.

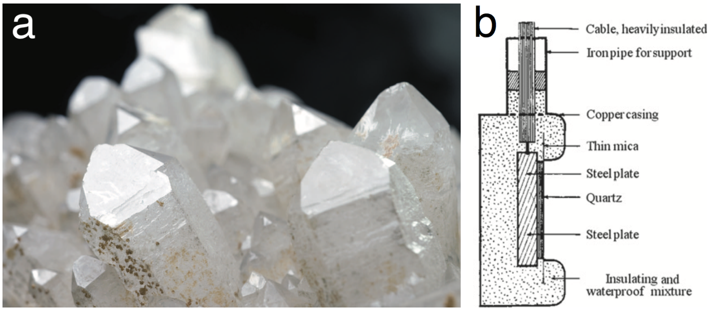

Figure 1.1: First practical application of a piezoelectric crystal. (a) Quartz crystal in its natural form [3]. (b) Cross-sectional view of a form of quartz transducer designed by Boyle and Langevin in 1917, as recorded in the BIR (Board of Invention and Research) document 38164/17.

Though the **mechanical quality factor**, Q_m, of quartz is rather high (indicating low mechanical loss), quartz had two major drawbacks. The first is its low conversion efficiency from mechanical to electrical energy, and vice versa, defined as the **electromechanical coupling**, or k:

$$k^2 = \frac{stored\ electrical\ energy}{input\ mechanical\ energy} = \frac{stored\ mechanical\ energy}{input\ electrical\ energy}. \qquad (1.3)$$

Second, Brazil was the only nation with access to natural quartz crystals. US researchers soon switched to Rochelle salt, or sodium potassium tartrate ($NaKC_4H_4O_6 \cdot 4H_2O$), crystals which have an electromechanical coupling close to 100 % at room temperature, and are easy to grow in any well-equipped kitchen. Brazilians had the last laugh, though, since devices based on Rochelle salt rapidly degrade in humid air due to the crystal's extreme water solubility.

1.1.3. FERROELECTRICITY AND PEROVSKITES

The next giant leap for piezoelectricity would not come around until World War II, when the urgent need for improved ceramic capacitors would launch researchers from the US [4], Japan [5], and Russia [6] to independently discover barium titanate ($BaTiO_3$, BT) ceramics. They had unwittingly discovered a new class of materials called **ferroelectrics**: a subset of piezoelectric materials in which the orientation of the spontaneous polarization can be flipped by application of high electric fields in a process called **poling**. These man-made ferroelectrics exhibit orders of magnitude higher piezoelectric charge coefficients, d, than any naturally occurring material. The key here, was the TiO_2 based perovskite crystal structure of BT.

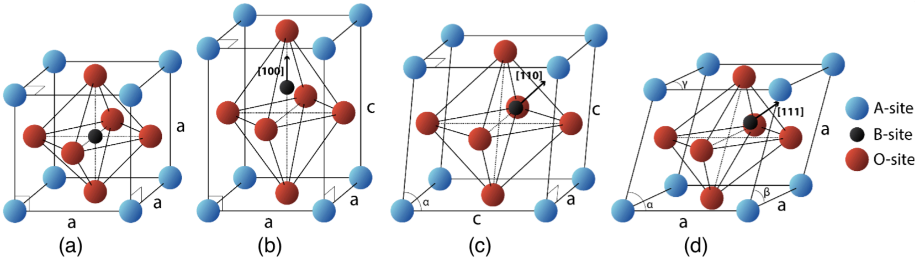

Figure 1.2: Perovskite crystal structure in its four common states [7], adapted from Holterman and Groen 2013 [3]. A-site cations are indicated in blue, O-site anions in red and B-site cations in black. Polarization directions are indicated, per crystal state, by the black arrow on the B-site ion and the matching hkl-index. (a) Paraelectric cubic state, above the Curie temperature, with B-site ion trapped in the center. (b) Tetragonal state: B-site ion can flip to a face. (c) Orthorhomic state: B-site ion can flip to an edge. (d) Rhombohedral state: B-site ion can flip to a corner.

The perovskite crystal structure is named after the $CaTiO_3$ mineral originally found in the Ural Mountains of Russia by Gustav Rose in 1839 and is named after Russian mineralogist Lev Perovski. Perovskites have a general formula of ABO_3, shown in Fig. 1.2. The A-site cations, in the corners of the lattice, usually have a larger atomic radius than the B-site cations, in the center of the lattice. The direction the B-site cation settles into depends on the phase of the crystal, and indicates the orientation of the spontaneous polarization of the unit cell.

The phase of a perovskite crystal depends on its composition and temperature. For instance, BT has a centrosymmetric, cubic structure at temperatures above its Curie point at 120 °C (shown in Fig. 1.2a) and can not be poled. Below 120 °C, BT transforms into a tetragonal structure (Fig. 1.2b), until at 0 °C (Fig. 1.2c) it transforms into an orthorhombic structure, before finally settling on a rhombohedral structure below -80 °C (Fig. 1.2d). Tetragonal crystals can be poled in 6 directions, while orthorhombic crystals can be poled in 12 directions and rhombohedral in 8 directions. As a general rule, it is easier to pole a crystal if it has more available poling states.

In perovskite crystals the tensor of the **piezoelectric charge coefficient**, d, reduces to only three terms, due to symmetry: the longitudinal mode, d_{33}, transverse mode, d_{31}, and shear mode, d_{15}, (Fig. 1.3). The absolute values of these coefficients follow a specific order: $d_{15} > d_{33} >> |d_{31}|$ [8–10]. The piezoelectric response in compression or tension, d_{33}, and bending, d_{31}, are coupled, as they rely on the same input/output parameter E_3. The d_{15} shear mode is larger than the d_{33} since the oxygen octahedron in the perovskite can rotate much more easily than it can stretch or squeeze [11–13].

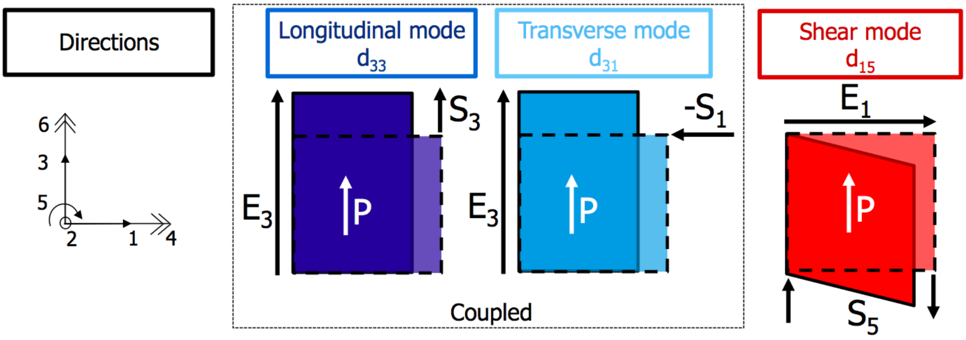

Figure 1.3: Operation modes of a perovskite piezoelectric material, adapted from Holterman and Groen 2013 [3]. From left to right: Conventional piezoelectric definitions of the 3 (xyz)-directions and 3 rotations over the (xyz)-directions. Graphical representations of the coupling between: the extension in 3-direction, S_3, due to an applied field E_3, described by d_{33}, the compression in 1-direction, S_1, due to an applied field E_3, described by d_{31}, and the extension due to rotation in 5-direction, S_5, due to an applied field E_1, described by d_{15}.

Piezoelectric BT ceramics are non-water soluble and have reasonably high coupling coefficients around 40 %, but the shortcomings remained. Ferroelectric materials can only be used up to about half of their Curie temperature without losing polarization. Around secondary transitions their electrical properties are also largely dependent on the temperature. For BT, this meant it could only be reliably used between 20 and 60 °C. To increase the Curie temperature higher than 120 °C, and decrease the second transition temperature, from tetragonal to orthorhombic, below -20 °C, many different cation replacements, such as Pb and Ca, were studied. From these trials, a new system, PZT, was discovered.

1.1.4. DISCOVERY OF PZT AND KNLN

In 1952, physicists at the Tokyo Institute of Technology developed $PbZr_{0.48}Ti_{0.52}O_3$ (PZT), an easy to manufacture ferroelectric ceramic combining high piezoelectric coefficients with increased temperature stability [14]. The material was discovered by Sawaguchi *et al.*, but the discovery of its superior piezoelectricity was conducted by Bernard Jaffe in 1955 [15]. Jaffe was at the US National Bureau of Standards at that time. He knew about Sawaguchi's serial studies on the PZT system, and focused on the composition range near the **morphotropic phase boundary** (MPB), where the tetragonal and rhombohedral phases coexist (Fig. 1.4). The electromechanical coupling, k, and dielectric constant, ε_r, around the MPB composition range skyrocket due to the availability of both the tetragonal poling states and the rhombohedral poling states. In 1971 he published the seminal book on *Piezoelectric Ceramics* still in use today, with colleagues W. R. Cook Jr. and H. Jaffe (no relation) [9]. The lead-based perovskites have since been doped with metallic impurities to achieve even better properties, tailoring: the ease of poling, dielectric constant, piezoelectric coupling coefficients, mechanical quality factor and material stiffness.

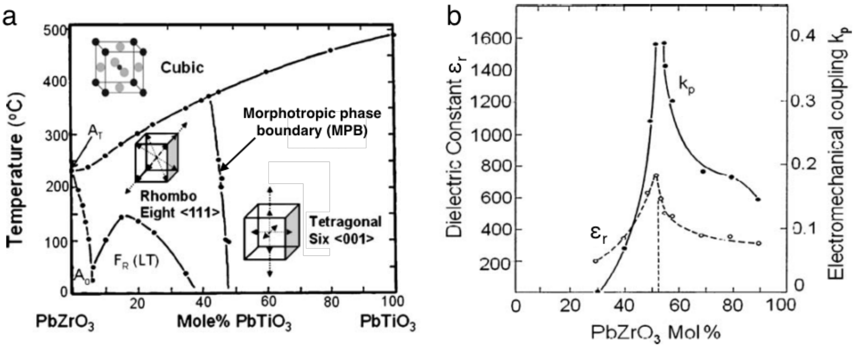

Figure 1.4: Morphotropic phase boundary in PZT. The phase diagram between PZ and PT as a function of temperature (a), and the dielectric constant, ε_r, and electromechanical coupling, k, (b) [9].

Despite its very useful properties, alternatives to PZT have been sought because it contains more than 60 wt.% of lead. The European Community explicitly limited the usage of lead in electronic equipment in 2006 in the 'Restrictions on the use of certain Hazardous Substances' (RoHS). The most commonly studied lead-free piezoelectric ceramics since, can be split into three groups; (Ba, Zr, Ca)TiO_3 (BZT-BCT), (Na, K)NbO_3 (KNN), and tungsten bronze (TB), all of which are based on materials discovered, but disregarded in favor of PZT, in the 1970's [16–22]. One of the most promising replacements for high performance PZT was developed in 2004 by Saito and Takao [23], this time on a **polymorphic phase transition** (PPT), a temperature dependent phase boundary, between two orthorhombic phases and one tetragonal phase. The lead free (KNLN) $(K_{0.5}Na_{0.5})_{(1-x)}Li_xNbO_3$, often also doped with Ta to decrease sensitivity to moisture, combines a significant piezoelectric effect with a T_C of over 400 °C.

1.1.5. PIEZOELECTRIC POLYMERS AND POLYMER COMPOSITES

Although PZT and KNLN are generally superior, due to their high density (7.9 and 4.5 cm^3, respectively) and acoustic impedance mismatch with water, flexible and light weight transducers were sought for underwater and medical acoustic monitoring. In the 1960's, researchers discovered a miniscule piezoelectric effect in both whale bone and tendon [24]. This began an intense search for other organic materials that might exhibit piezoelectricity. In 1969, Kawai [25] discovered that polarized β-phase polyvinylidene fluoride (PVDF) was ferroelectric. While other polymers, like nylon and polyvinylchloride (PVC) also exhibit the effect, none can outperform PVDF, which has d values on the order of 20 pC/N. Piezoelectric PVDF and its random copolymer with trifluoroethylene (P(VDF-TrFE)) are now the most widely studied [26, 27], commercially available [24], piezoelectric polymers.

Not fully satisfied with the complex stretching processing required to induce a piezoelectric effect in PVDF and the small piezoelectric charge constants, d, researchers in the 1970's turned to **piezoelectric composites**, a combination of an active piezoelectric ceramic filler in a passive polymer matrix. The first paper on a piezoelectric composite seems to be from Kitayama and Sugawara in 1972 [12, 28]. They prepared a hot-rolled composite made of active PZT powder mixed into a PVDF polymer matrix, and showed that the piezoelectric performance significantly improved with respect to PVDF, while the composite remained formable and flexible.

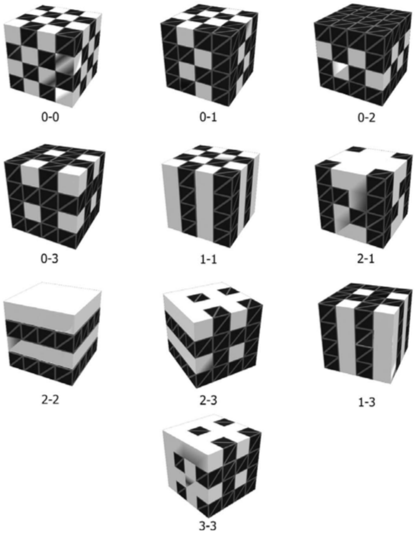

Figure 1.5: Connectivity families for two phase composites. The polymer phase is shown in black, while the piezoelectric ceramic phase is shown in white. Note that the total number of connectivity patterns is 16 (rather than 10) due to permutations involved in families: (1-0), (0-2), (0-3), (2-1), (2-3), (1-3) (Copyright IEEE 2005 [29], adapted from [30]).

The first composites were all ‘random’, or ‘0-3’, consisting of randomly dispersed piezoelectric ceramic particles in a polymer matrix [30–35]. Random composites are hardly piezoelectric when compared to piezoelectric ceramics, as an applied electric field is confined by the low dielectric constant, ε_r, of the polymer matrix. Changing the arrangement of the filler by, for instance, using continuous fibers instead of disparate particles, can drastically improve the d of the composite up to the value of the constituent ceramic [36]. These fiber composites are used today in fish finders, underwater sonar devices, and medical diagnostics, such as prenatal ultrasounds.

To prevent confusion in composite research, Robert E. Newnham and his group at Penn. State University [30] established a method to describe the 10 possible ways two phase composites can be arranged (Fig. 1.5). The connectivity of the composite is described by two digits: ‘X-Y’, where the X, for the active filler phase, and Y, for the passive matrix phase, indicate in how many dimensions (from 0 to 3) each phase is self-connected. Newnham’s group at Penn. State was also the first to characterize sum, combination, and product effects in piezoelectric composites [30]. A noteworthy combination property is g, the **piezoelectric voltage coefficient** and figure of merit for sensing, defined as $d/\varepsilon_r \cdot \varepsilon_0$, where $\varepsilon_0 = 8.854 \cdot 10^{-12}$F/m is the permittivity of free space. In (quasi) 1-3 composites, g follows the convex and concave type sum effects of d and ε_r, respectively, leading to a g which is higher in the composite than in either phase on its own.

In applications that require flexibility, such as wearable electronics, rigid 1-3 composites and ceramics can be unwieldy. A suitable alternative for this material selection problem can be found in quasi 1-3, or **dielectrophoretically structured composites** [37–40]. By applying an oscillating electric field on the viscous, uncured 0-3 composite, the piezoelectric ceramic filler particles align in chain like structures parallel to the applied field (Fig. 1.6). The system can exhibit a large g_{33} value at low volume fractions of filler, at which the ductility and stiffness of the matrix dominate. The Curie temperature remains, in first order approximation, that of the ceramic filler. The main drawback is that the voltage coefficient lags behind that of PVDF and of P(VDF-TrFE).

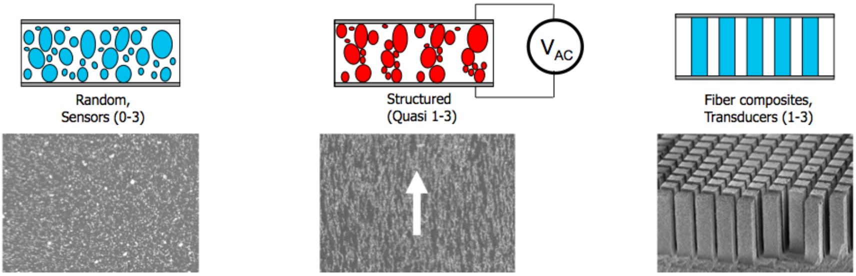

Figure 1.6: Graphical representations (above) and scanning electron micrographs (below) of random composites, structured composites and the ceramic pillars used in 1-3 composites. In the micrographs of the random and structured composites, the polymer matrix is grey while the piezoelectric filler particles are white. Micrograph of the diced ceramic for the 1-3 composite is adapted from Holterman and Groen 2013 [3]

1.1.6. ENERGY HARVESTING WITH PIEZOELECTRIC MATERIALS

The ability to deliver sustainable power to a wireless sensor network is attractive as it eliminates the time and cost of replacing batteries. This holds especially for networks that are either inhospitable or difficult to reach, such as structure-embedded microsystems and medical implants. The most attractive energy source is that of ambient mechanical vibrations, such as human motion, kitchen appliances and car engines. There are various methods to harvest the mechanical energy but, for small electronic harvesters, below a volume of about 1 cm^3, the power density for piezoelectric energy harvesting exceeds that for electromagnetic and electrostatic generators [41–43]. This means that with the ongoing decreasing power consumption of integrated circuits, autonomous microsystems based on piezoelectric energy harvesting come within reach [44]. Even though ceramics and single crystals demonstrate excellent piezoelectric charge coefficients, d, (Fig. 1.7), they have a high stiffness, and are inherently brittle, making it difficult to directly assemble them into the required structures. Piezoelectric PVDF exhibits a state-of-the-art piezoelectric voltage coefficient, g, of about 200 mV.m/N. However, the low Curie temperature, which for the commonly used copolymer P(VDF-TrFE) (65/35) is only 100 °C, severely limits its useful temperature range. High values of the voltage coefficient have also been reported for ferroelectret polymers, *i.e.* soft electroactive films [45–47], but applications are hampered by discharging at elevated temperature [48]. Recently, there has been a flurry of exciting research into flexible and lead free piezoelectric composite materials [49–56]. Possible applications range from tire pressure monitoring systems (TPMS) [57], to sensors for structural health monitoring (SHM) [58], and biocompatible energy harvesters [59]. However, at present, the search continues for composites with adequate **figure of merit (FOM)** for energy harvesting, dg, matched with mechanical ductility and low stiffness, that are simple to prepare at high volume.

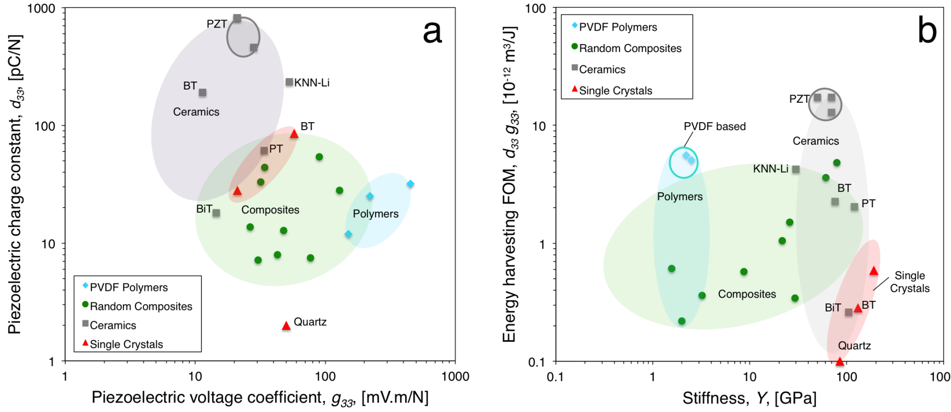

Figure 1.7: Performance of single crystal, ceramic, polymer and random polymer composite piezoelectric materials [3, 9, 24, 32, 52, 54, 55, 57, 60–63]. (a) Piezoelectric charge coefficient, d_{33} versus the voltage coefficient, g_{33}. (b) Energy harvesting figure of merit, dg, versus Young's modulus, Y, in the thickness direction.

1.2. SCOPE AND OUTLINE OF THIS THESIS

IN this thesis, several methods to enhance dielectrophoretically structured piezoelectric composites for sensing and energy harvesting applications are presented. To encourage implementation of these composites, an upscaling scheme is explored and the energy harvesting potential under direct strain is determined. Both random and dielectrophoretically structured composites are investigated, prepared with PZT and KNLN fillers and a range of polymer matrices. The performance is consistently compared to commercial reference materials. Finally, the figure of merit for energy harvesting with piezoelectric materials is analytically derived and experimentally validated.

Chapter 2 describes the materials development and characterization of piezoelectric composites prepared with an array of KNN based ceramic particles doped with Li in an epoxy matrix [64]. The effect of Li substitution on the particle morphology and crystal structure of the two-step calcined KNLN particles is evaluated. The piezoelectric performance of random and dielectrophoretically structured composites based on these KNLN particles is studied through both quasi static and frequency response methods with focus on the impact of Li content.

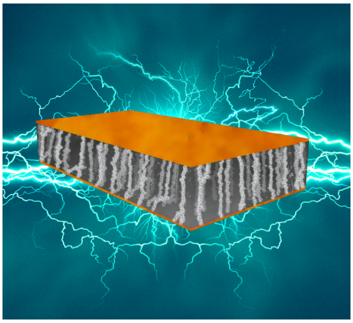

Figure 1.8: Artist's impression of an aligned piezoelectric composite film [7].

Chapter 3 describes the fabrication and quantitative analysis of the first aligned piezoelectric composite film implemented in a touch sensor [65, 66]. Lead-free microcubes, developed in Chapter 2, are dispersed in an uncured polydimethylsiloxane (PDMS) matrix and oriented by application of a dielectrophoretic alignment field. The state-of-the-art piezoelectric constants are measured and quantitatively interpreted. Aligned films are implemented in a flexible touch sensor. The high sensitivity is demonstrated under a controlled dynamical change of applied force, and by finger tapping a load matched and amplified flexible touch patch.

Chapter 4 describes the development of an upscaling scheme, transferable to roll-to-roll production, for dielectrophoretic structuring of piezoelectric composites [67]. The upscaling scheme consists of applying the dielectrophoretic field between a moving doctor blade and a ground electrode on a composite of PZT particles in a photocurable urethane dimethacrylate (UDMA) based matrix. The developed upscaling method leads to horizontal structurization of the piezoelectric particles, necessitating the exploration of several poling methods for horizontally structured composites. The performance of horizontally structured composites is compared to analogously prepared random composites. A sensor patch based on a high volume content piezoelectric composite is fabricated for integration in a technology demonstrator.

Chapter 5 explores whether the improved response of many piezoelectric materials to shear over tensile strain is retained in ceramic-polymer composites [68]. To that end, piezoelectric PZT particles are randomly dispersed in a passive polymer matrix at volume contents from 0 to 40 %, poled, and actuated by tensile and shear loading. To further explore the performance due to shear loading, a finite element model was developed, which was verified through established analytical models and validated by experiments. The shear mode response is compared to that of the same composites loaded in simple tension.

Chapter 6 describes the analysis and experimental validation of the figure of merit for piezoelectric energy harvesters [69]. Clamped piezoelectric disks are actuated with a sinusoidal excitation and the stored electrical energy is measured as a function of internal polarization state, disk geometry and material class. As the internal elastic strain energy in a clamped disk is relatively small, a new piezometer tool was developed to amplify and accurately measure the piezoelectric response to dynamic forces below 10 N. The figure of merit, dg, is confirmed as the appropriate figure of merit for piezoelectric energy harvesters, independent of material class and stiffness.

The main findings of the thesis are reiterated in the **Summary**.

2

ENHANCING THE ENERGY HARVESTING POTENTIAL OF $(K,Na,Li)NbO_3$-EPOXY COMPOSITES VIA LI SUBSTITUTION

> *Science doesn't know everything. If it did, it would stop.*
>
> Dara O'Briain

In this chapter, the influence of Li substitution on the piezoelectric performance of lead free $K_{0.5}Na_{0.5}NbO_3$ *(KNN)-epoxy composites is explored. KNN piezoceramic particles modified with 0 to 12 mol.% of Li are prepared via a double calcination technique, resulting in a perovskite particulate which transitions from an orthorhombic to tetragonal crystal structure between 6 and 9 mol.% of Li, and contains a minor non perovskite second phase from 6 mol.%. A cuboid particle morphology is evident in all cases, though tetragonal KNN-based particles have formed with serrated edges and fractures. The particles are dispersed at 10 vol.% in an epoxy matrix to develop both random and dielectrophoretically structured* $(K,Na,Li)NbO_3$*-epoxy composites. The dielectric constant of the composites appears almost independent of Li content, while the piezoelectric charge coefficient of structured composites peaks before the polymorphic phase transition, at 3 mol.% of Li. The peak in performance can be attributed to the increased primary particle size of the composition in combination with its single phase orthorhombic crystal structure. The enhancement of the energy harvesting figure of merit, derived from substituting 3 mol.% of Li in the KNN particulate, makes these composites an interesting choice for flexible energy generators.*

This chapter has been published in the Journal of the American Ceramic Society **100**, (2017) [64].
The experimental work was carried out by N. T. Mascarenhas as a part of her M.Sc. thesis, under the author's supervision [70].

2.1. INTRODUCTION

RESEARCH into flexible piezoelectric materials is on the rise for their potential for strain driven energy harvesting and integration into and onto flexible and wearable electronics [19, 71]. Most commercial piezoelectrics are based on ceramics which contain lead atoms in their crystal structure, yet for environmental reasons, lead free materials are preferred [18, 22]. Of the lead free ceramics, those based on the morphotropic phase boundary (MPB) composition $[K_{0.5}Na_{0.5}]NbO_3$ (KNN) doped with Li are a promising candidate for energy harvesting due to their high Curie temperature (around 400 °C), enabling use at a wide range of temperatures, and favorable electrical properties [18, 22]. As in many piezoelectric ceramics, compositions near the phase transition at $[K_{0.5}Na_{0.5}]_{(0.94)}Li_{0.06}NbO_3$ (KNLN6) lead to the best piezoelectric properties [20, 22, 23, 72].

The influence of Li substitution on the piezoelectric and dielectric properties of KNN based ceramics has been investigated extensively [20, 22, 23, 72–76]. In monolithic ceramics Li substitution increases the grain size and the Curie temperature, T_C [°C], while simultaneously lowering the orthorhombic to tetragonal transition temperature T_{O-T} [°C] [20, 22, 23, 72]. A wide range of electrical and mechanical properties have been reported for KNN ceramics doped with Li [20, 22, 23, 72–76]. Despite favorable piezoelectric performance, KNN based ceramics are plagued by variations in the volitalization and segregation of the alkali elements inducing compositional inhomogeneity [73] and the formation of a secondary tetragonal tungsten bronze (TTB) phase [74], and abnormal grain growth (AGG) [75]. Minor adjustments to the processing scheme drastically affects the behavior of alkali elements and contributes to the ultimate performance of the sintered ceramic [22, 73]. Due to the cuboid morphology of the grains, KNN based ceramics are also notoriously difficult to sinter into dense ceramics. Faster heating rates [74], inert atmospheres [76], and long isothermal holds [75] have been reported to inhibit the formulation of strongly facetted cuboid grains, aiding densification.

A number of flexible lead free piezoelectric materials based on a composite of KNN based particles randomly dispersed in a polymer matrix have been developed for piezoelectric energy harvesting [49–52, 54–56]. The chosen KNN fillers are identical to the compositions developed for optimal properties in ceramics, doped with sintering aids, at or near a polymorphic phase transition (PPT) or MPB. Additionally, these piezoelectric composites require a relatively high volume content of ceramic filler (from 30 vol.% for nanowires up to 85 vol.% for particles) to attain sufficient performance.

Besides the volume fraction of filler, piezoelectric performance in electroceramic - polymer composites is affected by: (i) the electrical properties of the filler and matrix, (ii) the size and morphology of the filler, and (iii) the spatial distribution of the filler [30, 34, 77, 78]. In KNN based ceramics (i) and (ii) are not independent variables, and altering one (via compositional substitution or processing conditions) will necessarily affect the other [20, 22, 23, 72–76]. The spatial distribution can be controlled by choosing an appropriate composite processing scheme, like dielectrophoretic structurization [37, 38]. Applying a dielectrophoretic alignment field on lead based piezoelectric fillers inside an uncured polymer matrix leads to a significant improvement of the piezoelectric performance in composites containing only 10 vol.% of filler compared to randomly dispersed composites [39]. Switching to lead free KNLN6 further improves the performance of structured composites, due to the inherent electrical properties of the filler and the cuboid nature of the particles [40]. However, it is clear from the literature that MPB compositions do not always lead to the best performance in piezoelectric composites [38, 78–80].

Due to the variance in reported KNN based ceramic properties, it is unclear at which amount of Li substitution in KNN the peak performance in piezoelectric properties of composites can be established. Hence, in the present work we will investigate composites based on near PPT $[K_{0.5}Na_{0.5}]_{(1-x)}Li_xNbO_3$ (KNLN) particles specifically prepared for embedding in an epoxy matrix and study the effect Li content has on particle morphology, piezoelectric performance and energy harvesting potential.

2.2. EXPERIMENTAL PROCEDURE

2.2.1. ELECTROCERAMIC POWDER PREPARATION

FIVE piezoceramic powders were synthesized via solid state reaction with compositions of $[K_{0.5}Na_{0.5}]_{(1-x)}Li_xNbO_3$ (x = 0, x = 0.03, x = 0.06, x = 0.09 and x = 0.12). Stoichiometric proportions of the >99% pure oxides $NaCO_3$, K_2CO_3, Li_2CO_3, and Nb_2O_5 (obtained from Sigma Aldrich) were immersed in cyclohexane and milled in glass jars with 5 mm yttria-stabilized ZrO balls. A two step calcination scheme was employed to obtain cuboid particles [40]. Each KNLN powder was calcined at 1050 °C for 3 hours (heated with a rate of 5 °C/min), milled for 5 hours, and calcined again at 950 °C for 20 hours (heated with a rate of 1 °C/min). To break apart loose aggregates, the calcined powders were ultrasonicated for 1 hour and sieved through a 63 μm mesh. All KNLN powders were dried overnight at 150 °C, and stored under vacuum at room temperature before processing into composites.

2.2.2. COMPOSITE PREPARATION

Composite disks were prepared by mixing the KNLN powders in Epotek epoxy 302-3M (Epoxy Technology Inc., Billerica (MA), USA) with a particle volume of 10 %. This optically clear epoxy has been extensively studied as a matrix for dielectrophoretically structured composites [38–40], and has a relatively high dielectric constant, ε_{33} [−], of 5.3 at room temperature. The theoretical density of each KNLN powder, calculated from the mass of the unit cell over the unit cell volume, was used to calculate the appropriate mixing ratio for each composite. The KNLN particles were mixed with diglycidyl ether of bisphenol-A (DGEBA) resin for 5 min at 2500 rpm in a SpeedMixer (Hauschild, DAC 150 FVZ, Hamm, Germany). Then the multi-functional aliphatic amine hardener poly(oxypropyl)-diamine (POPD) was added to the KNLN-resin mixture and mixed again for 5 min at 2500 rpm. The uncured composite was degassed in a vacuum for 10 min, mixed for 5 min at 2500 rpm to ensure homogeneous distribution of the particles, and poured into a prepared Teflon mold with circular 14 mm diameter cutouts. Al foil sheets of 50 μm thickness were applied on either side of the mold to act as the electrodes for dielectrophoresis (DEP). Flat samples were formed by clamping the mold between two steel plates. To induce dielectrophoretic structuring an electric field of 1 kV mm^{-1} was applied at an optimal frequency, ranging from 600 Hz to 1.2 kHz, using a function generator (Agilent, 33210A, Santa Clara (CA), USA) in tandem with a high voltage amplifier (TREK, Model 609E-6, Lockport (NY), USA) at room temperature. The leakage current, peak to peak voltage and phase angle of the DEP field were monitored with an oscilloscope (Tektronix Inc., DSOX2002A, Berkshire, UK). After 1 hour at room temperature the composites were cured on a hot plate (IKA, C-MAG HS7, Staufen, Germany) at 50 °C in 3 hours, keeping the DEP field applied. Random composites were prepared analogously, without application of an electric field. Next, the composites were ejected from the mold and polished to ensure good contact with electrodes. After post-curing at 120 °C for 1 hour, gold electrodes were applied on either side with a sputter coater (Balzers Union, SCD 040, Liechtenstein). The samples were poled in a rapeseed oil bath (Julabo, SE Class III, 12876, Seelbach, Germany) at 80 °C and 11 kV/mm for 30 min with a DC high voltage amplifier (Heinzinger, PNC 30000, Rosenheim, Germany) and cooled to room temperature while still applying the electric field. The composite samples were aged for at least 24 hours before piezoelectric and dielectric measurements took place.

2.2.3. MEASUREMENT METHODS

X-ray diffraction (XRD) (Bruker D8 Advance X-ray diffractometer, Bruker AXS Inc., Karlsruhe, Germany, using Co-Kα with EVA software) was used to analyze the crystal structure. UnitCell [81] was used to calculate the lattice parameters from the identified peaks. Particle morphology and spatial distribution of the KNLN particles in the random and structured composites were recorded with a field-emission scanning electron microscope (SEM) (JEOL, JSM-7500F, Nieuw Vennep, the Netherlands). Particle size was measured in aqueous solution via laser diffraction (Beckman Coulter LS230, Beckman Coulter Nederland B.V., Woerden, the Netherlands) and from SEM. The piezoelectric charge coefficient, d_{33} [pC/N], of the composites was measured with a PM300 Berlincourt type piezometer (Piezotest, London, United Kingdom). The capacitance, C [pF], and dielectric loss, tan δ [−], were measured at 1 kHz and 1 V with an LCR (Agilent, 4263B, Santa Clara (CA), USA). The ε_{33}^{T} was derived from the capacitance. Thickness mode electromechanical coupling coefficients, k_t [%], and mechanical quality factors, Q_m [−], were determined by the IEEE resonance method using an impedance analyzer (Agilent, HP4194A, Santa Clara (CA), USA).

2.3. RESULTS

2.3.1. STRUCTURAL CHARACTERIZATION

X-RAY diffraction patterns of the double calcined KNLN powders are presented in Fig. 2.1, normalized to the highest intensity peak. A single phase orthorhombic perovskite phase was observed in the undoped KNN and 3 mol.% Li specimens. Increasing the amount of Li beyond 3 mol.% results in the development of a minor secondary phase; indexed as $K_3Li_2Nb_5O_{15}$ (ICDD:52-0157) with a non perovskite tetragonal tungsten bronze (TTB) structure. The development of the TTB phase has been attributed to the volatilization (of K) and segregation (of Na and Li) of the alkali elements during the prolonged post calcination [72, 75, 82]. At 6 mol.% Li, a coexistence of a tetragonal and orthorhombic phase could be expected, but the specimen tends towards an orthorhombic crystal structure presumably due to loss of Li to the TTB phase. The KNN specimens doped with 9 and 12 mol.% of Li display a tetragonal crystal structure. Fig. 2.1b shows a magnification of the 2θ range running from 36° to 39°, where the inversion in peak splitting due to Li can be clearly seen.

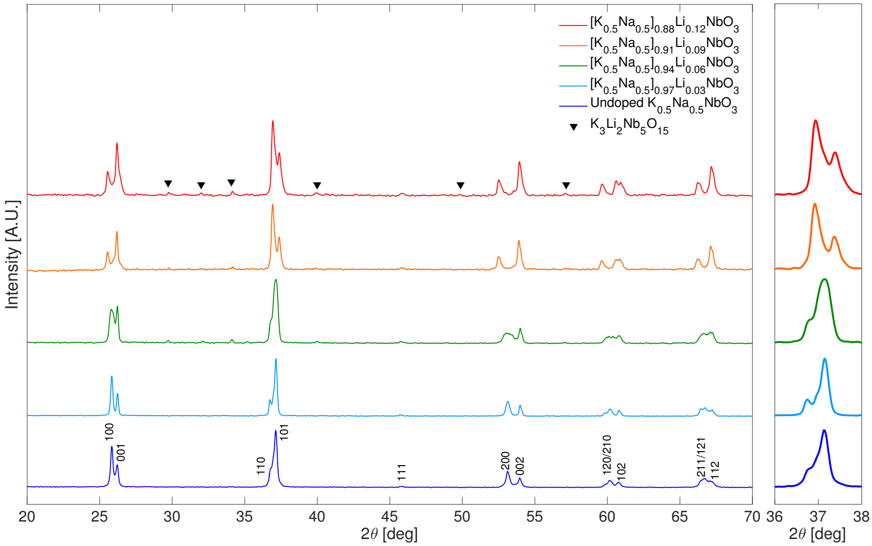

(a)

(b)

Figure 2.1: XRD patterns (a) of $[K_{0.5}Na_{0.5}]_{(1-x)}Li_xNbO_3$ (KNLN) (x = 0, x = 0.03, x = 0.06, x = 0.09 and x = 0.12), and (b) a magnification of the range 36° to 39° 2θ.

2.3.2. PARTICLE MORPHOLOGY

Double calcination of the KNLN particulate with 20 h of annealing at 950 °C, by slowly heating at 1 °C/min, has lead to the formation of cuboid particles (Fig. 2.2). Small cuboid particles on the order of 0.5 to 1.0 μm with strongly facetted edges have developed in the undoped KNN. Doping with Li increases the size of the cuboid particles. At 6 mol.% of Li the particle size decreases slightly, and some columnar shaped particles, likely TTB phase, on the order of 0.5 μm are observed. At 9 and 12 mol.% the cuboid particles develop serrated, roughened edges around facetted surfaces, and many of the particles have fractured. It is difficult to distinguish whether the clusters of cuboid grains have sintered together to form aggregates or are free flowing from SEM alone. Therefore, the particle size was measured in aqueous solution via laser diffraction. However, since the particles tend to agglomerate, the particle dispersion was not representative of the actual particle size distribution.

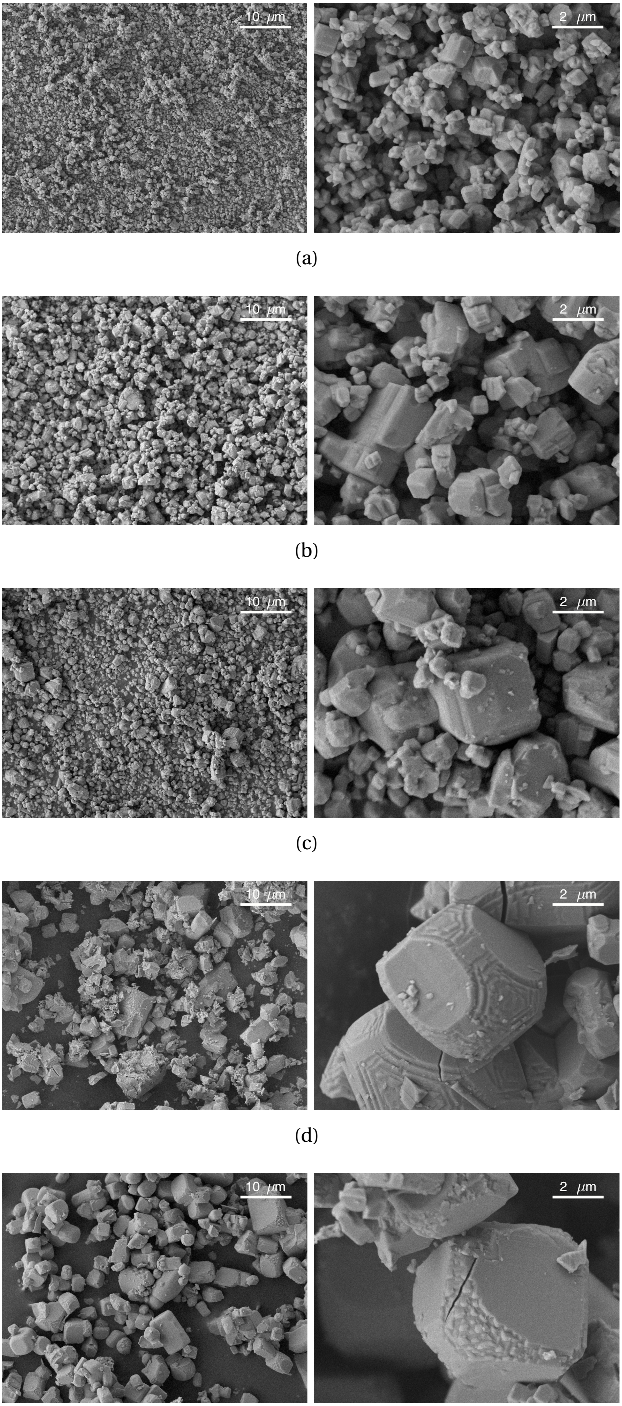

(a)

(b)

(c)

(d)

(e)

Figure 2.2: Micrographs of the two-step calcined KNLN particles (at 2000x (left) and 10000x (right) magnification), with increasing Li content: (a) Undoped KNN, (b) 3 mol.%, (c) 6 mol.%, (d) 9 mol.% and (e) 12 mol.%.

2.3.3. COMPOSITE MICROSTRUCTURE

In Fig. 2.3 and 2.4 the cross-section of the composite microstructures of the KNLN particulates processed into both random and structured composites at 10 vol.% of filler are shown. It is immediately clear that the double calcination of the KNLN particulates has lead to aggregation of particles. Even so, the dispersion of the primary particles and aggregates is relatively homogeneous in both random and structured composites. Comparing the microstructure of random composites to structured, it is clear that the application of the dielectrophoretic structuring field has induced the KNLN particles to align into chains parallel to the direction of the electric field. Chains of primary particles are interspersed with large aggregates. Compositions with a larger relative volume of primary particles (the undoped KNN and 12 mol.% of Li) more clearly show the formation of chain like structures in the direction of the applied electric field, compared to their random counterparts.

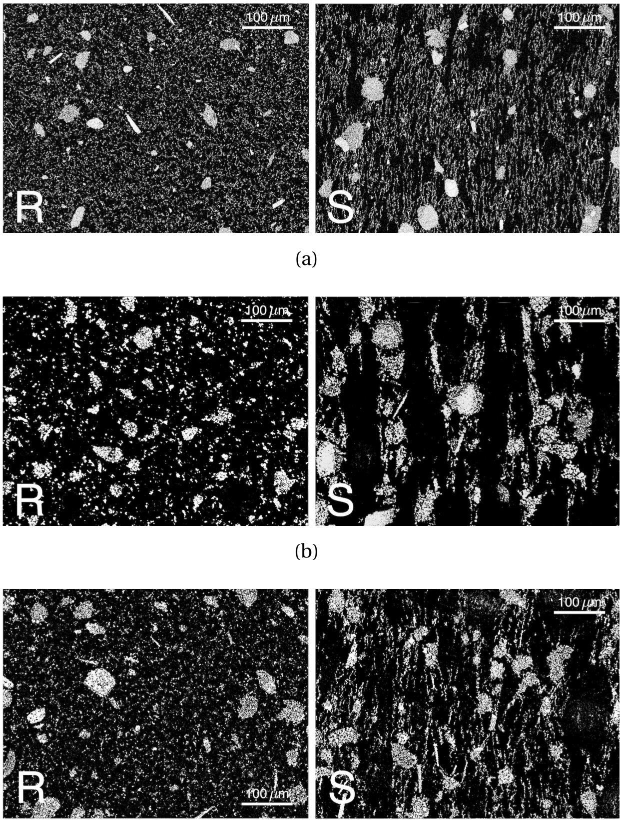

(a)

(b)

(c)

Figure 2.3: Micrographs of the cross-section of 10 vol.% KNLN-epoxy composites (magnification 200x) with increasing Li content (a) Undoped KNN, (b) 3 mol.%, and (c) 6 mol.%. The ‘R’ and ‘S’ stand for random and structured composites, respectively.

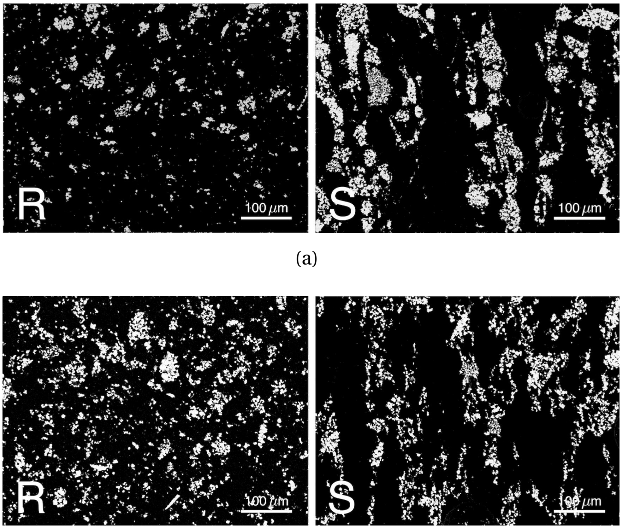

(a)

(b)

Figure 2.4: Micrographs of the cross-section of 10 vol.% KNLN-epoxy composites (magnification 200x) with increasing Li content (a) 9 mol.% and (b) 12 mol.%. The 'R' and 'S' stand for random and structured composites, respectively.

2.3.4. DI- AND PIEZOELECTRIC PROPERTIES

The piezoelectric constants of the KNLN-epoxy composites are presented in Fig. 2.5 as a function of Li content. The dielectric constant (Fig. 2.5a) trends upward with Li in structured composites. Any variation in dielectric properties or morphology of the particles has no effect on the dielectric constant in random composites, which remains at a flat constant around 8.5. The dielectric loss of the composites, presented in Fig. 2.5b, is below 5 %, and the trends are in line with the dielectric constant. Structuring of the KNLN particles has marginally increased the dielectric constant and loss over all Li contents. The dielectric loss remains unchanged after 1 year stored at ambient conditions, indicating that encapsulation of the KNLN particles in the composites appears to inhibit the moisture absorption commonly reported for Li-doped KNN ceramics. The influence of Li content on the piezoelectric charge coefficient, d_{33}, of 10 vol.% KNLN-epoxy composites is presented in Fig. 2.5c. The d_{33} is dependent on the phase structure, and higher on the orthorhombic side. In random composites, this translates to a relative constant of 5 pC/N on the orthorhombic side, and 2 pC/N for the tetragonal compositions. The properties are improved by dielectrophoretic structuring of the KNLN particles, and a peak in piezoelectric charge coefficient can be identified at 3 mol.% of Li with 19.4 pC/N. In application as a sensor or an off-resonance energy harvester, the piezoelectric voltage constant, g_{33} [mV.m/N], and figure of merit, $d_{33} \cdot g_{33}$ $[pm^3/J]$, of the KNLN-epoxy composites are of the utmost importance. These figures are presented as a function of Li content in Fig. 2.5d,e. The g_{33} is calculated via: $g_{33} = d_{33}/(\varepsilon_{33} \cdot \varepsilon_0)$, where ε_0 is the permittivity of free space and the ε_{33} is measured at 110 Hz. The maximum values obtained in random composites are 68 mV.m/N and 0.43 pm^3/J at x = 0, while for structured composites the maximum attained values are 181 mV.m/N and 3.5 pm^3/J, at x = 0.03. The magnitude and position of the maximum g_{33} value in structured composites depends on the stiffness ratio of the piezoelectric phase over the polymer phase, and it is likely that higher values could be obtained at lower particle volume fractions, while increases in $d_{33} \cdot g_{33}$ could be expected at slightly higher volume fractions [39, 40].

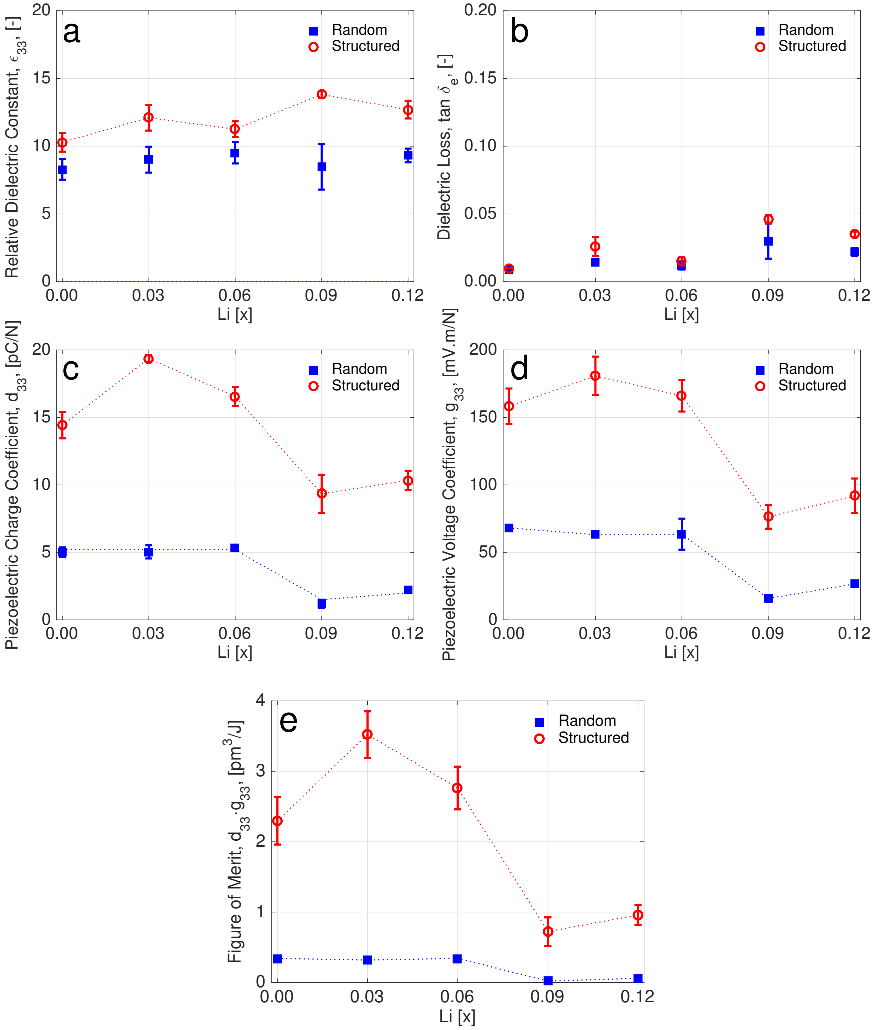

Figure 2.5: Piezoelectric constants of KNLN-epoxy composites. (a) Relative dielectric constant, ε_{33}, as a function of Li content substituted in $[K_{0.5}Na_{0.5}]_{(1-x)}Li_xNbO_3$. (b) Dielectric loss, $tan\ \delta_e$. (c) Piezoelectric charge coefficient, d_{33}. (d) Piezoelectric voltage coefficient, g_{33} and (e) Figure of merit, $d_{33} \cdot g_{33}$. Open circles represent dielectrophoretically structured composites. Solid squares represent randomly dispersed composites, prepared without dielectrophoretic field. The dotted lines are a guide for the eye.

The piezoelectric performance of the structured orthorhombic KNLN composites could also be studied via frequency response analysis, due to the relatively high attained d_{33} (Fig. 2.6). The materials properties are summarized in Table 2.1, where each value is the average of three samples per Li content, with dimensions of 9 mm in diameter and approximately 1 mm thickness.

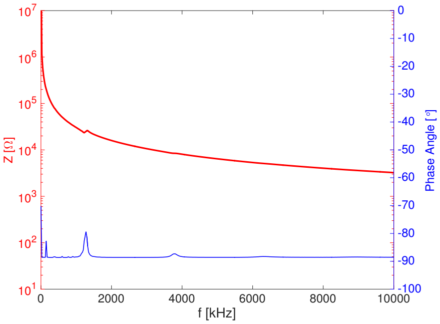

Figure 2.6: Raw frequency response (phase angle and impedance) of a structured KNLN3-epoxy composite.

The mechanical loss factor, Φ, is evaluated from the resonance peak in the frequency dependence of the real part of the impedance, Z', via $\Phi = (f_1 - f_2)/f_{peak}$, where f_1 and f_2 are the frequencies at which the impedance is equal to $Z'_{peak}/\sqrt{2}$. The mechanical quality factors follow from the relation $Q_m = 1/\Phi$. The k_t was evaluated from the following equation, where f_s and f_p are the series and parallel resonance frequencies [1].

$$k_t = \frac{\pi}{2}\frac{f_s}{f_p} tan\left(\frac{\pi}{2}\frac{\Delta f}{f_p}\right) \tag{2.1}$$

For materials with high mechanical losses, the IEEE recommends approximating Δf from the following equations, directly from the minimum, f_m, and maximum resonance frequencies, f_n, via a figure of merit 'M' [1, 83].

$$\Delta f = (f_p - f_s) \approx \frac{f_n - f_m}{\sqrt{(1 + \frac{4}{M^2})}} \tag{2.2}$$

$$M = \frac{1}{2\pi f_s R_1 C_0} \approx \frac{1}{2\pi f_m \left(C_0 + C1\right)|Z_m|} \tag{2.3}$$

The sum of C_0 and C_1 (representing the capacitance of the parallel and series branch of the equivalent circuit of the piezoelectric material near resonance) is equivalent to the static capacitance measured below the fundamental resonance, at 1 kHz. R_1 is the resistance of the series branch of the equivalent circuit and $|Z_m|$ is the impedance minimum at resonance. Finally, the frequency constant, N_t^D [Hz.m], was calculated from $N_t^D = f_p \cdot t$, where t [mm] is the sample thickness, leading to the longitudinal velocity C_t [m/s] equal to $2N_t^D$.

Table 2.1: Electromechanical properties of 10 vol.% structured orthorhombic KNLN-epoxy composites from the thickness mode resonance.

Li [x]	M [-]	k_t [%]	Q_m [-]	N_t^D [Hz.m]	C_t [m/s]
0.00	0.93	13.6	21	1211	2422
0.03	0.97	26.8	15	1376	2751
0.06	0.95	15.0	25	1217	2433

2.4. DISCUSSION

FROM the above results, we can tentatively propose the following processes take place in the studied electroceramic-polymer composites. Substituting Li in MPB cuboid KNN particles increases the particle size, but leads to the formation of a secondary non perovskite phase. The presence of the TTB phase in the KNLN composites with 6 to 12 mol.% of Li lowers the effective amount of polarisable volume, decreasing performance in composites. At 3 mol.% of Li no such TTB phase is discernible from XRD. While the coarsening and necking between the particles at 9 and 12 mol.% of Li is considered to be related to the well studied lower temperature of the liquid phase formation in these compositions [20, 22, 23, 72], the decrease in particle size at 6 mol.% of Li would indicate a change in the particle formation mechanism. The observed fracturing of the high Li content particles may be attributed to the high degree of tetragonality leading to high strains during cooling, and could signal a secondary mechanism of decreased performance in composites. In the particle size range observed from SEM (from 1.0 μm in the undoped KNN to >5 at 9 and 12 mol.% Li) we would expect to see a dependency of the d_{33} of random composites on particle size [77, 78]. The absolute value of the d_{33} is also higher than one would expect at 10 vol.% of filler from existing models for monodisperse particles in a dilute medium [34]. This suggests that the observed aggregates dominate the performance in random composites, regardless of the variance in electrical properties of the filler as a function of Li content. Structuring the KNLN particles in an epoxy matrix has enhanced the d_{33} and ε_{33}^T with respect to random composites, and previous work at the PPT [40], showing that dielectrophoretic structurization is a robust method of improving piezoelectric performance in composites. Fig. 2.5a suggests that the dielectric constant increases with Li content, except at 6 mol.% where the particle size decreases slightly. Since larger particles lead to fewer polymer interfaces per aligned chain [37], we suggest the increase in dielectric constant is a particle size effect. Similar to random composites, the d_{33} of the structured orthorhombic composites outperforms tetragonal compositions. Yet there is a peak at 3 mol.% of Li, not evident from the results of random composites. In structured electroceramic-polymer composites, the morphology and size of the particles will affect the efficiency of chain formation due to dielectrophoresis and degree of poling [38, 39, 84]. Futhermore, it has been demonstrated that particle size distribution is a key factor in the chain formation of structured composites [85]. The significant decrease in polymer interfaces in structured composites allows the inherent electrical properties of the filler to somewhat overcome the agglomerate dominated behavior observed in random composites. Even though the piezoelectric charge coefficient of the particles at 6 mol.% Li outperforms 3 mol.% Li, the reduction in polymer interfaces due to the larger particle size results in a better performance at 3 mol.% in composites. Furthermore, since the aim of the work is to enhance energy harvesting potential, the reduction in the dielectric constant, in the 3 mol.% Li composites after poling can compensate for the inherently lower d_{33} of the composition [23]. The peak in performance observed at 3 mol.% of Li can then be attributed to the increase in primary particle size, supplemented by aggregates which enhance overall performance via reduced inter-particle distance. To examine the energy harvesting potential of the KNLN based composites, a comparison of the piezoelectric performance of the composites from this study is drawn with piezoelectric materials from the literature in Table 2.2. The piezoelectric composites are ranked according to the volume fraction of active material. To attain a d_{33}, k_t, and figure of merit similar to what we have demonstrated for 10 vol.% structured KNLN3-epoxy in random composites, a combination of high volume fractions of active material, large particle sizes and high dielectric constant polymer matrices are necessary [32, 63, 77, 86]. In lead free composites based on KNN, similar properties have only been reported for 1-3 composites, or volume contents of active material over 0.7 [54–56]. While the figure of merit of the KNLN3 composite approaches that of the KNN bulk ceramic, an order of magnitude lower than PZT ceramics, the performance approaches that of pure PVDF and its copolymers.

Table 2.2: Performance of reported piezoelectric materials compared to this work.

Active material	Active volume [%]	Matrix	d_{33} [pC/N]	k$_t$ [-]	tan δ_e [%]	$d_{33}\cdot g_{33}$ [pm^3/J]	Ref.
Structured KNLN3	10	Epoxy	19	0.27	2.3	3.52	This work
KNN	10	Epoxy	5		0.9	0.34	This work
Structured PZT5A	10	Epoxy	7			0.52	[39]
Structured KNLN	10	Epoxy	13			1.53	[40]
PTCa	50	PEKK	28	0.17	1.2	3.60	[32]
PZT	57	Epoxy	[1]140			[1]6.15	[86]
PTCa	65	PVDF-TrFE	54	0.24		4.83	[63]
PT-BFMn	65	Epoxy	65		3.2	14.9	[77]
KNNLST	70	PVDF	33		7.0	1.05	[54]
KNNLT	85	Epoxy	44			1.51	[55]
1-3 NKNLT	25	Epoxy	140		4.8	7.33	[56]
PVDF	100	-	16	0.11	24	5.11	[87]
PVDF-TrFE	100	-	15	0.26	11	5.60	[87]
KNN	100	-	127	[2]0.41	3.6	4.25	[23]
KNNLT	100	-	230		1.6	4.76	[23]
PZT5A4	100	-	460	≈0.55	1.7	12.9	[60]
PZT507	100	-	820	≈0.40	1.6	17.3	[60]

[1] Average particle size is larger than sample thickness.

[2] k$_t$ from [20].

2.5. CONCLUSIONS

THIS work demonstrates that a significant improvement of the piezoelectric properties of electroceramic polymer composites can be achieved by dielectrophoretic alignment of KNLN particles with a wide distribution in particle size over lead containing composites. A peak in performance of structured composites was identified in KNN doped with 3 mol.% of Li, a single phase orthorhombic composition with cuboid particle morphology. There are indications that it is the combination of favorable electrical properties and particle morphology at $[K_{0.5}Na_{0.5}]_{(0.97)}Li_{0.03}NbO_3$ leading to the peak in piezoelectric performance. While the dielectric constant of the composites is only marginally affected by variations in Li content, the piezoelectric charge coefficient is markedly higher on the orthorhombic side of the phase diagram. Tetragonal compositions, which contain both fractured particles and a minor non perovskite second phase, result in a diminished piezoelectric charge coefficient of the composite, consistent with the trends of monolithic ceramics. Compared to the other orthorhombic compositions, at 0 and 6 mol.% of Li, larger particle sizes have been attained at 3 mol.%, lowering the amount of polymer interfaces per chain. Although a lower homogeneity of the composite microstructure is attained, the performance at 10 vol.% is now such that the electromechancial coupling can be measured via frequency response analysis. Due to the enhanced piezoelectric energy harvesting figure of merit, $d_{33} \cdot g_{33}$, composites based on these materials are an interesting choice for flexible energy generators.

3

FLEXIBLE PIEZOELECTRIC TOUCH SENSOR BY ALIGNMENT OF LEAD-FREE ALKALINE NIOBATE MICROCUBES IN PDMS

Ars longa, vita brevis.

Hippocrates

A highly sensitive, lead-free and flexible piezoelectric touch sensor is reported based on composite films of alkaline niobate $K_{0.485}Na_{0.485}Li_{0.03}NbO_3$ *(KNLN) powders aligned in a polydimethylsiloxane (PDMS) matrix. KNLN powder was fabricated by solid-state sintering and consists of microcubes. The particles were dispersed in uncured PDMS and oriented by application of an oscillating dielectrophoretic alignment field. The dielectric constant of the composite film is almost independent of the microstructure, while upon alignment the piezoelectric charge coefficient increases more than ten fold up to 17 pC/N. A quantitative analysis shows that the origin is a reduction of the inter-particle distance to under 1.0 μm in the aligned bi-continuous KNLN chains. The temperature stable piezoelectric voltage coefficient exhibits a maximum value of 220 mV.m/N, at a volume fraction of only 10 %. This state-of-the-art value outperforms bulk piezoelectric ceramics, is orders of magnitude higher than that of randomly dispersed composites, and is comparable to the values reported for the piezoelectric polymers PVDF and P(VDF-TrFE). Optimized composite films are incorporated in flexible piezoelectric touch sensors. The high sensitivity is analyzed and discussed. As the fabrication technology is straightforward and easy to implement, applications are foreseen in flexible electronics such wireless sensor networks and biodiagnostics.*

This chapter has been published in Advanced Functional Materials **27**, (2017) [65]. The composite fabrication was carried out by N. T. Mascarenhas as a part of her M.Sc. thesis, under the author's supervision [70].

3.1. INTRODUCTION

PIEZOELECTRIC materials have the remarkable ability to convert tensile and compressive stresses into electric charge, and vice versa. Applications that make use of the direct effect, where mechanical stress yields an electric voltage, or of the converse piezoelectric effect, where an electric voltage is generated upon mechanical deformation, are widespread and range from loud speakers, through actuators, to energy harvesters [71, 88–90]. Here we use piezoelectric materials to realize a sensitive, flexible touch sensor, where a voltage is generated upon a dynamical change in applied force.

When a piezoelectric capacitor is poled perpendicular to the electrodes, and actuated and charge tapped in the same direction, a short circuit current, I_{SC}, is generated:

$$I_{SC} = \frac{Q}{\Delta t} = d_{33}\frac{\Delta F}{\Delta t} \tag{3.1}$$

where Q is the generated charge, $\Delta F/\Delta t$ is the change in applied force over time, and d_{33} is the piezoelectric charge coefficient, given in pC/N. The open circuit voltage, V_{OC}, is then derived as:

$$V_{OC} = \frac{Q}{C} = \frac{d_{33}\Delta F}{\varepsilon_0\varepsilon_r A/l} = \frac{d_{33}}{\varepsilon_0\varepsilon_r} l \frac{\Delta F}{A} = g_{33} l \Delta P \tag{3.2}$$

where C is the capacitance, A the area and l the thickness of the capacitor. ε_0 is the permittivity of free space and ε_r is the dielectric constant of the piezoelectric material. Eq. 3.2 shows that the open circuit voltage linearly depends on the change in applied pressure, ΔP, and the thickness of the piezoelectric material. The proportionality constant is the figure of merit of the sensor, *viz.* the voltage coefficient, g_{33}, defined as $d_{33}/\varepsilon_0\varepsilon_r$ and calculated in mV.m/N.

Most piezoelectric materials consist of inorganic ceramics. They exhibit large piezoelectric charge coefficients, over 500 pC/N, but the high value of the dielectric constant severely limits their piezoelectric voltage coefficient [18, 19]. Furthermore, ceramics are inherently brittle and, therefore, cannot be applied in a flexible touch sensor. To that end a piezoelectric polymer is required [91, 92]. We note that high values of the voltage coefficient have been reported for ferroelectret polymers, i.e. soft electroactive films [45–47], but applications are hampered by discharging at elevated temperature [48]. The most widely studied [26, 27], commercially available [24], polymer is the piezoelectric homopolymer polyvinylidenefluoride (PVDF) and its random copolymer with trifluoroethylene (P(VDF-TrFE)). The state-of-the-art piezoelectric voltage coefficient is about 200 mV.m/N. The coercive field, however, is 60 MV/m [27]. Poling films with a thickness of more than 100 μm, needed to generate a measurable voltage output, *c.f.* Eq. 3.2, then requires high poling voltages of more than 6 kV. Another drawback is the low Curie temperature, which for the commonly used copolymer P(VDF-TrFE) (65/35) is only 100 °C.

Hence, there is a need in flexible electronics for a touch sensor that combines the mechanical flexibility of a polymer with a high piezoelectric voltage coefficient and a low coercive field. Here we show that a solution for this material selection problem can be provided by aligned ceramic-polymer composites. Random composites are hardly piezoelectric as an applied electric field is confined by the low dielectric constant of the polymer matrix [30–34]. However, upon aligning ceramic particles in a polymer matrix, the piezoelectric charge coefficient dramatically increases. As the dielectric constant of the composite film remains small, dominated by that of the matrix, the system can exhibit a large g_{33} value.

Dielectrophoresis has proven to be a well suited technique to align a piezoelectric ceramic filler as the active phase, into a low dielectric polymer matrix as passive phase [37–39]. Aligned composite films have been reported with piezoelectric voltage coefficients attaining 120 mV.m/N [40, 64]. The Curie temperature remains, in first order approximation, that of the ceramic filler. The main drawback is that the voltage coefficient lags behind that of PVDF and of P(VDF-TrFE).

To improve the piezoelectric voltage coefficient, we use composites consisting of a piezoelectric ceramic filler inside a low stiffness matrix of polydimethylsiloxane (PDMS). As filler we use lead-free alkaline niobate microcubes, $K_{0.485}Na_{0.485}Li_{0.03}NbO_3$ (KNLN) [20–23], rendering the touch sensor biocompatible. A state-of-the-art high piezoelectric voltage coefficient of 220 mV.m/N is realized by aligning the piezoelectric particles using dielectrophoresis. The implementation in a sensitive touch sensor is demonstrated and the performance is analyzed and discussed.

3.2. EXPERIMENTAL PROCEDURE

PARTICULATE powders with a composition of $K_{0.485}Na_{0.485}Li_{0.03}NbO_3$ (KNLN) were prepared as described previously [40, 64] from stoichiometric mixtures of the >99 % pure oxides $NaCO_3$, K_2CO_3, Li_2CO_3, and Nb_2O_5 (Sigma Aldrich), by milling with 5 mm yttria-stabilized ZrO_2 balls in cyclohexane. A two-step calcination scheme was employed by first calcining at 1050 °C for 3 hours, milling for 5 hours, and then calcining again at 950 °C for 20 hours. The powder was dried, sieved through a 63 μm size mesh and ultrasonicated to mitigate agglomeration. The powder consists of microcubes with a medium diameter of the particle size distribution, $d50$, of 2.4 μm.

The piezoelectric charge coefficient, d_{33}, was measured with a Berlincourt type piezometer on poled capacitors (PM300, Piezotest, London, UK). A static force of 10 N was used, under a 0.25 N peak to peak sinusoidal force at 110 Hz. The capacitance, C, and dielectric loss were measured at 1 kHz and 1 V with an Agilent 4263B LCR meter (Santa Clara, CA, USA). ε_{33}, measured under zero stress, was derived from the capacitance. A tensile tester (Instron 3365, Darmstadt, Germany) was used to measure the Young's modulus and strain at break by uniaxial tensile testing at least 5 different samples at 23 °C.

The open circuit voltage, V_{OC}, was measured with a 6514 Keithley electrometer (Cleveland, OH, USA) by actuating disk-shaped sensors (8.7 mm diameter and 1.1 mm thickness) with a pin force supplied by an inductive voice coil. The dynamic pin force was controlled by an Agilent 33210A function generator (Santa Clara, CA, USA) driving the current amplifier for the voice coil, and ranged from 1 to 10 N at 0.1 to 10 Hz. The sensors were clamped at a static force of 10 N between two rounded electrodes, identical to those used in the PM300 Berlincourt piezometer. The temperature was regulated by a MCPE1-07106NC-S Peltier element placed beneath the bottom electrode.

3.3. FABRICATION OF KNLN-PDMS COMPOSITE FILMS

KNLN-PDMS composite films [49–53] were prepared by mixing the KNLN microcubes in an optically clear two-component polydimethylsiloxane (PDMS) polymer, (Sylgard 184, Dow Corning), at a volume of 0 to 20 %, in a planetary speed mixer (DAC 150 FVZ, Hauschild, Germany). The slurry was degassed, poured into a prepared Teflon mold and clamped between two steel plates.

The KNLN microcubes were aligned in the uncured PDMS by dielectrophoresis, as depicted schematically in Fig. 3.1a. An AC electric field of 2 kV/mm was used. The alignment efficiency of dielectrophoresis can be inferred from the phase angle between applied voltage and leakage current at the dielectrophoresis frequency. The frequency was varied from 1 mHz to 10 kHz. The optimal frequency is obtained when the phase angle in the uncured composite slurry is 90 °. The system then is almost purely capacitive, with minimal leakage current. However, typical phase angles for these systems are as low as 50 - 60 ° depending on the electrical properties of matrix and filler, matrix viscosity, and filler morphology, showing incomplete alignment. Here at 200 Hz we have found an optimal phase angle of 88 ° which implies almost perfect alignment. We did not examine MHz range alignment, since the attained phase angle was already near perfectly out of phase.

As can be seen in Video A1 in the online Supporting Information [64], in the first 10 s, the KNLN microcubes reorient themselves parallel to the electric field lines. Subsequently, the cubes slowly link up into parallel chains. Effective alignment takes place in 60 s and no further particle movement can be distinguished. After alignment, the composites were cured at 100 °C for 1 hour. The dielectrophoretic field remained turned on to prevent particle sedimentation. The particle alignment in the composite film can be inferred from the SEM micrograph of Fig. 3.1b. The micron sized KNLN cubes are not randomly dispersed, but almost perfectly oriented in bi-continuous parallel chains, between the electrodes.

After curing, Au electrodes were applied on both sides of the films with a sputter coater (Quorum Q300T, East Sussex, UK). A photograph of the composite film is presented in Fig. 3.1c. As prepared films are not piezoelectric as the ferroelectric polarization is not aligned. To render the films piezoelectric they were therefore poled in a silicone oil bath at 150 °C, for 6 min at 7.5 kV/mm (for the poling study, see Section 3.B). We note that this field is an order of magnitude lower than the coercive field of PVDF. Afterwards the films were cooled to ambient temperature in the presence of the poling field, and aged for at least 24 hours before (piezo)electric measurement.

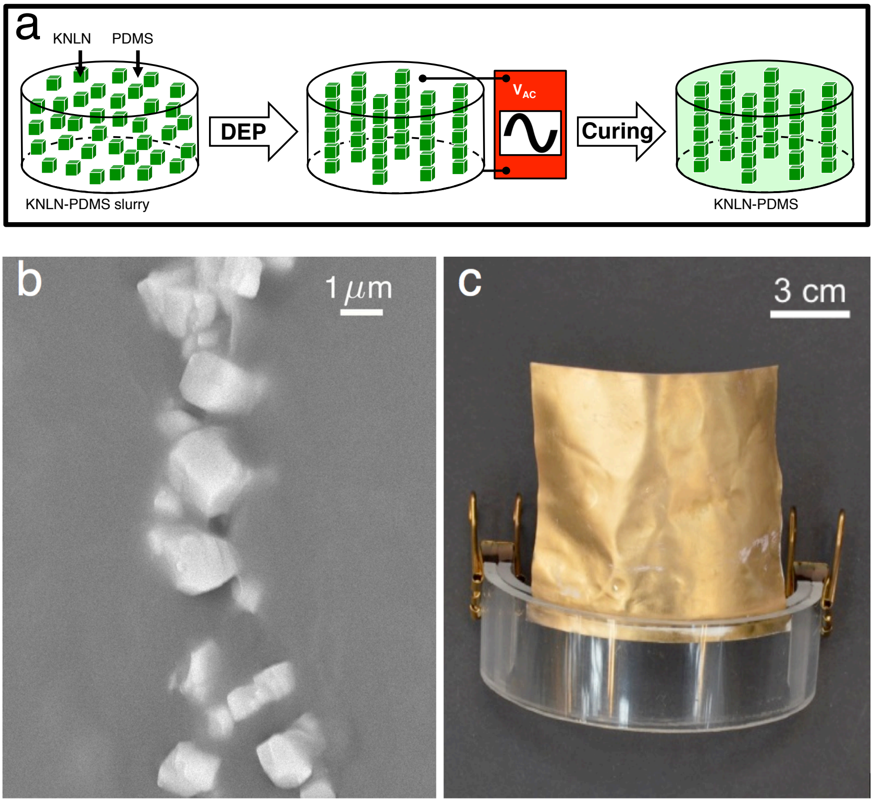

Figure 3.1: (a) Schematic of the fabrication of aligned KNLN-PDMS composite films using dielectrophoresis. (b) Scanning electron micrograph of a cross section of a cured and aligned KNLN-PDMS 5 vol.% composite, showing a single chain of aligned KNLN microcubes in the PDMS matrix. (c) Large area 10 vol.% KNLN-PDMS composite film with Au electrodes sputtered on both sides, clamped between two sheets of curved plexiglass.

3.4. PIEZOELECTRIC CONSTANTS OF COMPOSITE FILMS

FIGURE 3.2a represents the measured piezoelectric charge coefficient, d_{33}, as a function of KNLN content. Open circles represent the values extracted for randomly dispersed films, prepared without dielectrophoretic field. The films are hardly piezoelectric. However, the charge coefficient dramatically increases upon aligning the microcubes, as shown by the closed squares. The relative dielectric constant, ε_r, and the corresponding dielectric loss as a function of KNLN content are presented in Fig. 3.2c,d respectively. The dielectric constant monotonically increases with KNLN content and is almost independent of the microstructure. Furthermore, the composite films remain highly resistive as can be inferred from the low value of the dielectric loss, which remains below 2 % for all compositions. From the measured values of the piezoelectric charge coefficient and the dielectric constant we calculated the piezoelectric voltage coefficient, g_{33}. The values are presented as a function of KNLN content in Fig. 3.2b. The voltage coefficient peaks at a state-of-the-art value of 220 mV.m/N at a KNLN content of only 10 vol.% in aligned composites. This value is more than one order of magnitude higher than that obtained for composites with randomly dispersed particles [30–34, 37–40, 49–53, 64] and on par with the values reported for the piezoelectric polymers PVDF and P(VDF-TrFE) [24, 26, 27].

The explanation is that d_{33} strongly depends on the intra-chain connectivity, while ε_r is a bulk property, proportional to the fill factor but almost independent of the microstructure. In random composites with low volume fractions of ceramic particles, the electric field is confined in the low dielectric constant polymer matrix. There is no electric field over the piezoelectric particles, which explains why the d_{33} in random composites is very small.

There are many models to describe the dependence of ε_r and d_{33} on the volume fraction of two phase random ceramic-polymer composites [93]. Here we use the Yamada model, given by Eq. 3.3 and 3.4 as [34]:

$$\varepsilon_{r_{Yamada}} = \varepsilon_p \left[1 + \frac{n\varphi\left(\varepsilon_{33_c} - \varepsilon_p\right)}{n\varepsilon_p + \left(1-\varphi\right)\left(\varepsilon_{33_c} - \varepsilon_p\right)} \right] \tag{3.3}$$

$$d_{33_{Yamada}} = \frac{\alpha\varphi n\varepsilon_p}{n\varepsilon_p + \left(\varepsilon_{33_c} - \varepsilon_p\right)} d_{33_c} \tag{3.4}$$

where φ is the volume fraction of the ceramic particles and n is their aspect ratio, or shape factor. The sub-indices 'p' and 'c' stand for polymer and bulk ceramic respectively. The composite films are fully poled; hence the poling efficiency, α, is taken as unity. For the bulk values we use: a d_{33_c} of 125 pC/N, ε_{33_c} of 400 and ε_p of 3.9 [20–23].

The dotted lines in Fig. 3.2a,c represent simultaneous fits of d_{33} and ε_r to the experimental data. A good agreement is obtained. Both d_{33} and ε_r increase with volume fraction. For the shape factor a value of 5.6 is extracted. This value implies a rectangular aspect ratio of the particles of 1.95, in fair agreement with the aspect ratio obtained from the SEM micrograph of the microcubes ($c.f.$ Fig. 3.1b).

In aligned composites the value of d_{33} remains small until at a high enough fill factor the first bi-continuous paths between the electrodes are formed. After this threshold, the value of d_{33} increases with the volume fraction of percolating paths. This behavior can quantitatively be described with the Bowen model for ε_r and the Van den Ende model for d_{33}, given by Eq. 3.5 and 3.6 as [37, 39]:

$$\varepsilon_{r_{DEP}} = \varphi \left[\frac{R\varepsilon_p\varepsilon_{33_c}}{\varepsilon_{33_c} + R\varepsilon_p} \right] + \left(1-\varphi\right)\varepsilon_p \tag{3.5}$$

$$d_{33_{DEP}} = \frac{(1+R)^2\,\varepsilon_p\varphi Y_{33_c} d_{33_c}}{\left(\varepsilon_{33_c} + R\varepsilon_p\right)\left((1+R\varphi)Y_{33_c} + (1-\varphi)RY_p\right)} \tag{3.6}$$

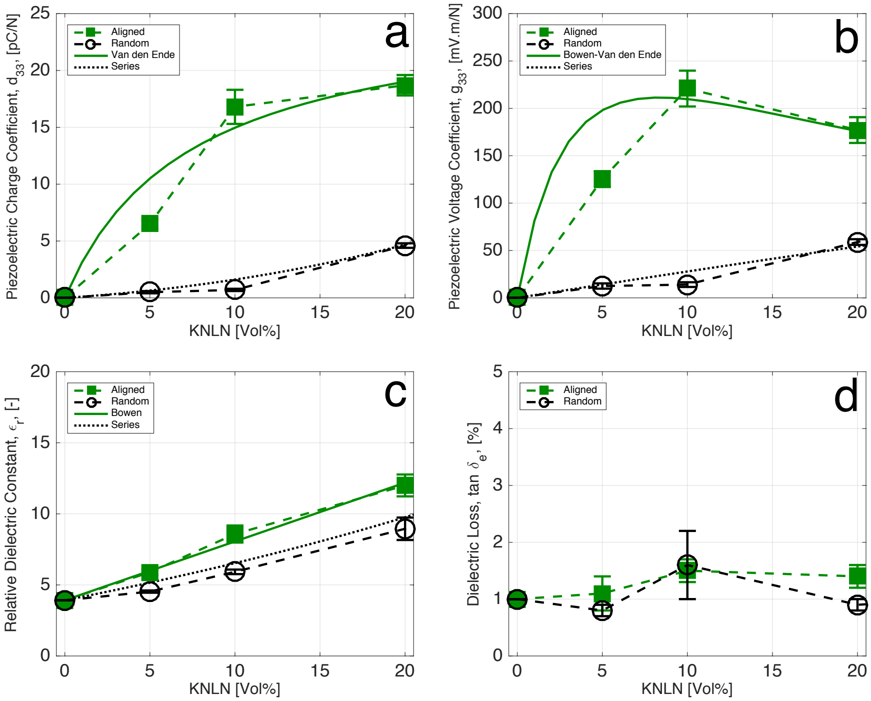

Figure 3.2: Piezoelectric constants of KNLN-PDMS composite films. (a) Piezoelectric charge coefficient, d_{33}, as a function of KNLN content. (b) Piezoelectric voltage coefficient, g_{33}, as a function of KNLN content. (c) Relative dielectric constant, ε_r, as a function of KNLN content and (d) Dielectric loss. Open circles represent randomly dispersed composite films, prepared without dielectrophoretic field. Solid squares represent dielectrophoretically aligned films. Dashed lines are a guide to the eye. Solid and dotted lines are quantitative fits to the data. The error bar at the optimal composition of 10 vol.% is extracted from averaging over more than 10 films.

where R is the intra-chain connectivity, which is equal to the ratio of the mean particle size ($d50$) over the mean inter-particle distance within the bi-continuous chains. The fully drawn lines in Fig. 3.2a,c represent simultaneous fits of d_{33} and ε_r to the experimental data. A good agreement is obtained for an intra-chain connectivity of 13. This value translates to a mean inter-particle distance in the aligned, percolating chains under 1.0 μm in fair agreement with the inter-particle distance observed in SEM micrographs (see Fig. 3.1b). The dielectrophoretic alignment has a staggering effect on d_{33}. At 10 vol.% of filler, the value increases ten fold from 1.5 to 17 pC/N, which is due to the local increase in intra-chain connectivity leading to bi-continuous percolating paths.

In contrast to d_{33}, the dielectric constant, ε_r, experiences only a marginal increase due to alignment of the particles. The dielectric constant is dominated by that of the polymer matrix, does not depend on details of the microstructure, and increases linearly with the volume fraction of ceramic particles (see Fig. 3.2c). Consequently, as shown in Fig. 3.2b, the piezoelectric voltage coefficient, g_{33}, exhibits a maximum at low volume fraction.

3.5. FLEXIBLE TOUCH SENSOR PERFORMANCE

FOR the aligned films with 10 vol.% KNLN that exhibit the optimal, state-of-the-art piezoelectric voltage coefficient, we examined the voltage output as a function of excitation form, pulsed or sinusoidal, applied force, frequency and temperature. We used a film with a thickness of 1.1 mm. The top two panels in Fig. 3.3a show the force and the output voltage under sinusoidal excitation with peak to peak force of 1, 3 and 10 N. The bottom two panels show the force and voltage output under pulse excitation with 1, 3 and 10 N. Inserts show the form of a single sinusoidal excitation and pulse excitation and the corresponding changes in open circuit voltage at 1 N peak to peak. In both cases the output voltage increases linearly with applied force. Under sinusoidal excitation the open circuit voltage follows the change in applied pressure, according to Eq. 3.2. Experimentally there is no overshoot, meaning that inelastic deformation can be disregarded. The extracted piezoelectric voltage coefficient, g_{33}, therefore perfectly agrees with the value of 220 mV.m/N as presented in Fig. 3.2b. In the pulse excitation an overshoot is detected, indicative of inelastic losses, and therefore the extracted value is slightly lower.

The voltage output is almost frequency independent. Fig. 3.3b shows that the output voltage under a 5 N peak to peak sinusoidal force excitation, decreases from an average of 16.9 V peak to peak at 0.1 Hz to 16.0 V at 10 Hz. The frequency independence implies that the leakage current can be ignored, which is in perfect agreement with the low extracted value of the dielectric loss, as shown in Fig. 3.2d.

Compared to commercially available PVDF based polymer and PZT ceramic components the open circuit voltage output is significantly larger (Fig. A1). Furthermore, the voltage output is almost temperature independent. Fig. 3.3c shows the open circuit voltage at temperatures from -10 to 50 °C; under a peak to peak excitation of 5 N the voltage remains at a steady level of about 16 V. This is expected as the voltage coefficient of KNLN is temperature independent far below the Curie temperature, which is about 420 °C [20–23], the measurements are performed far above the glass transition temperature of PDMS of -120 °C and well below the onset of decomposition at 200 °C.

Furthermore the composite films are mechanically flexible. All the films exhibit elastomer type behavior, with a Young's modulus of only 8.6 MPa, and a strain at break of 210 %. These values are similar to that of the elastomeric homopolymer PDMS, which is not surprising as the loading level is only 10 vol.%.

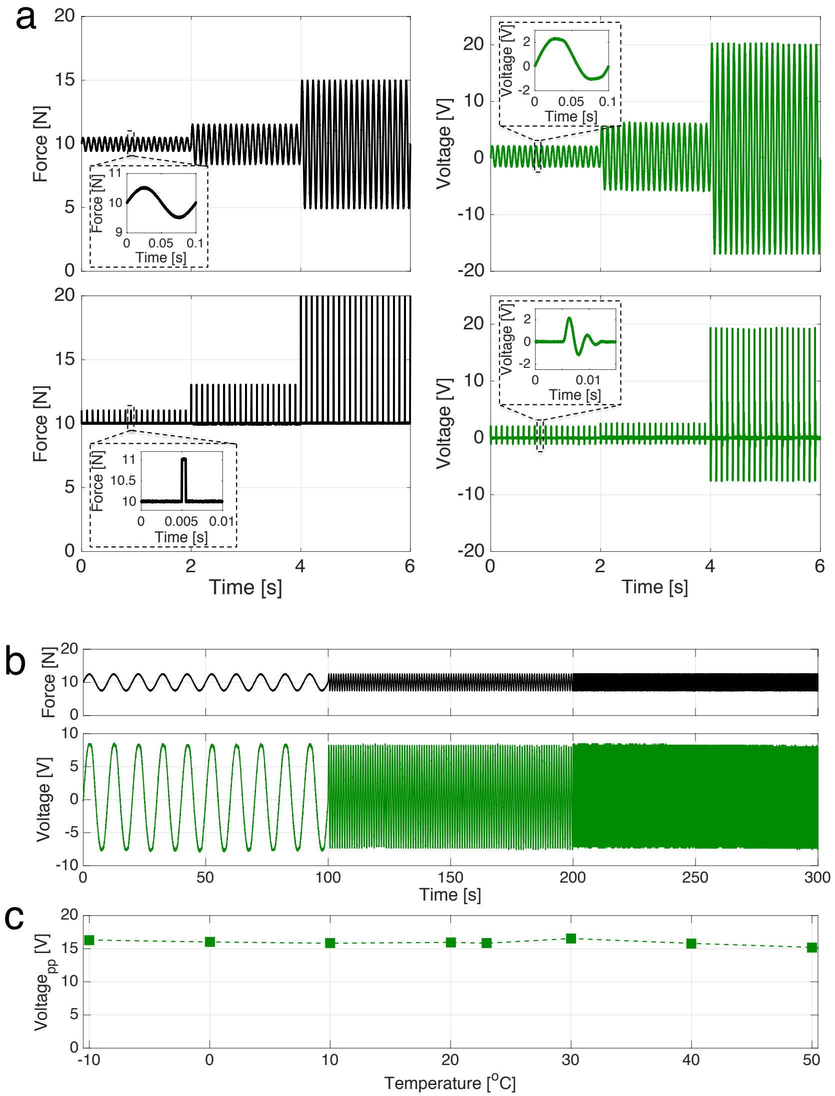

Figure 3.3: Voltage response of 1.1 mm thick, 8.7 mm diameter, composite disks of 10 vol.% dielectrophoretically aligned KNLN microcubes in a PDMS matrix, clamped with 10 N static force. (a) Open circuit output voltage due to applied sinusoidal and pulse force of 1, 3 and 10 N. Inserts show the form of a single sinusoidal excitation and pulse excitation and the corresponding changes in open circuit voltage at 1 N peak to peak. (b) Open circuit output voltage as a function of excitation frequency between 0.1 and 10 Hz. The applied force was 5 N. (c) Open circuit output voltage as a function of temperature. The disk was excited with a sinusoidal force of 5 N. To exclude pyro-electric contributions, the disks were kept at each temperature for 30 minutes before measuring at 1 Hz in 100 s intervals.

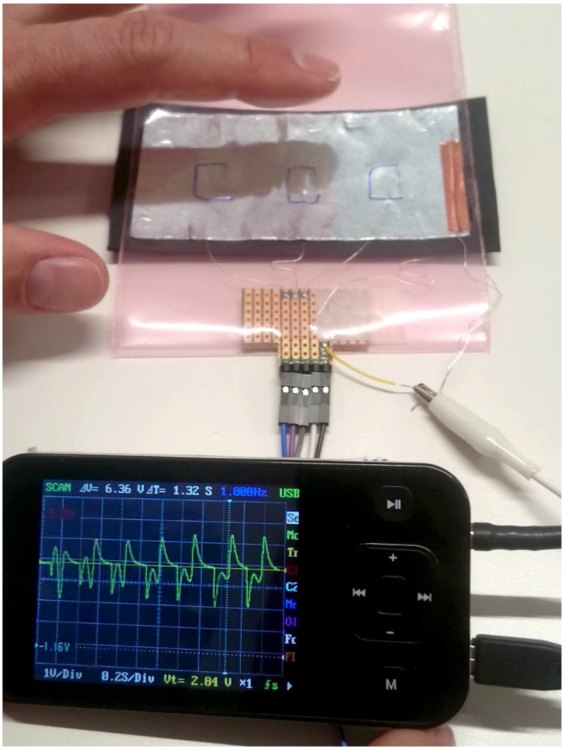

Figure 3.4: Flexible, state-of-the-art piezoelectric touch sensor based on a composite film of 10 vol.% dielectrophoretic aligned KNLN microcubes in a PDMS matrix. The handheld oscilloscope demonstrates the output voltage upon repeatedly touching the sensor. Even light tapping of the sensor generates enough voltage to accurately distinguish variations in touch intensity and speed.

As the overall performance of the composite films is stable with time, frequency and temperature, and as the films are mechanically flexible, they could be integrated into a flexible, touch-sensitive patch, as shown in Fig. 3.4. The flexible sensor patch contains three distinct 10 vol.% aligned KNLN-PDMS sensor buttons, which can be individually tapped. Each piezo button is terminated with a 10 MΩ load and this output voltage is amplified with 208x gain, as shown on the handheld oscilloscope. To suppress unwanted, out-of-band electrical noise the signal bandwidth is reduced by integration in the piezo's own capacitance and further limited with the bandwidth of the amplifier circuit. To improve the signal integrity, all connections are electronically shielded on both sides by Al tape stuck to a thin sheet of (pink) polyethylene. Fig. 3.4 shows that upon touching the sensor, a clear output signal is produced on the oscilloscope. Even light tapping of the piezo button generates enough voltage to accurately distinguish variations in touch intensity and speed (see Video A2 in the online Supporting Information [64]). We note that adding a dielectrophoretic processing step to arrive at a ceramic-polymer composite film is straightforward. Effectively a dense, flexible and large-area composite film can be produced in any shape that can be implemented into a flexible touch sensor.

3.6. CONCLUSIONS

IN SUMMARY, piezoelectric, flexible films were fabricated by dispersing lead-free piezoceramic $K_{0.485}Na_{0.485}Li_{0.03}NbO_3$ (KNLN) microcube powder into an elastomeric PDMS matrix. Before curing the films, the particles were aligned using an oscillating dielectrophoretic field. The dielectric constant of the composite films, ε_r, is almost independent of the microstructure, dominated by that of the PDMS matrix and increases linearly with filler fraction. On the other hand, upon aligning, the piezoelectric charge coefficient, d_{33}, increases more than ten fold, up to 17 pC/N. Quantitative analysis has shown that the origin is a reduction of the inter-particle distance under 1.0 μm in the aligned bi-continuous chains. The piezoelectric voltage coefficient, g_{33}, exhibits a maximum value of 220 mV.m/N, at a volume fraction of only 10 %. This value is more than one order of magnitude higher than that obtained for randomly dispersed particle composites and comparable to values reported for the piezoelectric polymers PVDF and P(VDF-TrFE). These biocompatible, piezoelectric KNLN composite films combine the best of both worlds; the coercive field and the Curie temperature are dominated by that of the KNLN ceramics, while due to the low loading levels the mechanical properties resemble those of PDMS.

The composite films have been integrated into a flexible touch sensor. We have demonstrated the high sensitivity of the sensor under a controlled dynamical change of applied force via measuring the open circuit voltage, and by finger tapping a load matched and amplified flexible touch patch. Composite films, comprising aligned piezoelectric particles in a polymer matrix, are straightforward to fabricate. Hence, we anticipate that implementation of this approach will lead to new flexible sensor systems for temperature, infrared, impact and torque measurements. The developed sensor can replace brittle ceramic sensors and, therefore, can be applied in many fields where flexible electronics are needed, such as medical diagnostics and wireless sensors networks.

APPENDICES

3.A. SUPPORTING INFORMATION

VIDEOS can be viewed in the online Supporting Information [65].

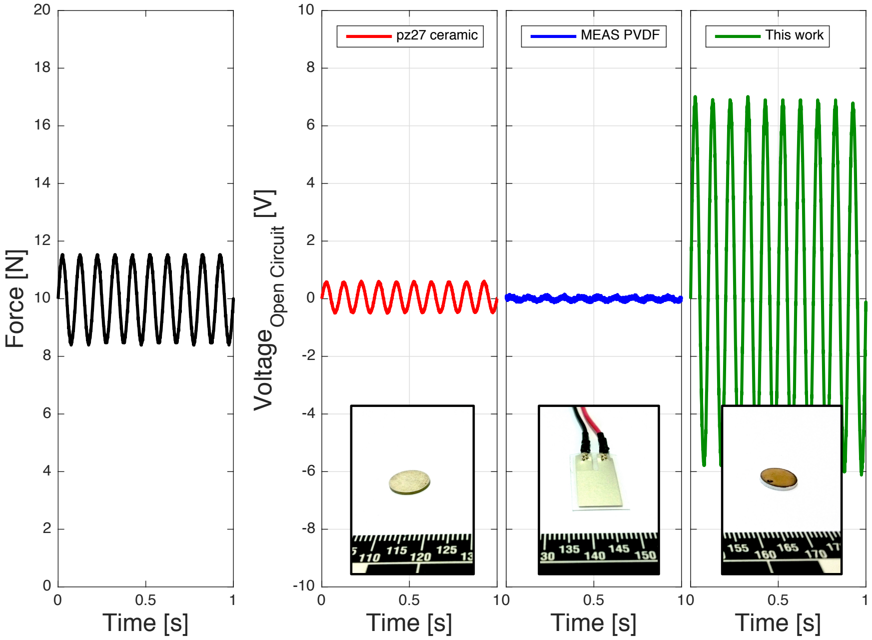

Figure A1: Open circuit voltage output of an aligned 10 vol.% KNLN-PDMS composite disk (8.7 mm diameter and 1.1 mm thickness) compared to a commercial pz27 ceramic disk (8.9 mm diameter and 1.0 mm thickness) and a commercial PVDF polymer component (10 by 15 mm active area and 30 μm active thickness) due to a 3 N peak to peak sinusoidal excitation at 10 Hz and 23 °C.

3.B. POLING STUDY

Composites of piezoceramic particles in a polymer matrix are promising materials for flexible energy harvesting and sensing applications due to their ease of processing matched with favorable mechanical properties and low dielectric loss [19, 94]. Existing piezoelectric materials, based on lead zirconium titanate (PZT) ceramics, raise ecological concerns and demonstrate poor mechanical properties with typically high stiffness (≈60 GPa) and low strain at break, limiting their application within curved devices [19]. PVDF polymer based piezoelectrics demonstrate favorable piezoelectric performance at stiffnesses of 1 GPa, yet continue to exhibit high dielectric losses above 5 vol.% [94]. In piezoceramic-polymer composites the electrical and mechanical performance can be tailored by adjusting the composition, internal structure and volume fraction of the two phases [30]. Composites with perfect particle connectivity, or a '1-3' structure, have been shown to attain significantly increased performance, yet require complex processing, in the form of ceramic fiber spinning and sintering, to produce and sacrifice mechanical performance. Random piezoceramic-polymer composites, or '0-3' composites, the simplest type of composite to process and mold into predesigned shapes, tend to demonstrate significantly reduced piezoelectric performance due to the greater distance between particles, or inter-particle distance. Structuring the ceramic particles within the polymer matrix by application of dielectrophoresis (DEP) has been shown to significantly decrease the inter-particle distance in composites, improving the piezoelectric and dielectric performance with respect to random composites, preserving their relative ease of processing [39]. A further concern influencing the piezoelectric performance of these composites is the degree of poling of the ceramic phase. Piezoelectric particulate-polymer composites require high poling fields (on the order of 10 - 15 kV/mm at temperatures above the polymer T_g) to achieve sufficient poling. The poling electric field acting on each particle is influenced both by the ratio of the conductivity and the ratio of the dielectric constant of the two phases [33]. The effective electric field the ceramic phase experiences tends to be only a fraction of the applied electric field, due to the low dielectric constant of the polymer matrix. Though, in composites based on lead free piezoceramics this limitation can be relatively overcome due to the reduced dielectric constant of lead free ceramics compared to lead based ceramics. At poling times longer than the relaxation time of the composite, the distribution of the electric field will be dominated by the ratio of the conductivities of the two phases instead of the dielectric constants [95]. To attain an effectively poled piezoceramic-polymer composite, it has been demonstrated that the poling time should be longer than the relaxation time of the composite [95]. Yet, fine-tuning of the exact poling conditions of a particular piezoceramic-polymer composite should still be investigated empirically. In the preceding sections, it was demonstrated that composites based on (K,Na)NbO_3 fillers doped with Li (KNLN) have increased piezoelectric performance when compared to similar lead containing composites. In this section, the effective poling conditions to come to optimal performance in a flexible, lead free KNLN polydimethylsiloxane (PDMS) piezoelectric structured composite are investigated and compared with random composites.

This appendix has been published in Ferroelectrics, (2017) [66]

POLING CONDITIONS

Effective poling conditions for the cured KNLN-PDMS composites are studied by poling and repoling the same structured and random samples, over and over again for each poling parameter (electric field, poling time and temperature) under investigation. All composites were poled in a silicone oil bath at temperatures varying from 25 to 150 °C, for times varying from 2 to 30 min, and electric fields varying from 5 to 20 kV/mm. The composite samples were cooled to room temperature in the presence of the electric field, and aged for at least 24 hours before piezoelectric and dielectric measurements took place.

RESULTS AND DISCUSSION

The effect of the applied poling electric field, E, on the piezoelectric charge coefficient,d_{33}, of KNLN-PDMS composites is presented in Fig. B1a. The samples were poled at a fixed temperature and time of 150 °C and 30 min. The piezoelectric charge coefficient of the composites increases with electric field, until 10 kV/mm after which performance degrades. We observed that the dielectric constant of all composites degrades as a consequence of the poling trial from 9.9 to 7.2 in structured, and 6.7 to 5.9 in random. The

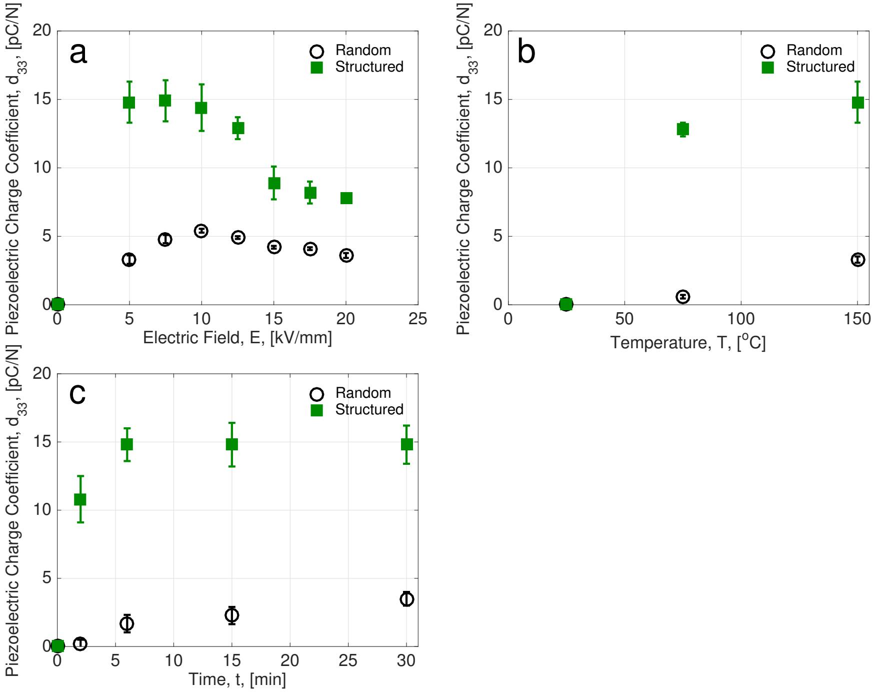

Figure B1: Effect of poling conditions on piezoelectric charge coefficient, d_{33}, of KNLN-PDMS composites. (a) Piezoelectric charge coefficient, d_{33}, as a function of electric field, E [kV/mm], poled at 150 °C for 30 min. (b) d_{33} as a function of poling temperature, T [°C], poled at 7.5 kV/mm for 30 min. (c) d_{33} as a function of poling time, t [min], poled at 7.5 kV/mm and 150 °C. Open circles represent randomly dispersed composite films, prepared without dielectrophoretic field. Solid squares represent dielectrophoretically aligned films.

decrease in performance, more pronounced in structured composites, suggests degradation of the polymer matrix. Since the inter-particle distance in structured composites is shorter, the polymer matrix between these particles experiences a relatively high local electric field. Re-poling composites at lower fields did not recover optimal performance. The optimal poling condition for random composites lags behind that of structured composites, reaching a maximum in piezoelectric charge coefficient at 10 kV/mm for random, and 7.5 kV/mm for structured. The effects of poling temperature, T, are shown in Fig. B1b, at a fixed time of 30 min and an electric field of 7.5 kV/mm. The piezoelectric charge coefficient of both types of composite increases with temperature up to 150 °C, after which the polymer matrix degrades. The effect of the poling time, t, on the piezoelectric charge coefficient d_{33} is presented in Fig. B1c. The piezoelectric charge coefficient of all composites increases with poling time. In structured composites, poling saturation is reached after 6 min, while in random composites improvement can be seen up to 30 min. Effective poling conditions found for structured composites are 7.5 kV/mm for 6 min at 150 °C, and random: 10 kV/mm for 30 min at 150 °C. Effective poling conditions are found at a lower field and time than in random composites, due to the improved inter-particle distance in the structured composites. The average dielectric constant of the optimally poled KNLN-PDMS composites was 5.9 and 8.6 for random and structured, respectively, with an average dielectric loss of 1.5 % each.

CONCLUSIONS

Effective poling conditions are identified at 6 min, 150 °C, and 7.5 kV/mm for structured and 10 kV/mm for random composites with improvements up to 30 min. Further increases in temperature lead to degradation of the polymer matrix. Increases in poling time have no demonstrable effect in structured composites, while increasing the electric field only reduces piezoelectric performance by degradation of the polymer matrix.

4

TOWARDS ROLL TO ROLL UPSCALING OF DIELECTROPHORETICALLY STRUCTURED COMPOSITES

I just wish the world was twice as big,
and half of it was still unexplored.

Sir David Attenborough

Implementation of dielectrophoretic structurization to improve the performance of low volume fraction piezoelectric ceramic-polymer composites is held back by the lack of a suitable upscaling scheme. In this chapter a potential upscaling scheme is explored based on tape casting a composite of a photocurable urethane dimethacrylate (UDMA) polymer and a well-studied piezoceramic, of lead zirconium titanate (PZT) particles. Dielectrophoretic alignment is successfully achieved in 10 vol.% PZT-UDMA composites prepared in a roll-to-roll upscalable way. Due to the moving electric field the orientation of the achieved chains is horizontal, parallel to the direction of the blade movement. Piezoelectric performance of the horizontally structured composites is identical to that of field-free tape casted composites, due to the inadequacy of the available poling schemes and electrode application methods. To show the potential of integrating these upscalable piezoelectric composites as touch sensors, a technology demonstrator was prepared based on a randomly dispersed 50 vol.% PZT-UDMA composite.

Parts of this chapter have been published in Ferroelectrics **480**, 1 (2015) [67].

4.1. INTRODUCTION

DIELECTROPHORETIC alignment of piezoelectric particles in electroceramic-polymer composites was first demonstrated by Bowen *et al.* in 1998 at Penn State Unviersity [37] by applying an oscillating electric field over the composite in its viscous state, inducing the particles to form into chains. Seven years later Wilson *et al.* at Cranfield University [38] demonstrated the improved piezoelectric charge coefficient of structured composites, with respect to random composites. Since 2005 a wide range of piezoelectric filler-polymer composites have been shown to achieve performance improvements due to the application of a dielectrophoretic alignment (DEP) field [39, 40, 96, 97].

Even though the figure of merit for touch sensing, the piezoelectric voltage sensitivity (g_{33}), of structured composites is significantly higher than most piezoelectric ceramics, structured piezoelectric composites have yet to be implemented in actual products since a suitable processing scheme has yet to be developed. The ALGRA company (Switzerland) has developed a method to print random composites in an upscalable way, via roll to roll printing. For structured nanoparticle composites, a discontinuous roll to roll production scheme has been developed by Cakmak *et al.* [96]. To attain vertical alignment, their process must be disrupted by placing an indium tin oxide (ITO) deposited polyethylene terephthalate (PET) foil on top of the pre-casted composite for application of the DEP field. After which the composites are subjected to UV to cure, followed by a post curing thermal treatment. The laboratory scale processes that have been used to make dielectrophoretically structured composites mix a piezoelectric powder with a two-component polymer (such as epoxy [38–40, 97], polyurethane [97, 98], or polydimethylsiloxane (Chapter 4)). The mixture is cured at elevated temperatures for up to four hours while the particles align, due to the application of a DEP field. To attain high-volumes of material at low-cost, this lengthy process is obviously unsuited.

In this chapter we will therefore explore the use of a photocurable polymer to find a new and simpler route for making structured piezoelectric composites. A photocurable polymer matrix allows for relatively fast curing times, compared to thermally curing polymers, facilitating higher production speed and possible roll to roll production. The principal aim is to understand whether this new process will generate structures with sufficient piezoelectric performance for application as a touch sensor.

4.2. EXPERIMENTAL PROCEDURE

4.2.1. UPSCALING PROCESS

TO facilitate upscaling trials, a well studied piezoelectric ceramic Pb(Zr,Ti)O_3 (PZT) particulate powder (PZT-5A4, Morgan Electroceramics, Ruabon, UK) was chosen as the filler material to be combined with a photocuring polymer matrix. The PZT particulate powder was calcined at 1150 °C for 1 hour and dry milled for 2 hours with 5 mm Y-stabilized ZrO_2 balls. The powder was then sieved, dried for 12 hours at 150 °C, and stored under vacuum conditions at room temperature. The particle size distribution of d10 = 1.0 μm, d50 = 1.9 μm and d90 = 4.2 μm was measured in an aqueous solution by laser diffraction with a Beckman Coulter LS230.

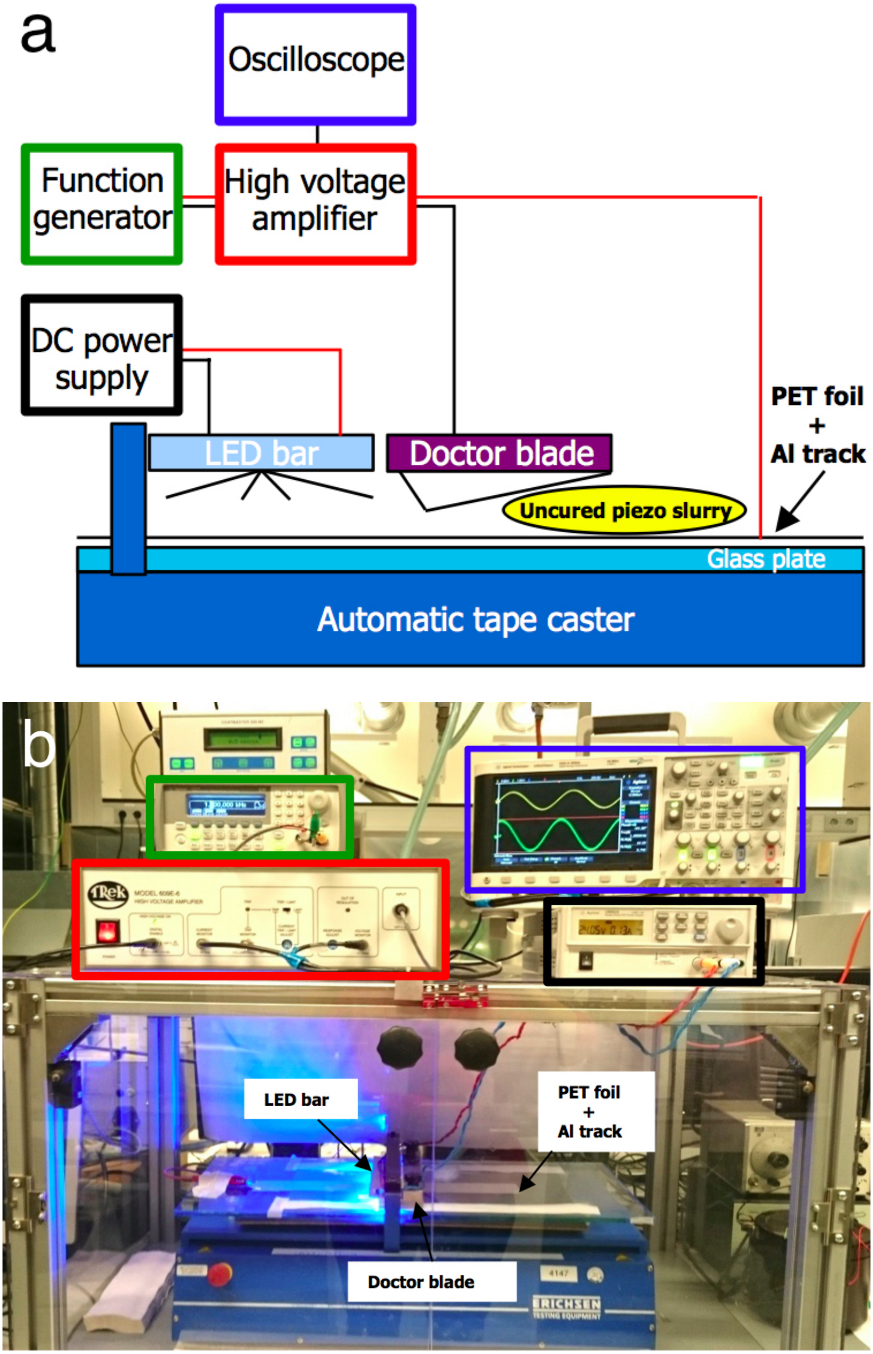

Figure 4.1: Setup for processing of both random and dielectrophoretically structured PZT - UDMA composites in a roll to roll upscalable way, showing (a) a schematic representation and (b) a photograph of the setup in action.

A matrix of urethane dimethyacrylate - 1,6 hexanediol dimethacrylate (UDMA) copolymer, photo-curable with the addition of a camphorquinone (CQ) photoinitiator and dimethylaminoethyl-methacrylate accelerator (Esstech, Inc.), was chosen. This UDMA copolymer has demonstrated the ability to accommodate high volume fractions of filler [99], a relatively quick curing time of 3 s [100], and has been successfully applied to develop electrorheologically structured composites [101].

Piezoelectric UDMA composites were prepared by mixing PZT5A4 particulate powder with UDMA copolymer in a speedmixer (DAC 150FV, Hauschild, Germany), at PZT volume contents between 0 and 50 vol.%. The composites were cast on Al tracks, adhered to a PET foil, at 100 - 200 μm thickness using an Erichson tape caster (see the schematic and photograph of the setup in Fig. 4.1). To prepare dielectrophoretically structured composites, an oscillating electric field of 1 kV/mm at the optimal frequency of 1 kHz was applied between the Al track and the doctor blade. Immediately after tape casting, the composites were photocured within one minute (depending on filler volume) using blue LED's (LEDtuning, the Netherlands) at 15.5 W at 0.333 mm/s (the experimentally found optimal conditions for achieving homogeneous, cured, films). Vertically structured PZT - UDMA reference samples were prepared in a teflon mold (see Fig. 4.2) with a transparent hot electrode of ITO deposited on PET foil and a Cu tape track to ensure homogeneous transfer of the electric field). The transparent top electrode allowed photocuring to take place while the structuring field of 1 kV/mm at 1 kHz was on. All composites were post cured for one hour at 150 °C to remove any remaining monomer. Gold electrodes of 20 nm thickness were applied using a (Balzers Union SCD40) sputter coater. The samples were either conventionally poled by application of an electric field in a Si oil bath for one hour at 100 °C and 10 kV/mm or 'in-situ' poled during fabrication and curing. All measurements were performed at least 24 hours after poling.

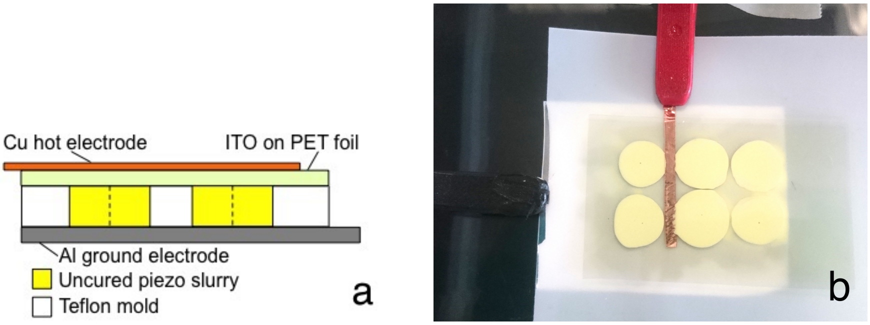

Figure 4.2: Setup for processing of vertically aligned, dielectrophoretically structured, PZT - UDMA composite reference samples, showing (a) a schematic representation (side view) and (b) a photograph of the top view.

4.2.2. MEASUREMENT METHODS

The piezoelectric charge coefficient, d_{33} [pC/N], was measured with a PM300 Berlincourt type piezometer (Piezotest, United Kingdom). The capacitance, C [pF], was measured at 1 kHz and 1 V with an Agilent 4263B LCR (Santa Clara, CA, USA). The ε_{33} was derived from the capacitance. The Young's modulus, E_{33} [GPa], of the UDMA was measured from uniaxial tensile tests of five dog bone samples using an Instron Model 3365 tensile tester equipped with a 1 kN load cell. Temperature dependent electrical measurements were performed using a broadband dielectric spectrometer (Novocontrol, Germany) paired with an Agilent E4991A (Santa Clara, CA, USA) impedance analyzer set to an oscillating voltage of 1 V and a cryostat high temperature sample cell. Micrographs of the cross-section, side view and top view of the PZT-UDMA composites were recorded using a field-emission scanning electron microscope (SEM) (JEOL, JSM-7500F). The ferroelectric polarization was measured at the Max Planck Institute for Polymer Research in Mainz, Germany, using a Radiant technologies Precision Multiferroic Test System at 1 Hz, under a double bipolar triangular pulse with a peak field from 0 to 50 kV/mm.

4.3. RESULTS AND DISCUSSION

PROPERTIES of random PZT-UDMA composites prepared at volume contents from 10 to 50 vol.% are given in subsections 4.3.1 to 4.3.3, while the results of structured composites, only prepared at 10 vol.%, will be shown from subsection 4.3.4 on.

4.3.1. RANDOM COMPOSITE MICROSTRUCTURE

The microstructures of the cross-section of tape casted and photo-cured random PZT-UDMA composites are shown in SEM micrographs presented in Fig. 4.1 and 4.2. At all volume fractions, the particle dispersion appears to be relatively homogeneous. There are no visible voids in the tape cased composites nor is there sedimentation of the particles.

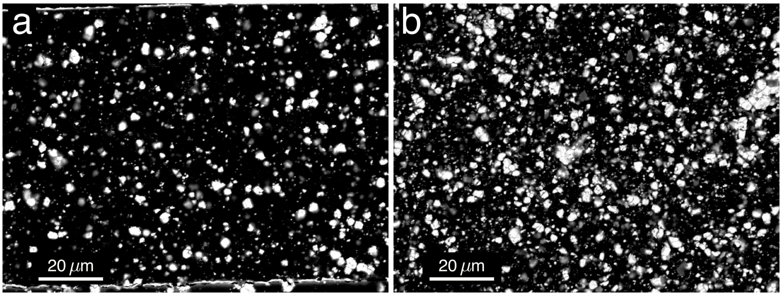

Figure 4.1: SEM micrographs of the cross-section of tape casted and photo-cured PZT-UDMA composites. (a) 10 vol.% and (b) 20 vol.% random composites at x1000 magnification.

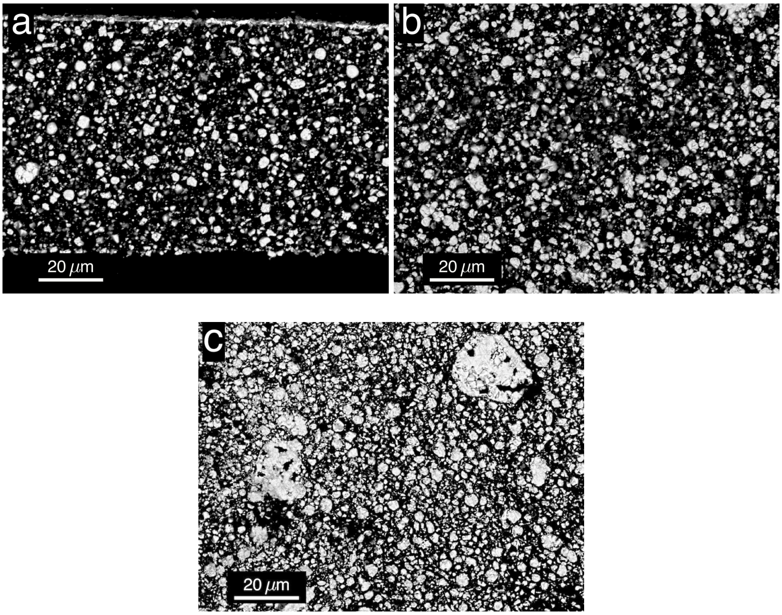

Figure 4.2: SEM micrographs of the cross-section of tape casted and photo-cured PZT-UDMA composites. (a) 30 vol.%, (b) 40 vol.% and (c) 50 vol.% random composites at x1000 magnification.

4.3.2. DI- AND PIEZOELECTRIC PROPERTIES OF RANDOM COMPOSITES

The high field polarization of random PZT-UDMA composites is presented in Fig. 4.3, as measured. With increasing volume content, the remanent polarization increases. The 10 vol.% composite exhibits almost linear behavior up to a field of 50 kV/mm, after which electrical breakdown occurred. The coercive field of the remaining composites varies between 5 - 6 kV/mm. Further increases to the applied electric field lead to dielectric breakdown of the composites containing 20 - 40 vol.%. The 50 vol.% composite could withstand higher fields, and attained a maximum remanent polarisation of 1.6 μC/cm^2 (Fig. 4.3b).

The dielectric and piezoelectric properties of the random PZT-UDMA composites are presented in Fig. 4.4 along with quantitative fits of the data, calculated via the Yamada analytical model (described in Chapter 3, Eq. 3.3 and 3.4). The overall performance is in good agreement with expectations from the model. The shape fitting factors, n, were determined by the least square fitting method, and come to n = 6 for the dielectric constant, and n = 5 for the piezoelectric charge coefficient with an assumed poling efficiency of 1. While the piezoelectric voltage coefficient of similar structured low volume composites is typically higher, the g_{33} at 50 vol.% of 39 mV.m/N is sufficient for operation as a touch sensor, depending on component design and available area. Fabrication of this type of random composite could easily be transferred to high volume roll-to-roll production.

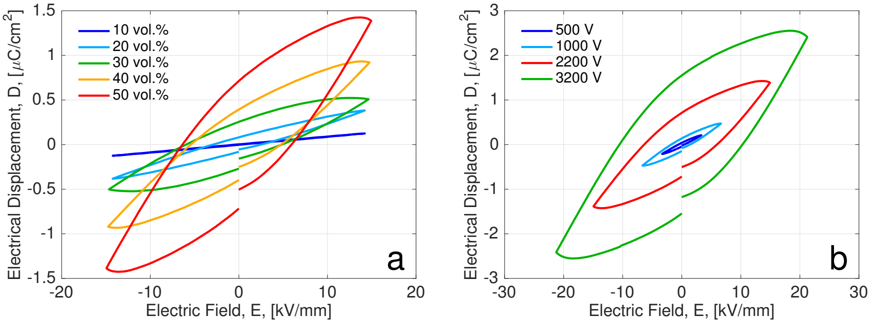

Figure 4.3: Hysteresis loops of tape casted PZT-UDMA composites. (a) Hysteresis loops of PZT-UDMA composites, containing 10 to 50 vol.% PZT, as a function of electric field, E, measured at a maximum applied electric field of 15 kV/mm. (b) Hysteresis loops of 50 vol.% PZT-UDMA composites as a function of electric field, E. The applied maximum field is increased in large steps, indicated by the bias given in the legend.

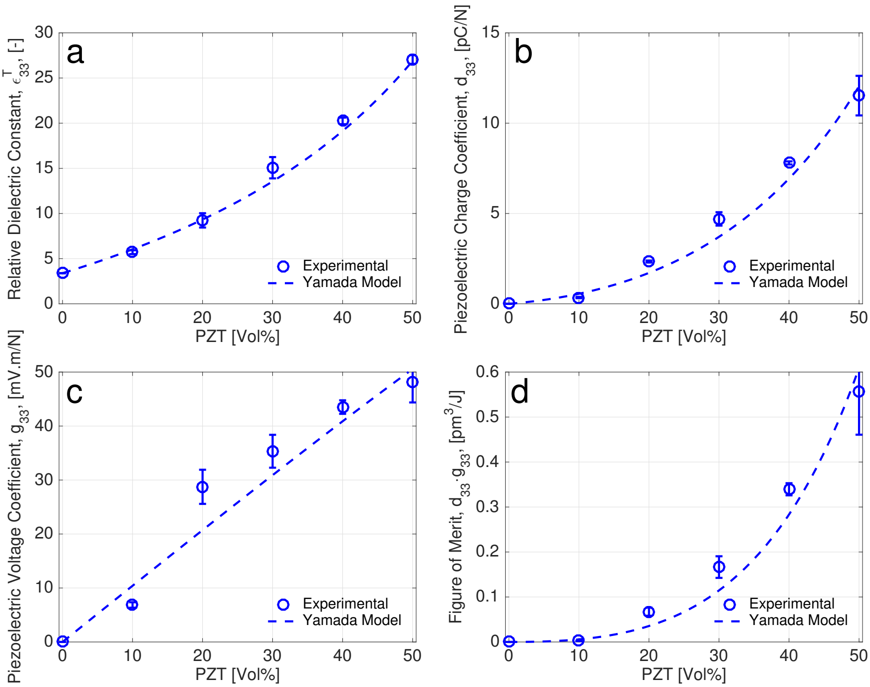

Figure 4.4: Piezoelectric constants of tape casted PZT-UDMA composites. (a) Relative dielectric constant, ε_{33}^{T}, as a function of PZT content. (b) Piezoelectric charge coefficient, d_{33}, as a function of PZT content. (c) Piezoelectric voltage coefficient, g_{33}, as a function of PZT content and (d) Figure of merit, $d_{33} \cdot g_{33}$. Open circles represent randomly dispersed composites, prepared without dielectrophoretic field. Dashed lines are quantitative fits to the data, calculated with the Yamada analytical model.

4.3.3. TECHNOLOGY DEMONSTRATOR

A piezoelectric unimorph based on a large area 50 vol.% PZT - UDMA composite, depicted in Fig. 4.5, was prepared to demonstrate the touch sensitivity and ease of integration of these composites. The unimorph composite was encapsulated in a PET foil, with Cu leads, to protect the Au electrodes from incidental wear and for ease of handling. The encapsulated piezoelectric component combined with an electroluminescent panel was workshopped into a prototype of the DIFFUS design "EAT" (Enhancing Appetite Tableware) product, which emits light when changes in pressure are detected due to cutting food and picking up the tableware on the smart placemat (Fig. 4.6). The performance of the high volume content PZT - UDMA composite has been demonstrated to be suitable for touch sensing, and retains an ease of integration, due to its relative low stiffness, for product prototyping.

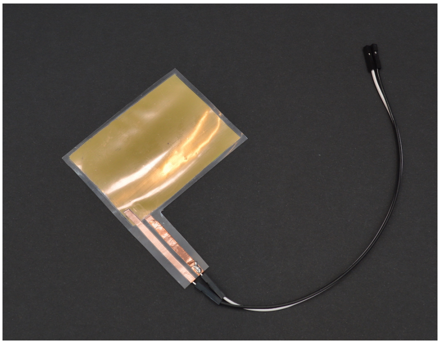

Figure 4.5: Encapsulated piezoelectric component based on a unimorph 50 vol.% PZT - UDMA composite.

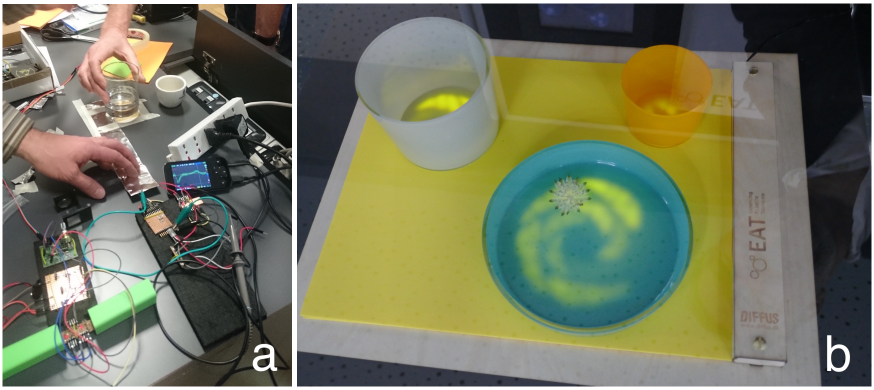

Figure 4.6: Integrating the 50 vol.% PZT - UDMA composite technology demonstrator, showing (a) the prototyping session and (b) the final product developed by DIFFUS design "EAT" (Enhancing Appetite Tableware).

4.3.4. TAPE CASTING WITH DIELECTROPHORESIS

Dielectrophoretically structuring piezoelectric composites with a moving electric field leads to horizontal orientation of the piezoelectric particles in the polymer matrix. The alignment is parallel to the direction of blade movement, as is clear from micrographs of the side view of 10 vol.% random composites compared to structured composites (Fig. 4.7). Horizontal alignment is also apparent from the top view (Fig. 4.8). Regardless of whether the doctor blade functions as the hot or ground electrode, horizontal alignment is present in all dielectrophoretically structured composites prepared with a moving electric field.

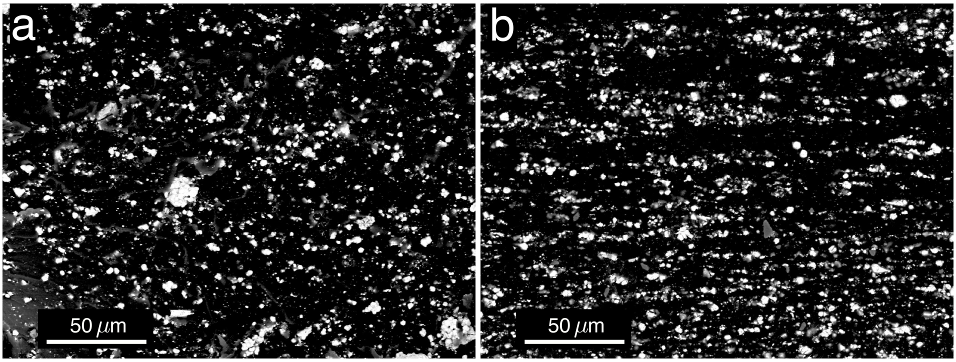

Figure 4.7: SEM micrographs of the side view of 10 vol.% (a) random and (b) horizontally structured PZT-UDMA composites at x500 magnification.

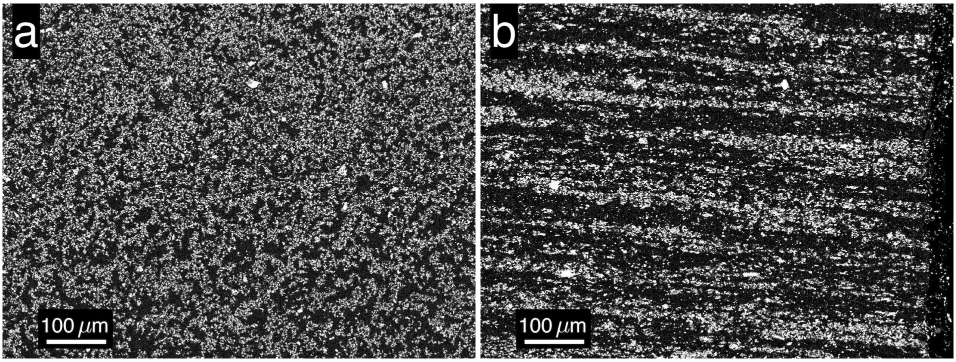

Figure 4.8: SEM micrographs of the top view of 10 vol.% (a) random and (b) horizontally structured PZT-UDMA composites at x150 magnification.

Altering the ground electrode pattern has little to no effect on the direction of alignment (see Fig. 4.9 of the top view of one such experiment). Reduction in blade movement speed, to allow more time for chain alignment to occur, leads to inferior film quality. Increasing the light intensity, to speed up the polymer cure, leads to the composite curing on the blade itself, rather than casting a film.

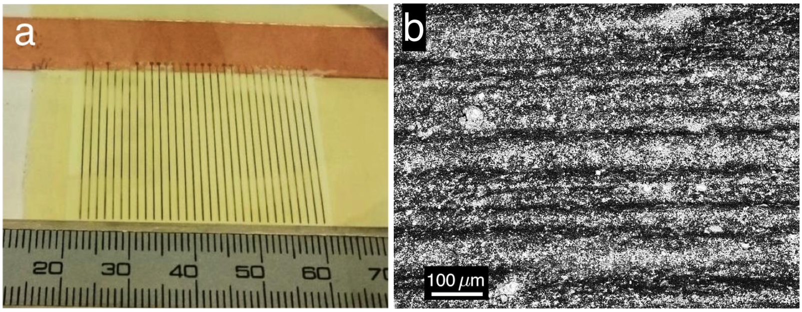

Figure 4.9: Example of an altered ground electrode (a) for tape casting a structured 10 vol.% PZT - UDMA composite showing the top view and the microstructure (b) from SEM at 150x magnification.

4.3.5. POLING HORIZONTALLY STRUCTURED COMPOSITES

Ideally, structured composites should be poled parallel to the direction of the aligned chains. In vertically aligned and parallel plate electrode (PPE) poled composites one can expect, based on established analytical models (see Chapter 3, Eq. 3.5 and 3.6), a significantly improved piezoelectric performance compared to random composites, as shown in Fig. 4.10 [37, 39].

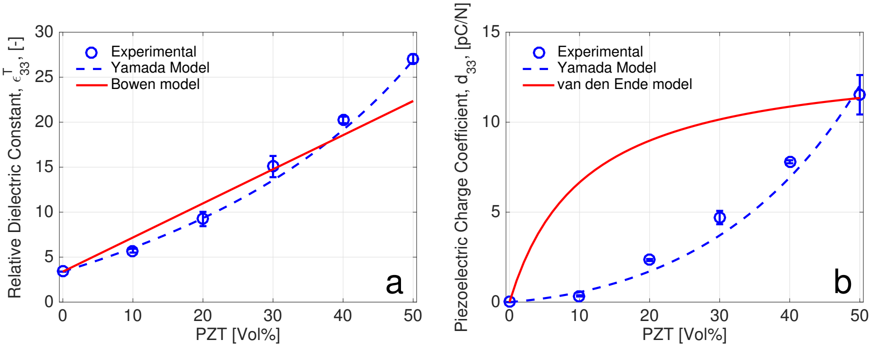

Figure 4.10: Piezoelectric constant estimates of dielectrophoretically aligned PZT-UDMA composites. (a) Relative dielectric constant, ε_{33}^{T}, as a function of PZT content. (b) Piezoelectric charge coefficient, d_{33}, as a function of PZT content. Open circles represent randomly dispersed composites, prepared without dielectrophoretic field. Dashed lines are quantitative fits to the data, calculated with the Yamada analytical model. Solid lines are estimates of the dielectric and piezoelectric constants, calculated via the Bowen model [37] and van den Ende model [39], respectively.

Horizontal alignment is far from ideal to attain efficient poling of the piezoelectric particles in these composites. The most efficient electrode pattern for poling would be PPE covering either end of the particle chains, yet due to the low thickness of the composite films (100 - 200 μm) this is not practical. Consequently, PPE are applied on the top and bottom of the composites, poling perpendicular to the direction of chain alignment. The horizontally structured composites were poled both conventionally (in an oil bath, with PPE) and in-situ (applying a DC bias during tape casting, and measuring with PPE). Vertically structured composites, prepared without a moving electric field, are also poled conventionally and in-situ, and serve as a reference. The piezoelectric performance of the horizontally structured composites under vertical actuation is identical to that of random composites (Table 4.1). The performance of the vertically structured composites is comparable to structured PZT - epoxy composites with a d_{33} of ≈7 pC/N [57], and in line with expectations from the analytical models (Fig. 4.10). Poling horizontally structured composites perpendicular to the direction of chain alignment, while a practical solution, leads to poor piezoelectric performance. The electric field experienced by the ceramic particles in the chains is essentially identical to that of a random composite.

Table 4.1: Effect of poling conditions on the ε_{33}^{T} and d_{33} of random and structured 10 vol.% PZT UDMA composites.

Poling conditions		Random	Vertically structured	Horizontally structured
Conventional	ε_{33}^{T} [-]	6.7 ± 0.44	8.8 ± 1.2	6.6 ± 0.34
	d_{33} [pC/N]	1.1 ± 0.04	6.7 ± 0.05	1.2 ± 0.05
In situ	ε_{33}^{T} [-]	6.6 ± 0.37	8.5	6.9 ± 0.75
	d_{33} [pC/N]	0.45 ± 0.10	7.5	0.52 ± 0.15

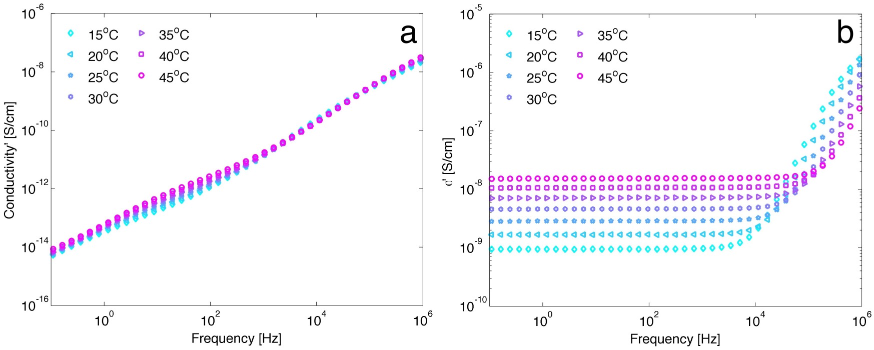

Figure 4.11: Near room temperature conductivity of neat UDMA polymer (a) before and (b) after photocuring.

In-situ poling of the composites, where the particles experience an in-plane alignment field, matched with an in-plane DC poling bias, could be a viable method to achieve 'horizontal' poling. During in-situ poling, the polymer matrix is not yet fully cured, and has a conductivity more than 6 orders of magnitude higher (Fig. 4.11) than in its cured state. For poling times shorter than the relaxation time of the composite, the effective electric field experienced by the particles is governed by the relation: $E_{effective} = 3\varepsilon_m/(\varepsilon_p + 3\varepsilon_m) \cdot E_{applied}$ [102], while for longer times, it is governed by the ratio of the electrical conductivities ($\sigma_m : \sigma_p$) [33]. If the composites are poled long enough, the higher conductivity could potentially lower the field required to efficiently pole the piezoelectric particles [97]. Yet, at a d_{33} of only ≈ 0.5 pC/N in the in-situ poled horizontally structured composites, it is clear that the benefits of in-situ poling have not been able to overcome the practical constraints. Each tape casting experiment only lasts 5 minutes, at the tape casting speed of 0.33 mm/s, and since the tape casting is performed in air, the highest achievable poling field was only 1.2 kV/mm (applied as a DC bias, during dielectrophoresis). In contrast, the vertically structured composites were in-situ poled for a full 30 minutes at room temperature, and have achieved a d_{33} of 7.5 pC/N.

Finally, interdigitated electrodes (IDE) could be applied to pole the horizontally structured composites in-plane. Yet, previous studies have shown that this leads to a piezoelectric performance of only 10 % that achieved in vertically structured and PPE poled composites [103]. Not only do the IDE fingers obscure large portions of the composite from experiencing a poling field, the poling field is not truly in-plane, and rounds off as it approaches the IDE fingers [104].

4.3.6. TIME REQUIRED FOR DIELECTROPHORETIC ALIGNMENT

To investigate the underlying cause of the horizontal alignment, additional experiments were carried out to ascertain the time required for dielectrophoretic alignment based on three different particle aspect ratios and sizes.

Table 4.2: Required alignment time for three different PZT particle sizes and aspect ratios.

Particle type	PZT particles	PZT thin fibers	PZT thick fibers
Particle diameter	1.9 μm	40 μm	400 μm
Particle aspect ratio	≈1	≈4	≈5
Time to align [s]	≈180	≈7	≈2

In theory, the dielectrophoretic alignment of high dielectric particles in a low dielectric matrix should take only a matter of seconds [85]. In practice, however, much larger time scales are evident. To empirically examine the relationship between particle aspect ratio and alignment time, two types of short PZT fibers were sintered at 1200 °C, mixed at 2 vol.% with the UDMA copolymer and allowed to align into chains between two Cu electrodes spaced 1 mm apart (for more details on the fiber production see Van den Ende *et al.* 2012 [98]). The time required for alignment was also measured for 2 vol.% PZT particle - UDMA composites. Alignment speed was monitored with an optical microscope, and the averaged results are presented in Table 4.2. The particles are classified as aligned when no further particle movement can be optically distinguished.

Both short fiber types require only seconds to align into chains while the particulate powder, used in all upscaling experiments, requires up to 3 minutes to align. This 3 minute alignment time is incompatible with the production speed of 2 cm per minute photocuring speed required to come to homogeneous films. To ensure vertical alignment, the hot and ground electrodes should be in sync for at least 3 minutes. This could be achieved if the doctor blade would move 5 mm (the length of the flat surface of the doctor blade) every 3 minutes, and stay still to allow for chains to form. Yet, moving the blade in this stop-start-stop pattern leads to severe film inhomogeneity, with a risk of photocuring the composite on the blade itself. Still, the measured timescales indicate that particles with an increased aspect ratio could allow for vertical alignment in tape casted composites.

4.4. CONCLUSIONS

A new method for upscalable processing of piezoelectric PZT-UDMA composites via tape casting and immediate photocuring is presented. Random composites with 50 vol.% of PZT filler are prepared at a speed of 0.5 mm/s, and can be integrated in products to perform as touch sensors. Dielectrophoretically structured composites prepared with a moving doctor blade achieve horizontal alignment, parallel to the direction of blade movement, both from the side view and top view. Yet, the piezoelectric performance of these PPE poled structured composites is identical to random composites of similar volume content. Decreasing the time required for chain alignment, by altering the piezoelectric particle morphology and/or composition could potentially lead to vertically structured composites produced with a moving electric field. Considering the upscalability and relative performance of the high volume PZT - UDMA composites, these materials may still be considered as a relatively cheap and formable alternative to sintered PZT ceramics for sensing applications.

5

EXPLORING THE PIEZOELECTRIC PERFORMANCE OF PZT PARTICULATE-EPOXY COMPOSITES LOADED IN SHEAR

If you liked it,
then you should have put a ring on it.

Beyoncé Knowles

The active and passive piezoelectric response of lead zirconium titanate (PZT)-epoxy particulate composites loaded in shear is studied using analytical models, a finite element model and by experiments. The response is compared to that of the same composites when loaded in simple tension. Analogously to bulk PZT, particulate PZT-polymer composites loaded in shear show higher piezoelectric charge coefficient (d_{15}) and energy density figure of merit (FOM_{15}) values compared to simple tension (d_{33}) and (FOM_{33}). This outcome demonstrates the as-yet barely explored potential of piezoelectric particulate composites for optimal strain energy harvesting when activated in shear.

This chapter has been published in Smart Materials and Structures **25**, (2016) [68]. The numerical work was carried out by F. Van Loock as a part of his M.Sc. thesis, under the author's supervision [105].

5.1. INTRODUCTION

OVER the last decade, energy harvesting systems based on piezoelectric devices have attracted considerable interest in applications where battery replacement is highly inconvenient or even impossible such as medical implants, remotely located sensors in aircraft structures and tire pressure monitoring systems [71, 106–108]. Piezoelectric energy harvesters convert mechanical waste energy into useful electrical energy by employing the active material's direct piezoelectric effect. The relationship between the input mechanical and output electrical energy is described by the piezoelectric charge coefficient (d_{ij} $[pC/N]$) where the indices describe a specific piezoelectric operation mode. The i-index indicates the orientation of the electrical port, and the j-index refers to the direction of the mechanical port with respect to the direction of the applied load. For the most frequently studied and commercially available piezoelectric materials, based on lead zirconium titanate ($\mathrm{Pb(Zr_xTi_{(1-x)}O_3}$) or PZT, these modes are known as the longitudinal (d_{33}), transverse (d_{31}), and shear (d_{15}) mode, and the absolute values of these coefficients generally follow the subsequent order: $d_{15} > d_{33} >> d_{31}$ [3, 8, 9]. To compare the energy harvesting performance of piezoelectric materials it is convenient to determine the generated electrical energy per volume, or energy density, of the material irrespective of the efficiency at which the output energy is produced. The appropriate energy density figure of merit (FOM_{ij} $[m^3/J]$) is the inverse piezoelectric stress energy density constant, directly related to d_{ij} and dielectric constant (ε_{ii} [-]), under stress-driven loading of the active material via: $W_{ij}^T = FOM_{ij} \cdot T^2 = d_{ij}^2/\varepsilon_{ii} \cdot T^2$, where maximizing FOM_{ij} maximizes the actual stress energy density W_{ij}^T $[J/m^3]$ for a given stress state T [Pa] [8, 109].

Although PZT material systems have become the standard material for piezoelectric energy harvesters because of their high piezoelectric coupling and temperature stability, their inherent brittleness makes them not directly suitable for high strain resistant and/or complex shaped piezoelectric energy harvesting applications [57, 110, 111]. An attractive solution for this material selection problem is provided by compliant, relatively cheap and easy to produce piezoelectric particulate (0-3) ceramic-polymer composites [30, 112]. These piezoelectric particulate composites consist of randomly dispersed piezoelectric particles (active phase) in a polymer matrix (passive phase). Piezoelectric particulate composites show potential for compliant energy harvesting devices as they come with tunable and advantageous mechanical properties such as high compliances, high toughnesses, and high yield strains even at moderate particle volume fractions [57, 112, 113]. However, it has been demonstrated that composites with randomly dispersed piezoelectric particles are characterized by relatively low piezoelectric coupling properties [111], which can be overcome to some extent by imposing a form of structuring to the particles [57, 112]. Irrespective of structuring the composites, in order to obtain harvesting systems with sufficient electrical energy yields, the active material must be used to its fullest extent. Analysis of the magnitudes of the various piezoelectric constants d_{ij} for bulk PZT ceramics suggests that this can be achieved by quasi-statically loading the harvesting device in its shear or d_{15} mode. The potential of energy harvesters employing the shear mode has been investigated in the literature for PZT ceramics operating at resonance [114–116]. However, the shear mode quasi-static activation of particulate composites has not yet been explored.

Hence, the present work aims to investigate the unexplored shear mode properties of random (0-3) piezoelectric particulate composites, focusing on a PZT-epoxy system, by a combined analytical, numerical and experimental approach.

5.2. THEORY

5.2.1. PIEZOELECTRIC CONSTITUTIVE EQUATIONS

THE reversible electromechanical coupling of piezoelectric materials is described by the linearized piezoelectric constitutive equations of the strain $\overline{S}$ [-], stress $\overline{T}$ [Pa], dielectric displacement $\overline{D}$ $[C/m^2]$, and electric field $\overline{E}$ $[V/m]$ state vectors [1, 9].

$$\begin{bmatrix} \overline{S} \\ \overline{D} \end{bmatrix} = \begin{bmatrix} \overline{\overline{s}} & \overline{\overline{d}}^{t} \\ \overline{\overline{d}} & \overline{\overline{\varepsilon}} \end{bmatrix} \begin{bmatrix} \overline{T} \\ \overline{E} \end{bmatrix} \tag{5.1}$$

where $\overline{\overline{s}}$ $[\mathrm{Pa}^{-1}]$ is the material's compliance matrix. The elements of the electromechanical property matrices and state vectors are described with respect to the standard piezoelectric orthogonal axes system in which indices 1, 2, and 3 represent the x-, y-, and z-axes, while indices 4, 5, and 6 represent rotations around those axes. Rewriting Eq. 5.1 in stress-electric displacement form and simplifying taking into account that piezoelectric particulate composites are transversely isotropic along the poling (3-axis) direction [117].

$$\begin{bmatrix} \hat{T}_{11} \\ \hat{T}_{22} \\ \hat{T}_{33} \\ \hat{T}_{23} \\ \hat{T}_{31} \\ \hat{T}_{12} \\ \hat{D}_{1} \\ \hat{D}_{2} \\ \hat{D}_{3} \end{bmatrix} = \begin{bmatrix} \tilde{C}_{11} & \tilde{C}_{12} & \tilde{C}_{13} & 0 & 0 & 0 & 0 & 0 & -\tilde{e}_{31} \\ \tilde{C}_{12} & \tilde{C}_{22} & \tilde{C}_{23} & 0 & 0 & 0 & 0 & 0 & -\tilde{e}_{31} \\ \tilde{C}_{13} & \tilde{C}_{23} & \tilde{C}_{33} & 0 & 0 & 0 & 0 & 0 & -\tilde{e}_{33} \\ 0 & 0 & 0 & \tilde{C}_{44} & 0 & 0 & 0 & -\tilde{e}_{15} & 0 \\ 0 & 0 & 0 & 0 & \tilde{C}_{44} & 0 & -\tilde{e}_{15} & 0 & 0 \\ 0 & 0 & 0 & 0 & 0 & \tilde{C}_{66} & 0 & 0 & 0 \\ 0 & 0 & 0 & 0 & \tilde{e}_{15} & 0 & \tilde{\varepsilon}_{11} & 0 & 0 \\ 0 & 0 & 0 & \tilde{e}_{15} & 0 & 0 & 0 & \tilde{\varepsilon}_{11} & 0 \\ \tilde{e}_{31} & \tilde{e}_{31} & \tilde{e}_{33} & 0 & 0 & 0 & 0 & 0 & \tilde{\varepsilon}_{33} \end{bmatrix} \begin{bmatrix} \hat{S}_{11} \\ \hat{S}_{22} \\ \hat{S}_{33} \\ \hat{S}_{23} \\ \hat{S}_{31} \\ \hat{S}_{12} \\ \hat{E}_{1} \\ \hat{E}_{2} \\ \hat{E}_{3} \end{bmatrix} \tag{5.2}$$

where the '^' and '~' diacritical marks refer to the average material states and effective properties, respectively. The elasticity matrix elements, $\tilde{C}_{ij}$ [Pa], are equivalent to $\tilde{s}_{ij}^{-1}$, and the piezoelectric strain coupling matrix elements, $\tilde{e}_{ij}$ $[C/m^2]$, are defined via:

$$\tilde{e}_{ij} = \frac{\tilde{d}_{ij}}{\tilde{s}_{ij}} = \tilde{d}_{ij}\tilde{C}_{ij} \tag{5.3}$$

To investigate the energy density FOM_{15} of particulate composites as compared to the energy density FOM_{33}, the property set $\{\tilde{s}_{jj}, \tilde{\varepsilon}_{ii}, \tilde{d}_{ij}\}$ is analyzed for both shear and longitudinal mode activation as a function of the particle volume fraction (φ [-]).

5.2.2. ANALYTICAL MODELS

To predict the electromechanical behavior of piezoelectric particulate composites, three analytical methods are selected: the Hashin-Shtrikman (H-S) [118] elastic moduli bounds, the simplified piezoelectric property prediction model of Furukawa *et al.* [119] and an elaboration of Furukawa's model devised by Yamada *et al.* [34].

The H-S bounds give the minimal/maximal theoretical moduli of two phase composites with randomly dispersed spherical inclusions [118, 120]. The H-S lower and upper bounds are given in terms of the bulk ($\tilde{\kappa}^{+/-}$ [Pa]) moduli, shear ($\tilde{C}_{55}^{+/-}$) moduli and the longitudinal compliance ($\tilde{s}_{33}^{+/-}$) computed by considering the composite as a homogeneous isotropic linear elastic material. The 'm' and 'p' superscripts denote the matrix and particle phase, respectively.

$$\tilde{s}_{33}^{+/-} = \frac{3\tilde{\kappa}^{+/-} + \tilde{C}_{55}^{+/-}}{9\tilde{\kappa}^{+/-}\tilde{C}_{55}^{+/-}} \tag{5.4}$$

The Furukawa model presents simplified analytical expressions for the electromechanical properties of a piezoelectric particulate composite [119]. The model considers the composite as a uniform distribution of isolated spherical isotropic particles in an isotropic continuous polymer matrix, neglecting particle-particle and matrix-particle interactions. Due to the assumed incompressibility of both phases, the relation holds for both the effective longitudinal ($\tilde{C}_{33} = \tilde{s}_{33}^{-1}$) and the shear ($\tilde{C}_{55} = \tilde{s}_{55}^{-1}$) stiffness. The simplifying assumptions leading to Furukawa's closed-form equations only hold for dilute systems as demonstrated by experiment in the literature [113, 119, 121].

$$\tilde{\varepsilon}_{ii} = \frac{2\varepsilon_{ii}^{m} + \varepsilon_{ii}^{p} - 2\varphi(\varepsilon_{ii}^{m} - \varepsilon_{ii}^{p})}{2\varepsilon_{ii}^{m} + \varepsilon_{ii}^{p} + \varphi(\varepsilon_{ii}^{m} - \varepsilon_{ii}^{p})}\varepsilon_{ii}^{m} \tag{5.5}$$

$$\tilde{C}_{jj} = \tilde{s}_{jj}^{-1} = \frac{3C_{jj}^{m} + 2C_{jj}^{p} - 3\varphi(C_{jj}^{m} - C_{jj}^{p})}{3C_{jj}^{m} + 2C_{jj}^{p} + 2\varphi(C_{jj}^{m} - C_{jj}^{p})}C_{jj}^{m} \tag{5.6}$$

$$\tilde{d}_{ij} = \varphi\frac{15C_{jj}^{p}e_{ii}^{m}}{(3C_{jj}^{m} + 2C_{jj}^{p} - 3\varphi\left(C_{jj}^{m} - C_{jj}^{p}\right))(2\varepsilon_{ii}^{m} + \varepsilon_{ii}^{p} + \varphi\left(\varepsilon_{ii}^{m} - \varepsilon_{ii}^{p}\right))}d_{ij}^{p} \tag{5.7}$$

Yamada *et al.* extended Furukawa's model by taking the geometry of the (ellipsoidal) particles in the polymer matrix into account, via a shape fitting factor n [-] [34].

$$\tilde{\varepsilon}_{ii} = (1 + \frac{n\varphi\left(\varepsilon_{ii}^{p} - \varepsilon_{ii}^{m}\right)}{n\varepsilon_{ii}^{m} + (1-\varphi)\left(\varepsilon_{ii}^{p} - \varepsilon_{ii}^{m}\right)})\varepsilon_{ii}^{m} \tag{5.8}$$

$$\tilde{C}_{jj} = \tilde{s}_{jj}^{-1} = (1 + \frac{\varphi\left(C_{jj}^{p} - C_{jj}^{m}\right)}{C_{jj}^{m} + \frac{1}{3}\frac{(1+\nu)}{(1-\nu)}(1-\varphi)\left(C_{jj}^{p} - C_{jj}^{m}\right)})C_{jj}^{m} \tag{5.9}$$

$$\tilde{d}_{ij} = \alpha\varphi \frac{n\,\tilde{\varepsilon}_{ii}}{n\,\tilde{\varepsilon}_{ii} + (\varepsilon^{p}_{ii} - \tilde{\varepsilon}_{ii})} d^{p}_{ij} \tag{5.10}$$

where ν [-] is the matrix material's Poisson ratio and α [-] is a measure of the poling efficiency of the piezoelectric composite material, assumed equal to be 1 in this study. The fitting factor n is related to the ellipsoidal particle's aspect ratio AR [-] (= a/b, see Fig. 5.1) by an integral equation.

$$n = \frac{2}{AR}\left[\int_0^{\infty} \frac{du}{(AR^2+u)\sqrt{(AR^2+u)(1+u)^2}}\right]^{-1} \tag{5.11}$$

Several experimental studies have indicated close agreement between the measured electromechanical properties of piezoelectric particulate composites and Yamada's model [34, 112, 113, 122]. However, the corresponding fitted n values could not always be related to the physical morphology of the PZT particles used in the experimental analysis. At an increased particle volume fraction, agglomeration of the particles may cause the effective shape of the piezoelectric constituents to change. Hence, the assumption of a constant n value at changing particle volume fraction may not be physically accurate. It should also be noted that the simplified analytical models of Yamada and Furukawa do not stipulate whether the derived expressions for the piezoelectric constant $\tilde{d}_{ij}$ are valid for the unexplored operation mode $\tilde{d}_{15}$ [34, 113, 119].

5.3. FINITE ELEMENT MODEL

To gain a more accurate insight into the piezoelectric particulate composite's shear mode behavior, a more complex micromechanical theoretical model with less strict *a priori* assumptions at the expense of higher modelling complexity was developed. Taking a representative volume element (RVE) as the smallest representative periodical structure of the composite and applying appropriate periodic boundary conditions and loads to the RVE, one can predict the effective homogenized electromechanical properties of the piezoelectric composite by using a multi-physics finite element (FE) analysis [123, 124].

The prime advantage of this technique over (semi-)analytical models is the wide range of flexibility it offers in terms of particle shape, size, material, and orientation [117, 125, 126]. Instead of assuming homogeneous average strains and stresses acting on the particles, imposed in, for instance, the semi-analytical Dunn and Taya [121] expanded Mori-Tanaka (MT) frameworks [127], the numerical FE-RVE technique returns a physically more accurate solution by taking into account stress and strain variation within the particle, matrix and particle-matrix interface [117, 125, 128]. The FE-RVE method enables the simulation of these local stress and strain variations at a relatively high resolution such that the real electromechanical behavior of the particle in a non-active matrix can be compared for different activation modes.

5.3.1. MODEL DESCRIPTION

The new FE-RVE model developed for a random (0-3) piezoelectric particulate composite system is based on the following assumptions:

1. Both the particles and matrix behave as linear elastic homogeneous materials. Although the epoxy matrix typically exhibits a non-linear stress-strain curve at high strain levels at typical energy harvesting operational temperatures, the linear elasticity assumption is valid as the composite is, for the experimental measurements as well as for energy harvesting operations in general, loaded in its linear elastic regime [129, 130].

2. There is perfect bonding at the interface between the particles and the matrix. Hence, additional secondary interfacial effects and bond damages are not taken into account.

3. The randomly dispersed particles are assumed to be structured periodically at equi-distant locations within the matrix. Several studies have shown the effect of this assumption to be negligible as long as simulations are performed within the elastic regime [124, 126, 131, 132].

4. A two-dimensional FE analysis is performed to constrain the required computational power analogously to the numerical effective property study of Chambion *et al.* [126]. There are no reasons to conclude that a full computational expensive three-dimensional analysis would lead to different results for the ranking of the effectiveness of the composites and loading conditions considered here.

The RVE is assumed to be the smallest representative microstructure periodically extendable to retrieve the particulate composite's macroscopic electromechanical behavior. A generic representation of the resulting two-dimensional square RVE with a central ellipsoidal particle (spherical if $a = b$) and opposite boundary pairs {A+/A-} and {C+/C-} is shown in Fig. 5.1. The particle volume fraction v_f is varied by adapting the dimensions of the particle in a fixed dimension RVE ($z_{RVE} = 0.01$ mm).

$$v_f = \frac{ab\pi}{z_{RVE}^2} \tag{5.12}$$

5.3.2. BOUNDARY CONDITIONS

To ensure periodicity in terms of stress and deformation, appropriate periodic boundary conditions are applied at the two sets of opposite boundary pairs [123, 132]. The set of periodic boundary displacement (u_i) and electric potential (φ_e [V]) conditions for each boundary pair are formulated as follows, and where Y^+ and Y^- denote the positive and negative $x_{j/i}$ direction along each boundary pair, respectively.
[117, 124, 133]:

$$u_i^{Y^+} - u_i^{Y^-} = \hat{S}_{ij}(x_j^{Y^+} - x_j^{Y^-}) \tag{5.13}$$

$$\varphi_e^{Y^+} - \varphi_e^{Y^-} = \hat{E}_i(x_i^{Y^+} - x_i^{Y^-}) \tag{5.14}$$

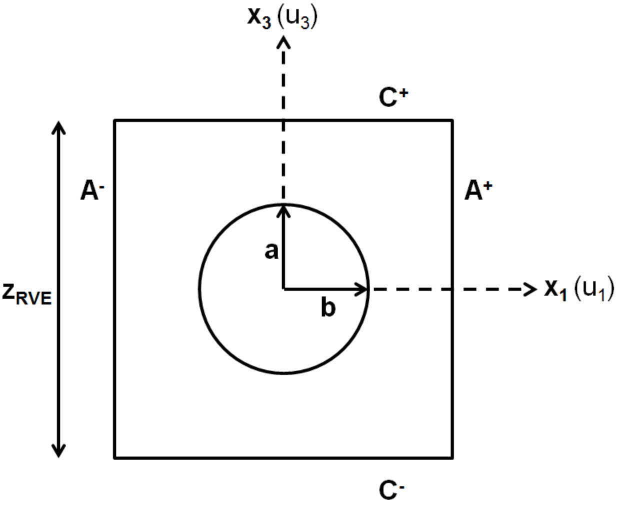

Figure 5.1: Generic representation of the two-dimensional square RVE sized by z_{RVE} with ellipsoidal inclusion defined by a and b.

Table 5.1: The load and periodic boundary conditions applied to simulate the effective longitudinal and shear mode electromechanical properties of the piezoelectric particulate composite. Periodic conditions are denoted by the '-' symbol, u_1 and u_3 refer to the displacement according to the x_1- and x_3-axis (see Fig. 5.1), respectively. S_3^0, S_5^0, S_1^0 are arbitrary strain constants equal to 0.1 in this study, and φ_e^0 is an arbitrary electric potential constant set to 1 V.

Case #	Property	BC def.	A$^-$	A$^+$	C$^-$	C$^+$
1	$\tilde{\varepsilon}_{33} = \frac{\hat{D}_3}{\hat{E}_3}$	$\varphi_e = \ldots$	-	-	0	φ_e^0
	$\tilde{e}_{33} = -\frac{\hat{T}_3}{\hat{E}_3}$	$u_1 = \ldots$	0	0	-	-
		$u_3 = \ldots$	-	-	0	0
2	$\tilde{s}_{33} = \frac{\hat{S}_3}{\hat{T}_3}$	$\varphi_e = \ldots$	-	-	0	0
		$u_1 = \ldots$	0	0	-	-
		$u_3 = \ldots$	-	-	0	$S_3^0 \cdot z_{RVE}$
3	$\tilde{\varepsilon}_{11} = \frac{\hat{D}_1}{\hat{E}_1}$	$\varphi_e = \ldots$	0	φ_e^0	-	-
	$\tilde{e}_{15} = -\frac{\hat{T}_5}{\hat{E}_1}$	$u_1 = \ldots$	-	-	0	0
		$u_3 = \ldots$	0	0	-	-
4	$\tilde{s}_{55} = \frac{\hat{S}_5}{\hat{T}_5}$	$\varphi_e = \ldots$	0	0	-	-
		$u_1 = \ldots$	-	-	0	$S_5^0 \cdot x_1$
		$u_3 = \ldots$	0	$S_5^0 \cdot x_3$	-	-

Four load cases have been applied (Table 5.1) to compute the effective electromechanical properties by FE analysis on the RVE [117, 134, 135]. Each load case corresponds to a set of load boundary conditions, and enables the simulation of one or more of the shear and longitudinal mode properties. The effective property of interest can be derived from the resulting RVE by implying that all but one element in the strain or electric field vector of Eq. 5.2 is equal to zero. The RVE states are computed based on the surface averaged values, as formulated for the strain state, by example:

$$\hat{S}_{ij} = \frac{1}{z_{RVE}^2}\int_A S_{ij}\, dA. \tag{5.15}$$

The stress, electric field, and electric displacement states are analogously determined.

5.3.3. CALCULATION METHOD

A two-dimensional FE-RVE analysis was performed with the commercial COMSOL Multiphysics software. The quasi-static response was calculated in the Piezoelectric Devices module according to the boundary conditions summarized in Section 5.1. Due to the various investigated particle volume fractions and geometries, an adaptable physics-controlled, normal-sized triangular element mesh was applied as illustrated for case 4, in Fig. 5.2. Each node was characterized with three degrees of freedom: two displacements (u_1 and u_3) and one electric potential (φ_e). The typical number of elements per simulated RVE was 880, with the elements devoted to the piezoelectric particle ranging from 15% (for the lowest volume fraction $\varphi = 0.007$) to 41% (for the highest volume fraction $\varphi = 0.40$). Both the passive (zero piezoelectric coupling matrix) polymeric and active ceramic phases were implemented as piezoelectric materials by strain-charge formulated constitutive equations. The piezoelectric phase was assumed to be poled along the RVE's x_3-axis.

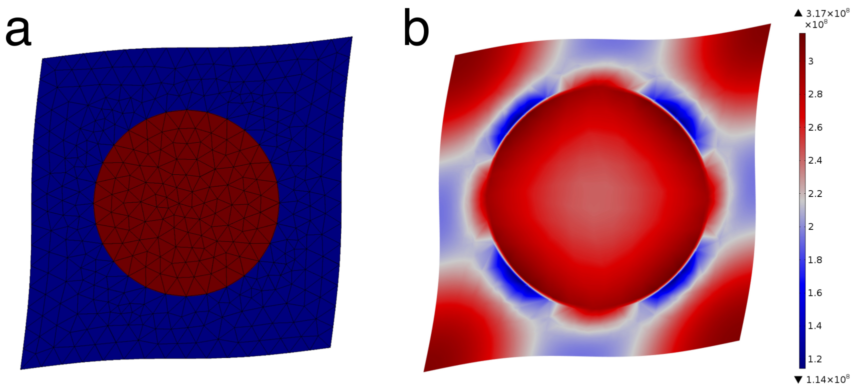

Figure 5.2: Example of the simulated RVE in COMSOL Multiphysics software. (a) Mesh view of the boundary conditions formulated for the $\tilde{s}_{55}$ effective property study (case 4 of Table 5.1), $\varphi = 0.28$ and $AR = 1$. (b) Shear stress (T_5) surface plot with identical conditions to (a).

5.3.4. MATERIAL DATA

The material properties of the epoxy and PZT are summarized in Table 5.2. Epoxy compliances were derived from the Young's modulus and Poisson ratio, assuming the epoxy to be a homogeneous isotropic linear elastic material. The dielectric constant of the epoxy matrix was derived from the measured capacitance. The transversely isotropic properties of the PZT were obtained from the supplier [60].

Table 5.2: Electromechanical property inputs of PZT5A4 [60] and epoxy [136, 137].

	s_{11}	s_{22}	s_{33}	s_{12}	s_{13}	s_{23}	s_{44}	s_{55}
	[m^2/N ·10^{-12}]	[m^2/N ·10^{-12}]	[m^2/N ·10^{-12}]	[m^2/N ·10^{-12}]	[m^2/N ·10^{-12}]	[m^2/N ·10^{-12}]	[m^2/N ·10^{-12}]	[m^2/N ·10^{-12}]
PZT5A4	16.0	16.0	18.0	-5.7	-7.2	-7.2	47.5	47.5
epoxy	588.2	588.2	588.2	-196.0	-196.0	-196.0	1529.4	1529.4

	s_{66}	ε_{11}	ε_{22}	ε_{33}	d_{33}	d_{31}	d_{15}
	[m^2/N ·10^{-12}]	[-]	[-]	[-]	[pC/N]	[pC/N]	[pC/N]
PZT5A4	44.3	1650.0	1650.0	1850.0	460.0	195.0	550.0
epoxy	1529.4	5.3	5.3	5.3	0	0	0

5.4. EXPERIMENTAL PROCEDURE

5.4.1. COMPOSITE PREPARATION

COMPOSITE samples consisting of quasi-equiaxed PZT particles in a conventional Epotek epoxy 302-3M (Epoxy Technology Inc., Billerica (MA), USA) were prepared with particle volume fractions ranging from 0 to 0.3 PZT. The PZT particulate powder (PZT-5A4, Morgan Electroceramics, Ruabon, UK) is identical to the powder used in Chapter 4). It was calcined at 1150 °C for 1 hour and dry milled for 2 hours with 5 mm Y-stabilized ZrO balls. The powder was then sieved, dried for 12 hours at 150 °C, and stored under vacuum conditions at room temperature. The particle size distribution of d10 = 1.0 μm, d50 = 1.9 μm and d90 = 4.2 μm was measured in an aqueous solution by laser diffraction with a Beckman Coulter LS230. The PZT particles were mixed with diglycidyl ether of bisphenol-A (DGEBA) resin for 5 minutes at 2500 rpm in a DAC 150 FVZ Speed-Mixer (Hauschild, Hamm, Germany). Then the multi-functional aliphatic amine hardener poly(oxypropyl)-diamine (POPD) was added to the PZT-resin mixture and mixed again for 5 minutes at 2500 rpm. The uncured composite was degassed in vacuum for 10 minutes and then poured into a Teflon mould. The composite samples were cured at 50 °C overnight in the closed mould, clamped between two steel plates. After cooling to room temperature, the disk-shaped composites were pre-cured for 15 minutes at 100 °C and punched to produce annular rings (d_{out} = 14 mm, d_{in} = 10 mm, t = 1.5 mm) for d_{15} measurements, and solid disks (d_{in} = 9 mm, t = 1.5 mm) as d_{33} references. All samples were manually polished to remove the outer epoxy-rich layer and smoothen any surface defect incurred due to punching. The samples were then post cured at 100 °C for 1 hour. Gold electrodes (t = 30 nm) were sputtered on either side of each sample using a Balzers Union SCD40 Sputter-coater (Balzers, Liechtenstein). Next, the samples were poled, in the thickness direction, in a rapeseed oil bath at 80 °C and 10 kV mm^{-1} for 1 hour with subsequent cooling to room temperature while the field was maintained. New measurement electrodes were sputtered as needed. All dielectric and piezoelectric measurements were performed at least 24 hours after poling in order not to be affected by charge accumulation at the particle-matrix interface.

5.4.2. MEASUREMENT METHODS

The relative dielectric constant, ε_r was derived from the capacitance, C [F], of the parallel plate electroded disks, measured at 1 kHz and 1 V with an Agilent 4263B LCR meter (Santa Clara, CA, USA). Quasi-static measurements with performed with a Berlincourt type piezometer (Piezotest, PM300, London, United Kingdom) to quantify the longitudinal and shear piezoelectric charge coefficient of at least 5 poled particulate composite samples per volume fraction. A dynamic excitation force equal to 0.25 N (at a frequency of 110 Hz) and a static 10 N sample grip force were imposed for all quasi-static d_{ij} measurements. The d_{33} was obtained from the parallel plate electrode, thickness-poled disks, while the d_{15} was obtained from the radially electroded, thickness-poled rings. Micrographs of the cross-section of the PZT-epoxy composites and particle morphology of the calcined PZT powder were recorded using a field-emission scanning electron microscope (SEM) (JEOL, JSM-7500F).

5.5. RESULTS AND DISCUSSION

IN this work PZT volumetric ranges from 0 to 0.4 were explored to avoid significant particle agglomeration/percolation effects which would violate the fundamental assumptions in the analytical and numerical models [34, 113, 119, 126].

5.5.1. COMPLIANCE

The simulated compliance $\tilde{s}_{33}$ and $\tilde{s}_{55}$ of the particulate composites as a function of the volume fraction φ, given in Vol% of PZT, are plotted in Fig. 5.3a and 5.3b, as predicted by the FE-RVE, the analytical models of Furukawa and Yamada (AR =1) as well as the H-S bounds. Both the numerical and analytical effective compliance follow the trend of the upper H-S compliance bound (H-S$_1$). This is to be expected as the H-S$_1$ bound takes the most compliant material (epoxy) as the matrix and the stiffest one (PZT) as the inclusion. Yamada *et al.* based their elastic model on the work of Hashin *et al.* causing the Yamada compliance trends to almost coincide with the H-S$_1$ bound [34]. The results of the numerical FE-RVE compliance simulations (both longitudinal and shear) are in agreement with the compliance properties predicted by the established analytical frameworks under the investigated particle volume fraction region.

5.5.2. DIELECTRIC CONSTANT

The relative dielectric constants $\tilde{\varepsilon}_{33}$ and $\tilde{\varepsilon}_{11}$ are plotted versus particle volume fraction in Fig. 5.4a and 5.4b, respectively. Note that the applied experimental methods did not allow to retrieve the $\tilde{\varepsilon}_{11}$. At an AR = 1 the analytical models overlap entirely, which is to be expected. The Yamada model, with a fitted AR = 1.1, shows a closer agreement to the experimental $\tilde{\varepsilon}_{33}$ data. The assumed spherical equi-axed morphology (AR = 1) of the primary particles is visually confirmed through SEM micrographs of the PZT par-

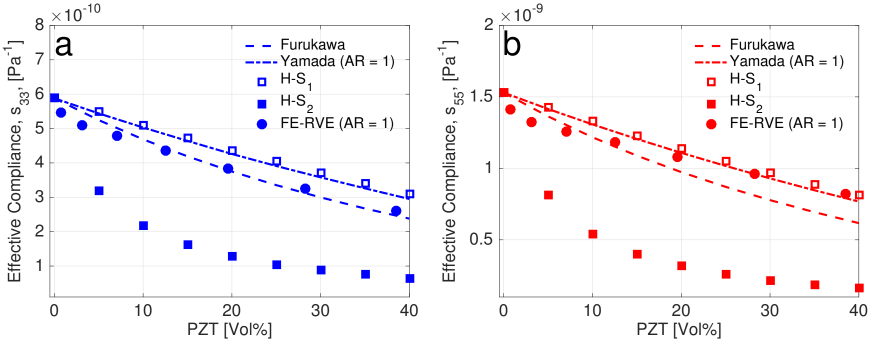

Figure 5.3: The effective compliance figures $\tilde{s}_{33}$ (a) and $\tilde{s}_{55}$ (b) plotted against φ as predicted by the FE-RVE, the analytical models of Furukawa, Yamada and the Hashin-Shtrikman (H-S) bounds.

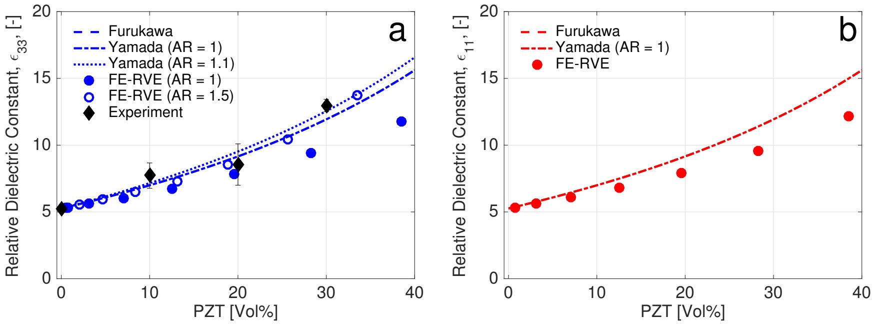

Figure 5.4: The effective dielectric constant figures ε_{33} (a) and ε_{11} (b) plotted against φ as predicted by the FE-RVE, the analytical models of Furukawa and Yamada and experimentally measured for ε_{33}.

ticulate powder (Fig. 5.5a). Yet, a small but growing discrepancy between the best fit for Yamada's model, at $AR = 1.1$, and Furukawa's model can be observed for increased particle volume fractions. The numerical FE-RVE model, with $AR = 1$, captures the non-linear $\tilde{\varepsilon}_{ii} - \varphi$ trend indicated by the experimental and analytical figures. However, it tends to underestimate the absolute value of the permittivity for higher volume fractions. SEM micrographs of the cross-sectional view of the composite microstructure, given in Fig. 5.5b to 5.5d, reveal the origin of the discrepancy. At $\varphi = 0.1$ the particles are truly randomly dispersed, in accordance with assumption (iii) for the RVE model. The occurrence of particle agglomeration at increased particle volume fraction changes the effective shape of the particles, contributing to the effective dielectric (and piezoelectric) properties of the composite. This causes the underestimation predicted by the analytical and numerical models with respect to the experimental data for higher volume fractions ($\varphi > 0.2$) subsequent to an initial good agreement for $\varphi = 0$ to $\varphi = 0.2$. The increasing underestimation of the predicted dielectric properties for increasing φ values was also reported in earlier experimental work on particulate PZT-polymer composites [113, 119].

A particle shape fitting strategy similar to the model of Yamada was applied for the FE-RVE simulations by changing the inclusion's aspect ratio. As shown in Fig. 5.4a, *AR* = 1.5 corresponds approximately to the experimental ε_{33} data. Clearly, the Yamada model and the FE-RVE simulations contradict each other in terms of the effective particle shape when fitted to the experimental data. Still, the FE-RVE is able to simulate the dielectric properties of the particulate composite as a function of the material properties and the degree of loading within acceptable bounds.

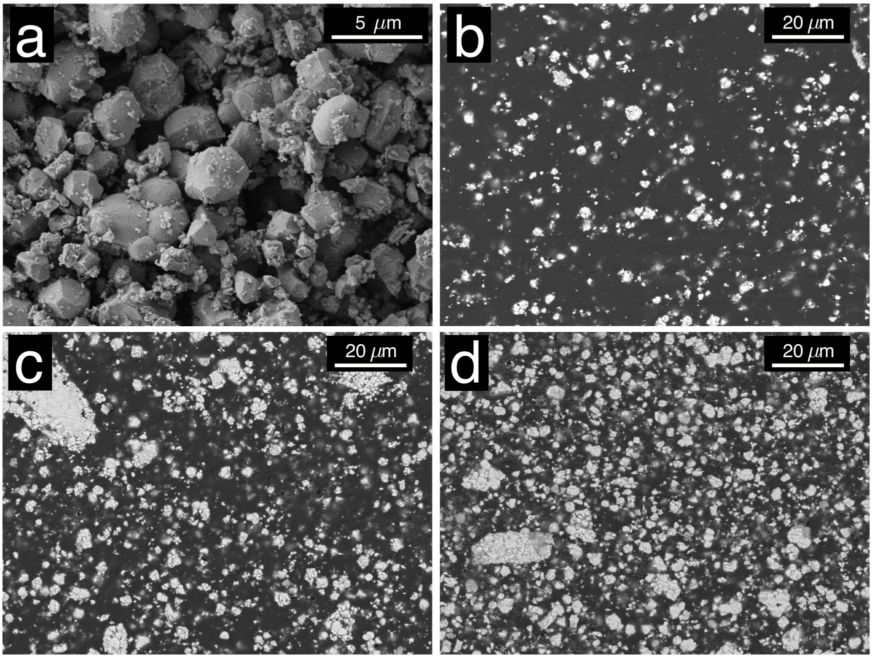

Figure 5.5: SEM micrographs of the particle morphology of the calcined PZT powder (a), and PZT-epoxy composites with PZT volume fraction, φ, of 0.1 (b), 0.2 (c) and 0.3 (d).

5.5.3. PIEZOELECTRIC CHARGE COEFFICIENT

All models (analytical and numerical) return underestimations of the experimental data for the longitudinal piezoelectric charge coefficient (Fig. 5.6a), assuming spherical particles (*AR* = 1). Again, particle agglomeration at increased PZT loading grades can be seen as the main rationale behind the increasing divergence between the experimental and theoretically predicted data. Making the particle aspect ratio a free variable in the longitudinal models in order to fit the experimental data over the entire volume fraction range, returns *AR* = 2.0 for the FE-RVE model and *AR* = 2.4 for the analytical one. The fitted FE-RVE aspect ratio value more or less coincides with the *AR* value based on the dielectric simulations (*AR* = 1.5), whereas application of the Yamada model would result in a relatively large inconsistency in particle aspect ratio for the dielectric (*AR* = 1.1) and piezoelectric (*AR* = 2.4) measurements.

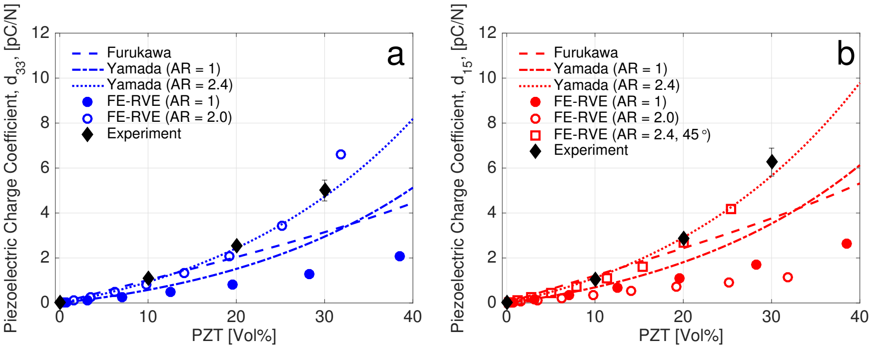

Figure 5.6: The effective piezoelectric charge coefficients d_{33} (a) and d_{15} (b) plotted against φ as predicted by the FE-RVE, the analytical models of Furukawa and Yamada and experimentally measured.

The shear piezoelectric charge coefficient (Fig. 5.6b) is also underestimated by the theoretically predicted values for $AR = 1$. The Yamada model exhibits close agreement with the experimental d_{15} data when the d_{33}-fitted particle aspect ratio is inputted, although the physical accuracy of this value is questionable. Other factors such as particle orientation, spacing and particle-matrix bond imperfections are known to play a non-insignificant role in the composite's effective piezoelectric behavior [111, 126, 138]. Still, taking into account the physical relevance limits, the results suggest that Yamada's model can be extended from the prediction of the common longitudinal piezoelectric charge coefficient to the shear charge coefficient.

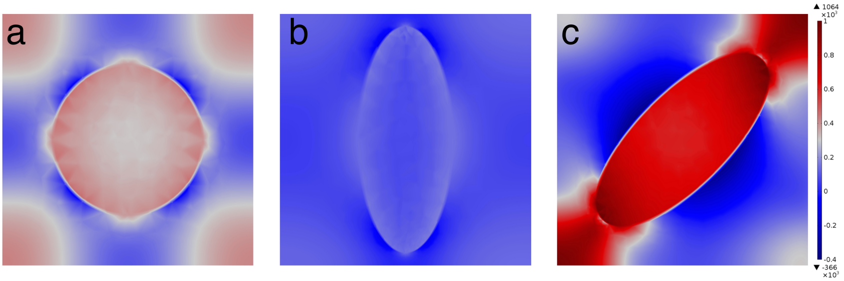

Figure 5.7: Shear stress (T_5) surface plot of a simulated RVE with boundary conditions formulated for the $\tilde{e}_{15}$ simulations (case 3 of Table 5.1) with a spherical inclusion (a), an ellipsoidal inclusion (b) and a 45° tilted ellipsoidal inclusion (c).

Applying the same strategy as in Yamada's model, fitting the $\tilde{d}_{15}$ FE-RVE simulations to the $\tilde{d}_{33}$-fitted aspect ratio ($AR = 2.0$), decreases the predicted value. Simply elongating the particle in the FE-RVE simulations results in a lower stress state for an ellipsoidal particle oriented along the x_3-axis (Fig. 5.7b) than for the spherical particle (5.7a) at equal electrical input energy of $\varphi_e^0 = 1$V (case 3 of 5.1).

The piezoelectrically induced shear stress can be increased by re-orienting the ellipsoidal particle along the RVE's diagonal with a 45° tilt (Fig. 5.7c). The tilt results in a close agreement with the experimental data for d_{15} and the d_{15}-fitted Yamada particle aspect ratio ($AR = 2.4$).

In conclusion, the FE-RVE and experimental results show that the d_{15} outperforms the d_{33} over the entire particle volume fraction range, while the ratios between the shear and longitudinal modes (d_{15}/d_{33}) converge to the anticipated PZT bulk material ratio (≈ 1.2) at $\varphi = 0.30$. The measurement accuracy of the Berlincourt meter is in the range of 1 pC/N, which results in relatively large error margins at the lowest volume fraction ($d_{15}/d_{33} \approx 1.0$). The anticipated bulk ratio of ≈ 1.2 therefore only becomes distinguishable when the absolute difference between d_{15} and d_{33} reaches 1 pC/N.

5.5.4. ENERGY HARVESTING FIGURE OF MERIT

Finally, the energy density FOM_{ij} in shear and longitudinal mode were calculated as a function of the PZT volume fraction. The results are plotted in Fig. 5.8. The results of the aspect ratio adjusted Yamada model and the elongated and tilted ellipsoidal particle FE-RVE simulations are in close agreement with the experimental data. Across all investigated volume fractions and for all three methods, the shear mode energy density figure of merit of the piezoelectric particulate composites is superior to the longitudinal activation mode. This is expected from the definition of the energy density FOM_{ij} figure ($FOM_{ij} = d_{ij}^2/\varepsilon_{ii}$) as, for a constant volume fraction, $\tilde{\varepsilon}_{11}$ only marginally increases with respect to $\tilde{\varepsilon}_{33}$ compared to the increase of $\tilde{d}_{15}$ to $\tilde{d}_{33}$.

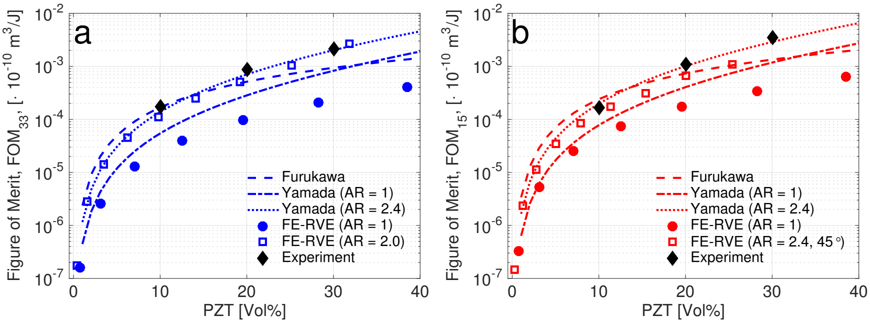

Figure 5.8: The effective energy density figures of merit in d_{33} mode (a) and d_{15} mode (b) plotted against φ as predicted by the FE-RVE, the analytical models of Furukawa and Yamada and experimentally measured.

In Fig. 5.9 the FOM_{ij} numerical results of $\varphi = 0.3$ PZT-epoxy composites from this study are compared to those of reference materials published in the literature [139–144], as a function of their simulated and reported material longitudinal stiffness. Only barium titanate (BT) and PZT ceramics favor the shear over the longitudinal activation mode. While PVDF-TrFE and BT exhibit relatively high FOM_{ij}'s, their low Curie temperatures inhibit their use in many energy harvesting applications. Activating the shear mode increases the FOM_{ij} of the particulate composite, even though the absolute value remains

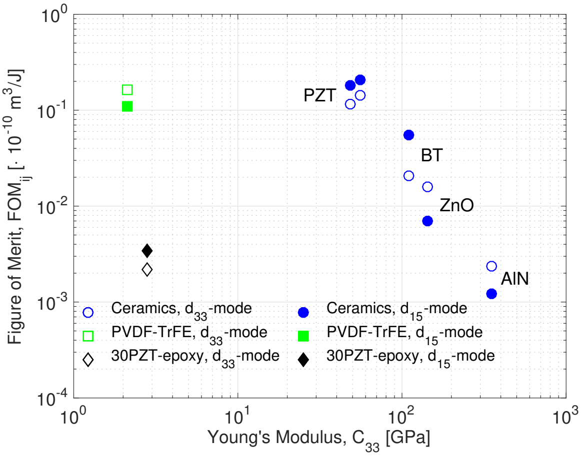

Figure 5.9: The d_{33} mode and d_{15} mode figures of merit versus the longitudinal stiffness of a piezoelectric composite with 30% volume fraction of PZT in epoxy (this work) compared to published reference materials [139–144].

low. The low to moderate volume fraction PZT-epoxy system investigated in this study was selected to allow an appropriate experimental validation and analytical verification of the developed RVE model, rather than for generation of high electromechanical coupling by an optimized piezoelectric particulate composite system. Higher *FOM*'s can be attained by simultaneously altering the filler material, the polymer matrix and the internal structure of piezoelectric particulate composites, while retaining a relatively low stiffness [57, 112].

5.6. CONCLUSIONS

THE developed FE-RVE model, established analytical models and experimental measurements have demonstrated the benefit of activating the shear d_{15} mode over the longitudinal d_{33} mode in piezoelectric particulate composites based on PZT. The FE-RVE simulations show close agreement with the experimental data and demonstrate that, next to particle morphology, particle orientation within the particulate composite is a contributing factor to the macroscopic shear mode behavior. While the absolute energy harvesting level of the composites loaded in shear remains relatively low, its performance is better than that of the same composite loaded in longitudinal tension or compression.

6

ANALYSIS AND EXPERIMENTAL VALIDATION OF THE FIGURE OF MERIT FOR PIEZOELECTRIC ENERGY HARVESTERS

When you light a candle,
you also cast a shadow.

Ursula K. Le Guin

Piezoelectric energy harvesters are at the front of scientific research as enabler of renewable, sustainable energy for autonomous wireless sensor networks. Crucial for this disruptive technology is the achievable output power. Here we show analytically that the maximum output energy per unit volume under impact excitation per pulse is equal to $1/(4-2k^2)\cdot 1/2 dgX^2$*, where* k^2 *is the electromechanical coupling constant,* d *and* g *are the piezoelectric charge and voltage coefficient, respectively, and* X *is the applied stress. The expression derived is validated by the experimentally measured output energy for a variety of piezoelectric materials over an unprecedented range of more than three orders of magnitude. As the prefactor* $1/(4-2k^2)$ *varies only between* $1/2$ *and* $1/4$ *the figure of merit for piezoelectric materials for energy harvesters is not* k^2*, as commonly accepted for vibrational harvesters, but* dg*. The figure of merit does not depend on the compliance, or Young's modulus. Hence we argue that commonly used brittle inorganic piezoelectric ceramics can be replaced by soft, mechanically flexible polymers and composite films, comprising inorganic piezoelectric materials embedded in a polymer matrix.*

6.1. INTRODUCTION

THE ability to deliver sustainable power to a wireless sensor network is attractive as it eliminates the time and cost of replacing batteries. This holds especially for networks that are either inhospitable or difficult to reach, such as structure-embedded microsystems and medical implants. The most attractive energy source is that of ambient mechanical vibrations, such as human motion, kitchen appliances and car engines. There are various methods to harvest the mechanical energy but, for small electronic harvesters, the most widely investigated effect is piezoelectricity [107, 145–150]. The direct effect is used, where application of a mechanical stress generates an output voltage. Below a volume of about 1 cm^3, the power density for piezoelectric transduction exceeds that for electromagnetic and electrostatic generators [41–43]. Estimations for the generated power range from 0.5 to 100 mW/cm^3 for vibrations with acceleration of 1 - 10 m/s^2 at 50 - 350 Hz [151, 152]. This means that with the ongoing decreasing power consumption of integrated circuits, autonomous microsystems come within reach [44].

As discussed in many review papers [8, 41–44, 71, 90, 109, 152, 153], piezoelectric energy harvesting comprises three major steps, *viz.* mechanical-mechanical energy conversion, mechanical-electrical energy transduction and electrical energy-electrical energy output transfer. The mechanical transformer converts the inertial or kinematic energy of the source into nontranslational energy in the piezoelectric material. Challenges are impedance matching and preventing mechanical failure under large stresses. Numerous mechanical designs are being used to optimize the strain, such as bimorph cantilevers, unimorph diaphragms, and cymbal transducers [154–159]. The maximum amount of energy is stored at resonance. The stored energy decreases rapidly away from the resonant frequency. Not surprisingly therefore, strategies are being pursued to increase the bandwidth of the harvester, such as tunable resonators and multi-frequency arrays [160–162].

The transduction between mechanical and electrical energy in the piezoelectric material is governed by the electromechanical coupling coefficient, k^2, which is the ratio between stored mechanical energy and input electrical energy, or vice versa. The value of k^2 is between 0 and 1. Most widely used are lead zirconium titanate ceramics (PZT) with k^2 of about 0.5 [12, 19].

The dynamically stimulated piezoelectric generators produce an AC current while a DC current output is needed to power electronics. To that end the AC current is rectified by diodes and stored in a capacitor or rechargeable battery [163]. Switches and inductors are used for current regulation as well as for current limiting and short-time energy storage, respectively [151, 164, 165]. The efficiency is about 50 %, limited by e.g. power consumption and mismatch between electrical output impedance of transducer and input impedance of the electrical circuit.

Research is focused on maximizing the strain in the mechanical conversion [154–159] and on maximizing the electromechanical coupling coefficient, k^2, of the piezoelectric transducer [166]. Optimization of k^2 is not surprising as it is represents the ratio between stored electrical energy and input mechanical energy. Therefore, most piezoelectric harvesters are based on PZT ceramics that exhibit a high value of k^2 of about 0.5. However, counter intuitively, energy harvesters have been reported that use piezoelectric materials with orders of magnitude lower values of k^2, *viz.* polyvinylidefluoride (PVDF) with $k^2 \approx 0.03$ [167, 168] and even ferroelectrets with $k^2 \approx 0.005$ [45, 46]. To solve this apparent discrepancy we analyzed the performance of a piezoelectric energy harvester. We will show that the figure of merit for the output energy is not k^2, but dg where d is the piezoelectric charge coefficient and g is the piezoelectric voltage coefficient.

To verify the figure of merit [169–172], we needed to measure the output of a harvester based on a variety of piezoelectric materials. We note, however, that the output energy strongly depends on the boundary conditions of the applied mechanical load. To circumvent the mechanical constraints, we therefore measured the output energy in the simple boundary condition of a clamped disk. This is, experimentally, the only way to reliably compare a variety of piezoelectric materials under identical conditions.

Unfortunately, due to the clamping, the output energy reduces to only nJ/cm^3. To overcome this limitation, we built an extremely sensitive piezometer system, which measures the output energy of a clamped disk under a well-defined sinusoidal mechanical impact. We measured a variety of material classes with widely varying piezoelectric and mechanical constants. For the first time, we could experimentally validate over many orders of magnitude that the figure of merit is not k^2 but dg. This has dramatic consequences for optimization of piezoelectric materials for energy harvesting. The figure of merit does not depend on the compliance. Hence, we have an additional degree of freedom to optimize the energy harvester. Instead of brittle ceramics, soft and mechanically flexible polymers and composite films, comprising inorganic piezoelectric materials embedded in a polymer matrix, can be applied.

This chapter is organized as follows. First, an analytical expression for the output energy of a piezoelectric harvester is derived. The figure of merit and the efficiency are discussed. Next, the piezometer system developed to measure with high sensitivity the output energy under impact excitation is presented. Then, we will present values for the stored electrical energy measured under impact excitation at open circuit. Measurements were performed on intermediate polarization states of a PZT piezoceramic, and on a wide variety of piezoelectric materials. Subsequently, the output energy is extracted using a resistive load. We will show that the experimentally measured output energy and open circuit stored energy as a function of piezoelectric constants and applied impact force can quantitatively be described, validating the analytically derived expressions.

6.2. FIGURE OF MERIT OF A PIEZOELECTRIC ENERGY HARVESTER

6.2.1. ELECTROMECHANICAL COUPLING COEFFICIENT, k^2

THE electrical displacement, D, of a piezoelectric capacitor under applied electric field, E, is the sum of the induced, P_i, and spontaneous polarization P_s:

$$D = P_i + P_s = \varepsilon_r \varepsilon_0 E + P_s \tag{6.1}$$

where ε_0 is the vacuum permittivity and ε_r is the relative dielectric constant. In the following we assume that the change in spontaneous polarization with electric field can be disregarded. Basically this means that the applied electric field is much smaller than the coercive field. The electrical energy stored in the capacitor per unit volume is then given by:

$$U_{elect} = \frac{1}{2}DE = \frac{1}{2}\varepsilon_r\varepsilon_0 E^2 \tag{6.2}$$

Application of the electric field induces a strain, x:

$$x = dE \tag{6.3}$$

where d is the piezoelectric charge coefficient. We note that the charge coefficient is a fourth rank tensor, commonly written with two indices following Voigt's notation, here for clarity ignored, as we only consider compressive stress in the poling direction, parallel to the surface normal. As there is no external stress, the mechanical energy stored per unit volume is then given by:

$$U_{mech} = \frac{1}{2}x^2/s = \frac{1}{2}(dE)^2/s \tag{6.4}$$

where s is the compliance. The electromechanical coupling coefficient, k^2, which is defined as:

$$k^2 = \frac{stored\ mechanical\ energy}{input\ electrical\ energy} = \frac{stored\ electrical\ energy}{input\ mechanical\ energy} \tag{6.5}$$

is then given by:

$$k^2 = d^2/\varepsilon_0\varepsilon_r s = dg/s = dgY \tag{6.6}$$

where Y is the Young's modulus, g is the piezoelectric voltage coefficient, given by $d/\varepsilon_0\varepsilon_r$, and $0 \leqq k^2 \leqq 1$.

6.2.2. MAXIMUM OUTPUT ENERGY AND TRANSMISSION COEFFICIENT OF A PIEZOELECTRIC HARVESTER

The piezoelectric capacitor acts as a transducer as it can convert mechanical energy in electrical energy and vice versa. The transducer harvest energy when connected to an electrical load, or generate a stress when connected to a mechanical load. The transmission coefficient, λ, is the ratio of output energy over input energy [173–175]. For a linear transducer:

$$\lambda = \frac{output\ mechanical\ energy}{input\ electrical\ energy}, \text{ or equivalently}$$
$$\lambda = \frac{output\ electrical\ energy}{input\ mechanical\ energy} \tag{6.7}$$

We calculate the transmission coefficient for the maximum mechanical work done by a piezoelectric transducer upon application of an electric field. To use a piezoelectric capacitor as a mechanical transducer we need a mechanical load. With zero mechanical load, or complete clamped conditions (*i.e.* no strain), no energy is sent to the outside world. We take the simplest case where a mass is put on the piezoelectric capacitor. The mechanical load yields a constant compressive stress, X, *i.e.* $X < 0$. The stress of the load induces a strain, x, of sX and an electrical displacement of dX. Although the convention is to use T for strain and S for stress, here we use x and X, respectively, to prevent confusion with other symbols, such as compliance, s. The load generates a mechanical input energy of $1/2xX$, which is $1/2sX^2$. In open circuit the total displacement is zero. An electric field is built up:

$$E = -d/\varepsilon_0\varepsilon_r X = -gX \tag{6.8}$$

leading to a stored electrical energy of:

$$U_{open} = 1/2\varepsilon_0\varepsilon_r E^2 = 1/2\varepsilon_0\varepsilon_r(-gX)^2 = 1/2dgX^2 \tag{6.9}$$

To generate an outside stress, the electrodes are connected and an electric field, E, is applied. This yields an additional strain of dE. The total strain is then given by:

$$x = sX + dE \tag{6.10}$$

and the mechanical output energy is given by:

$$U_{out} = 1/2xX = 1/2(sX + dE)X \tag{6.11}$$

Without external load, the stress, X, and the output energy are both zero. For a given compressive load, $X < 0$, the output energy depends on the value of the electric field. For small values, the strain due to the electric field is smaller than the strain induced by the load. The output energy then is positive, meaning that all energy remains stored in the transducer; no outside work is done. With increasing electric field, the strain due to the electric fields gets equal to the strain induced by the load. Then the total strain and output energy are both zero. At higher values of the electric field the total strain and output energy gets negative and work is done to the outside world.

For a given electric field, the maximum outside work is obtained when the derivative dU_{out}/dX is zero:

$$U_{out,max} = -1/8(dE)^2/s = -1/2sX^2 \text{when} X = -dE/2s \tag{6.12}$$

This means that the maximum output energy is obtained when the strain induced by the external load is half of the strain generated by the electric field, *i.e.* X/E is equal to $-d/2s$. Furthermore, the maximum output energy is exactly equal to the stored mechanical energy of the applied compressive load, *viz.* $1/2 \cdot sX^2$.

The corresponding input electrical energy follows from the displacement as:

$$U_{elect,in} = \frac{1}{2}DE = \frac{1}{2}(\varepsilon_r\varepsilon_0 E + dX)E = \frac{1}{2}(\varepsilon_r\varepsilon_0 E + d(-dE/2s))E \tag{6.13}$$

and the transmission coefficient, λ, for this maximum output energy is then:

$$\begin{aligned}\lambda_{max\ output} &= \frac{1}{8}(dE)^2/s \Big/ \frac{1}{2}\left(\varepsilon_r\varepsilon_0 E + d\left(-\frac{dE}{2s}\right)\right)E \\ &= \frac{1}{4}(d^2/s) \Big/ (\varepsilon_r\varepsilon_0 - \frac{d^2}{2s}) = k^2/(4-2k^2)\end{aligned} \tag{6.14}$$

where we have used $k^2 = dg/s$, *c.f.* Eq. 6.6. The limiting values for $\lambda_{max\ output}$ are $1/4k^2$ for small values of k^2 and $1/2k^2$ for k^2 approaching unity.

In summary, we apply a compressive load, X, on a piezoelectric capacitor. The load stores a mechanical input energy of $1/2sX^2$. This energy can be extracted by applying an electric field such that the strain induced is just twice the strain induced by the load. The transmission coefficient, the ratio between mechanical output energy and electrical input energy, is then equal to $k^2/(4-2k^2)$.

In literature, researchers have focused on the maximum transmission coefficient instead of on the coefficient for maximum output [173–175]. As derived in Appendix A, the maximum transmission coefficient is given by:

$$\lambda_{max} = (1/k + \sqrt{((1/k)^2-1))^{(}-2)} \approxeq k^2/(4-2k^2) \tag{6.15}$$

Only at low values of k^2 below about 0.5 the transmission coefficients are equal, *viz.* $k^2/(4-2k^2)$. At very high values of k^2, approaching 1, there is a significant difference. The transmission coefficient for maximum output energy, $\lambda_{max\ output}$, goes to $1/2k^2$ while the maximum transmission coefficient goes to unity. As explained in Appendix 6.A, the maximum transmission coefficient is obtained when the strain induced by the external load is almost equal to the strain generated by the electric field. However, this situation is practically useless as then the total strain and, hence the output power, both go to zero. A classical problem, the maximum transmission coefficient is unity but under that constraint you cannot harvest energy. As this situation is irrelevant, it is dealt with in the Appendix.

6.2.3. EFFICIENCY OF A PIEZOELECTRIC HARVESTER

The expression for the transmission coefficient is derived using the electrical input energy in the first work cycle. This energy however is not lost but remains stored as electrostatic energy in the capacitor, where it can be used in the next work cycle. Hence the efficiency of the transducer is almost 100% [174]. The only energy loss is the dielectric loss of the capacitor, which is typically below 3%. The transmission coefficient therefore is not a measure of efficiency; it represents the fraction of the stored mechanical energy that can externally be harvested, and vice versa.

Look at an energy harvester as consisting of a transducer coupled to an oscillating spring. When there is no damping to inelastic losses, all the mechanical energy remains stored in the spring. The transducer converts a fraction of the stored mechanical energy, *viz.* the transmission coefficient, into electrical energy. When the dielectric loss can be disregarded, the overall efficiency describing the conversion of absorbed, stored mechanical energy into electrical energy is unity.

6.2.4. FIGURE OF MERIT (FOM)

The mechanical energy stored in the harvester is equal to $1/2sX^2$, where s is the compliance of the piezoelectric material and X the compressive stress of the mechanical load. A fraction of $k^2/(4-2k^2)$ of the absorbed mechanical energy can be harvested. As a piezoelectric harvester must be driven dynamically, multiplication by the number of impacts per unit time then yields the maximum output power of the harvester.

The transmission coefficient to harvest the stored mechanical energy is $k^2/(4-2k^2)$. A few numbers for the limiting cases. We first take high performance PT or PZT with k of 0.7 and k^2 of 0.5. Then $\lambda_{max\ output}$ is 0.16. For PVDF and its random copolymers, with k^2 of about 0.03 we arrive at $\lambda_{max\ output}$ of 0.008. Finally, ferroelectrets, such as corona charged polypropylene, exhibit enormous piezoelectric voltage coefficients, g, up to 3 V m/N. However, the Young's modulus is only 1 MPa. Hence the value for k^2 is only 0.0045, and $\lambda_{max\ output}$ is 0.001, meaning that only 0.1 % of the stored mechanical energy can be converted.

Hence, at first sight, it seems that the performance is dominated by the transmission coefficient. However, not the transmission coefficient but the maximum output energy is the decisive parameter. The output energy of the harvester is given by:

$$U_{out,max} = \frac{1}{2}sX^2 \cdot \frac{k^2}{(4-2k^2)} = \frac{1}{(4-2k^2)} \cdot \frac{1}{2}dgX^2 = \frac{1}{(4-2k^2)}U_{open} \tag{6.16}$$

where Eq. 6.9 is used for the stored electrical energy in open circuit. Firstly, this equation implies that the maximum output energy is a fraction $1/(4-2k^2)$ of the stored electrical energy in open circuit. This fraction varies between 1/2 and 1/4 depending on k^2. Here we have assumed that all of the output energy can be electrically converted, meaning that the efficiency for the harvesting electronics is 100 %. In practice a value of 50 % is more realistic. Secondly, as the prefactor $1/(4-2k^2)$ hardly depends on the value of k^2, the figure of merit of a piezoelectric energy harvester is approximately equal to dg. The output energy is about $1/8-1/4$ times dgX^2. This figure of merit does not depend on the compliance. Hence, we have an additional degree of freedom to optimize the piezoelectric transduction in an energy harvester. Instead of brittle ceramics, soft and mechanically flexible materials with a small compliance can be used, such as piezoelectric polymers and composite films, comprising inorganic piezoelectric materials embedded in a polymer matrix.

The figure of merit can be understood by the following hand waving arguments. Firstly, when stress is applied to a piezoelectric transducer, the energy is used to charge the piezoelectric capacitor. The output energy is proportional to the stored electrical energy, $1/2dgX^2$, which therefore only depends on the piezoelectric voltage and charge coefficient. More specifically, the electrical output energy is the transmission coefficient times the input energy. The transmission coefficient is a fraction of k^2 and the mechanical input energy $1/2sX^2$. As k^2 is equal to dg/s, the output energy only depends on dg as the compliance is cancelled out. In the past, researchers have focused on increasing the electromechanical coupling coefficient, k^2. Piezoelectric polymers and flexible composites with very low k^2 values due to a large compliance, or small Young's modulus, therefore were considered inappropriate. However, the stored mechanical energy, $1/2sX^2$, is concomitantly huge and, consequently, the output energy does not depend on the compliance.

6.3. PIEZOMETER SYSTEM TO MEASURE THE STORED ELECTRICAL ENERGY

WE built a piezometer system to quantitatively relate the stored electrical energy with the piezoelectric charge and voltage coefficients, d and g, for any piezoelectric material. To eliminate the effect of sample geometry, a circular disk of a piezoelectric material is measured in clamped conditions. In this geometry there is no shear or bending. Due to the boundary conditions of a clamped disk there is hardly any strain, which means that there is hardly any stored electrical energy. Therefore the piezometer system is developed to be extremely sensitive, able to detect stored energy in the order of $\mathrm{nJ/cm^3}$. Here we present the working principle of the piezometer system, the force transfer, the temperature control, and the data extraction. A schematic representation of the piezometer system, operating under quasi-static load, is presented in Fig. 6.1a. A photograph of the jig is presented in Fig. 6.1b. An electrical diagram of the system is presented in Fig. 6.1c.

6.3.1. WORKING PRINCIPLE OF THE PIEZOMETER SYSTEM

The piezoelectric sample is placed between two rounded PM300 Piezometer (Piezotest, London, UK) calibers (bubble 1, in Fig. 6.1c). The sample is metallized on both sides, yielding a piezoelectric capacitor. An inductive voice coil (bubble 3, Fig. 6.1c), driven by a dynamic electrical signal from an Agilent 33210A function generator (Santa Clara, CA, USA), supplies the source of both static and dynamic force, $F(\omega t) = F_{max} f(\omega t)$, where $f(\omega t)$ is a periodic function (for example, $sin(\omega t)$), t is the time and ω the angular frequency. The polarization of the sample is in line with the direction of the force. The dynamic force generates piezoelectric charges on the surfaces of the piezoelectric sample, $Q(\omega t) = Q_{max} f(\omega t)$ [176].

To measure the short circuit current, $I_{SC}(\omega t)$, the charges $Q(\omega t)$ are lead to an ultra-low noise amplifier that virtually shorts the sample (zero volts over the sample) and converts the current from the sample into a voltage (trans impedance). The gain can be controlled over 4 decades: 1 MΩ, 10 MΩ, 100 MΩ, and 1 GΩ. The electrical bandwidth is limited with a 3rd order Bessel roll off (60 dB per decade) at 5 kHz. A Bessel function is used to get a constant phase delay over frequency, resulting in an overshoot free step electrical function response.

To measure the open circuit voltage, $V_{OC}(\omega t)$, the amplifier is bypassed by a measurement select switch (bubble 4, Fig. 6.1c). The charges, Q(ωt), are lead along a guarded cable to a Keithely 6517b Electrometer (Cleveland, OH, USA). The guard function of the electrometer is used to compensate for the capacitance of the coaxial connection between the device and the electrometer.

6.3.2. FORCE TRANSFER

The force of the voice coil is applied to the sample through a metal rod, isolated by a Macor mount, connected to one of the Berlincourt calibers (bubble 2, Fig. 6.1c). The Macor mount provides electrical and thermal isolation from the samples to the rod, while maintaining rigid transfer of the force to the sample. The offset voltage of the function generator supplies the static force to the sample. A voltage to current converter (amplifier) drives the voice coil up to + or - 20 N with 5 kHz electrical bandwidth. The overall transfer equals 2 N/V.

The applied force to the piezoelectric sample is accurately defined by the current through the voice coil, multiplied with the coil's force constant (in N/A). Under static conditions 100 % of the force from the voice coil is transferred to the surface of the sample. The force constant of the voice coil is non-linear when the coil is driven at large strokes. Therefore, to ensure the force is always defined within 5 %, the maximum sample thickness is limited to 7 mm (nominal 2 mm + 5 mm).

Under dynamic conditions any elasticity or backlash, between the voice coil and the contact of the mechanical tip of the rod to the sample, will lead to mechanical energy loss. Severe losses occur when the movement of the coil exceeds 10 μm movement at a frequency of 110 Hz. Due to elasticity and backlash, this excitation introduces a force loss of -0.74 N, as calculated from $F_{Loss} = -\omega^2 Am$, where A is the amplitude of the movement, and m is the moving mass of the voice coil, taken as 0.155 kg. The indentation of the mechanical tip of the rod, δ_{tip}, depends on the elasticity of the piezoelectric material being tested, according to: $\delta_{tip} = Ft/A_{caliber}Y$, where $A_{caliber}$ is the contact area of the caliber. Force loss is negligible when measuring rigid piezoceramics since the indentation at the maximum dynamic force of 10 N, is only 0.04 μm. In rubbery materials a 10 μm indentation already occurs at a dynamic force of 0.3 N. Therefore, the measurement frequency is limited to 10 Hz. The maximum force loss for the materials measured here, was -0.10 N for rubbery piezoelectric disks measured at 10 N dynamic force at 10 Hz. Furthermore, to dampen backlash the mount of the voice coil is designed to be extremely rigid.

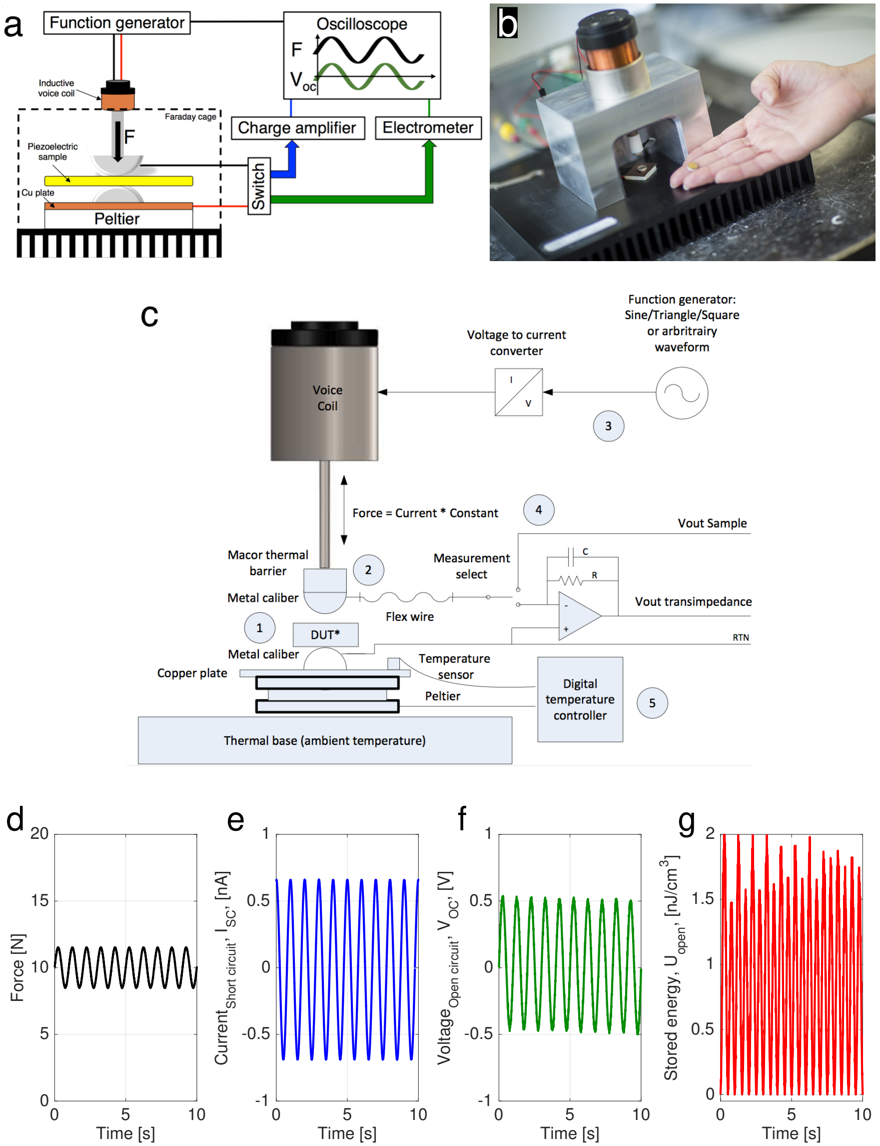

Figure 6.1: Developed piezometer system. (a) Schematic representation of the measurement system. (b) Picture of the jig. (c) Schematic diagram of the system, showing a simplified diagram of the peripheral electronics. (d) Example periodic input waveform of the applied force with a sinusoidal excitation of 1 Hz. (e) The short circuit current, I_{SC}, due the sinusoidal excitation shown in (d) of a PZ27 ceramic disk. (f) The corresponding open circuit voltage, V_{OC}. (g) The corresponding stored electrical energy, per unit volume, U_{open}.

6.3.3. TEMPERATURE CONTROL

To study the effect of temperature with force excitation, the device is equipped with a Peltier heating and cooling element, accurately controlled within 1 °C over a temperature range of -10 °C to +100 °C. The temperature is regulated by a MCPE1-07106NC-S Peltier actuated temperature controller, placed beneath a copper plate, sealed to the bottom caliber (bubble 5, Fig. 6.1c). The copper plate is used to create a uniform temperature distribution and mount a solid state temperature sensor. The bottom electrode stack can handle extreme forces without compression. To keep the temperature stable, the measured temperature is compared with the desired setpoint and the difference is amplified by a PID-controller that drives the Peltier element. The Peltier element is able to heat and cool with a $\Delta T/\Delta t$ of 20 K/s over a range of -10 °C to 100 °C.

6.3.4. DATA EXTRACTION

The periodic input waveform, generated by the function generator, and the piezoelectric output waveform, are collected with a DSOX2002A oscilloscope (Tektronix Inc.,Berkshire, UK). The maximum amplitude of both input and output waveforms is obtained in the frequency domain using the fast fourier transform function in MATLAB. Only the set frequency is used, and all other signals are disregarded. As an example we present measurements on a commercial, soft PZT, PZ27 ceramic disk. The diameter is 10 mm and the thickness, t, is around 1 mm. The force is shown in Fig. 6.1d and shows a dynamic sinusoidal force of 1.5 N at a frequency of 1 Hz, superimposed with a static force of 10 N.

The short circuit current, I_{SC}, is presented in Fig. 6.1e. The current is the derivative of the force, which for the sinusoidal excitation translates to an offset of almost 90 °. We note that the piezoelectric loss, $tan\,\delta_p$, can be calculated from the phase difference between applied force and output signal. The phase difference is not exactly 90 °, but typically 3 to 5 ° off, in the range of forces examined here. The calculated loss is small, and can be disregarded.

The short circuit current is used to confirm the accuracy of the set dynamic force. The piezoelectric charge coefficient, d_{33}, as calculated from $d_{33} = I_{SC}\frac{\Delta t}{\Delta F}$, perfectly matches the independently measured charge coefficient in the PM300 Piezometer, set to 110 Hz, 10 N static force and 0.25 N dynamic force.

The open circuit voltage, V_{OC}, is presented as a function of time in Fig. 6.1f. The voltage is the second derivative of the applied force, which for a sinusoidal excitation is equal to the original excitation waveform. It is crucial to note that the magnitude of the generated voltage is independent of the contact area, $A_{caliber}$, it only depends on the total surface area of the piezoelectric capacitor, A_{sample}.

$$D = dT = d\frac{F}{A_{caliber}} \tag{6.17}$$

Hence,

$$Q = DA_{caliber} = dF \tag{6.18}$$

Hence the total generated charge, Q, is independent of the area of the caliber.

We can now calculate the stored electrical energy, per unit volume of the piezoelectric capacitor, U_{open}, given as:

$$\begin{align} U_{open} &= \frac{1}{2} C V_{OC}^2 / A_{sample} t \tag{6.19} \\ &= \frac{1}{2} C \frac{(Q/C)^2}{A_{sample} t} = \frac{1}{2} C \frac{Q^2}{A_{sample} t} = \frac{1}{2\varepsilon_0 \varepsilon_r} \frac{t}{A_{sample}} d^2 F^2 / A_{sample} t \nonumber \\ &= \frac{1}{2} d g (F/A_{sample})^2 \tag{6.20} \end{align}$$

The energy per unit volume does not explicitly depend on the sample thickness. Furthermore, this energy depends on the surface area of the capacitor, but is independent of the contact area of the caliber. The reason is that the whole area of the capacitor is metallized, and due to the clamping there is no shear or bending, and therefore only d_{33} has to be considered. The scaling of the stored energy per unit area, U_{open}, with sample thickness and sample area will be experimentally validated in section 5.2 below.

The stored electrical energy, per unit volume, is presented as a function of time Fig. 6.1g, based on the V_{OC}, as shown in Fig. 6.1f. As U_{open} depends on V_{OC}^2, it oscillates at double the applied frequency. The energy density is relatively low, only in the range of nJ/cm^3. The first reason is that the sample is clamped. The second reason is that the sample area in this example is relatively large, a diameter of 1 cm.

We note that the small stored electrical energies can be accurately determined in the developed piezometer system because the applied force is accurately applied. Furthermore, we measure V_{OC}, in the range of mV to V, rather than the typical I_{SC}, in the pA to nA range. The focus on V_{OC}, especially allows for accurate measurement of materials, such as PVDF and composites, with low d_{33}, below 30 pC/N, but a relatively high g_{33}, up to 200 mV m/N. In summary, the developed piezometer system allows, for the first time, accurate measurement of the stored electrical energy for any piezoelectric material and sample configuration.

6.4. EXPERIMENTAL PROCEDURE

THE electric displacement, D, as function of electric field, E, was measured in a RT6000 HVA-2 High Voltage Tester (Radiant Technologies, Albuquerque, NM, USA). The piezoelectric charge coefficient, d_{33}, was measured with a Berlincourt type piezometer (PM300, Piezotest, London, UK). A static force of 10 N was used, under a 0.25 N peak to peak sinusoidal excitation at 110 Hz. The capacitance, C, and dielectric loss, $tan\ \delta_e$, at 1 kHz and 1 V were measured with an Agilent 4263B LCR meter (Santa Clara, CA, USA) and, preceding each frequency sweep of the impedance analyzer. The relative dielectric constant, ε_r, measured under zero stress, was derived from the capacitance.

The electromechanical coupling coefficient, k_p, and mechanical quality factor, Q_m, were determined by the IEEE resonance method using an Agilent HP4194A impedance analyzer (Santa Clara (CA), USA). The Q_m, is evaluated from the resonance peak in the frequency dependence of the real part of the impedance, Z', via $Q_m = f_{peak}/(f_1 - f_2)$, where f_1 and f_2 are the frequencies at which the impedance is equal to $Z'_{peak}/\sqrt{2}$, and f_{peak} is the frequency at the peak, Z'_{peak}. The k_p was evaluated from the following equation, where f_s and f_p are the series and parallel resonance frequencies [1].

$$k_p = \frac{\pi}{2}\frac{f_s}{f_p} tan\left(\frac{\pi}{2}\frac{\Delta f}{f_p}\right) \tag{6.21}$$

The stored electrical energy, U_{open}, was measured on a variety of piezoelectric samples in the developed piezometer system. The samples were driven at 23 °C with a sinusoidal excitation amplitude of 3 N peak to peak, at 10 Hz, and clamped at 10 N, unless mentioned otherwise.

First the ‘as-received’ (piezo-)electric properties of four sizes (thickness of 0.5 or 1.0 mm and diameter of 10 or 20 mm) of PZ27 piezoelectric ceramic disks were fully characterized, e.g., for remanent polarization, coercive field, and piezoelectric coefficients. 1-3 fiber composites, denoted by ‘A’, were obtained from Smart Materials GmbH (Dresden, Germany) with a thickness of 1.54 mm, a PZT (SP53) filler content of 48 vol.% in an epoxy matrix, and a fiber diameter of 800 μm. A 30 μm thick film of β-phase PVDF was obtained from Images SI Inc. (PZ-04, Staten Island, NY, USA), denoted by ‘B’. Three randomly distributed, 0-3, particle composites, denoted by ‘C’,’D’ and ‘E’, were prepared from solid state sintered ceramics embedded in a polymer matrix [68, 70, 177]. Composites ‘C’ and ‘D’ consist of 30 vol.% soft PZT-5A (Morgan Electroceramics, Ruabon, UK), in a Zn-doped ionomer (Surlyn 9320, DuPont, Barueri, SP Brazil) and an epoxy (302-3M Epotek, Epoxy Technology Inc., Billerica (MA), USA) matrix, respectively. Composite ‘E’ consists of 50 vol.% of Li, $K_{0.485}Na_{0.485}Li_{0.03}NbO_3$ (KNLN) embedded in a PDMS matrix. Two dielectrophoretially aligned, quasi 1-3, particle composites, denoted by ‘F’ and ‘G’, were prepared from solid state sintered ceramics, PZT-5A and KNLN, embedded in the same epoxy matrix [39, 64].

6.5. RESULTS AND DISCUSSION

6.5.1. INTERMEDIATE POLARIZATION STATES OF PIEZOCERAMIC PZ27

To validate dg as the figure of merit for energy harvesting, we used the intermediate, or unsaturated, polarization states of the piezoceramic PZ27 as a model system. We start from a thermally depolarized PZ27 disc, by annealing for 1 h at 500 °C. The residual d_{33} then is less than 5 pC/N. Subsequently, we measured the electrical displacement as a function of applied electric field. The maximum applied voltage is ramped in small steps from 200 V to 2000 V, corresponding to a maximum applied electric field of 4 kV/mm. The measured displacement as a function of applied electric field is presented in Fig. 6.2a. With increasing applied voltage the inner loops gradually open until at high bias the fully saturated hysteresis loop is obtained. The remanent polarization, *i.e.* the displacement at zero bias, is derived as 34.5 μC/cm^2 and the coercive field obtained is 1.7 kV/mm, both in perfect agreement with reported literature values. We note that retention measurements have shown that the intermediate polarization states are stable over time, up to the Curie temperature [178]. The remarkable stability originates from the coexistence of effectively independent domains, with slightly different values of the coercive field.

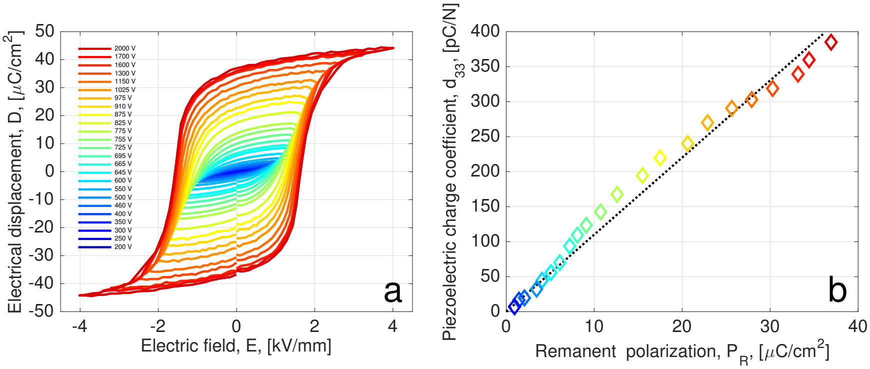

Figure 6.2: Piezoelectric charge coefficient of intermediate polarization states. (a) Hysteresis loops of a representative thermally de-poled PZ27 ceramic disk as a function of electric field, E. The applied maximum field is increased in small steps, indicated by the bias given in the legend. (b) Corresponding piezoelectric charge coefficient, d_{33}, as a function of the remanent polarization, P_R. The colors of the experimental points correspond to the applied poling voltages of Fig. 6.2a).

For each set value of the polarization state, we measured the piezoelectric charge coefficient. The values of d_{33} are presented as a function of the remanent polarization in Fig. 6.2b. A linear dependence is obtained, with a slope of 1.0 10^{-9} m^2/N. The order of magnitude can be explained as follows. The origin of intrinsic piezoelectricity is electrostriction, biased by the spontaneous polarization. The piezoelectric strain of a ferroelectric, single domain, single crystal, with a centrosymmetric paraelectric phase, can be obtained from expansion of the free energy in a Taylor series [179] with respect to the electric displacement which is taken as the fundamental variable [180]. As odd terms in the expansion vanish by symmetry [181], the strain as a function of electric field is given by [27]:

$$X_{33} = Q_{33}D^2 = Q_{33}(\varepsilon_r\varepsilon_0 E\acute{p} + P_s)^2 = 2Q_{33}\varepsilon_r\varepsilon_0 P_s E\acute{p} + Q_{33}P_s^2 + Q_{33}\varepsilon_r^2\varepsilon_0^2 E^2 \qquad (6.22)$$

where $\acute{p}$ is a parity function, with values of -1 or +1, to account for the relative orientation of electric field and spontaneous polarization, and where we have used that $\acute{p}^2$ equals unity. Q_{33} is the coefficient of electrostriction, a universal property of solid and liquid dielectrics [182, 183]. The first term on the right hand side of Eq. 6.22 corresponds to the piezoelectric effect, with the piezoelectric charge coefficient, d_{33} given by $2Q_{33}\varepsilon_r\varepsilon_0 P_s$. The piezoelectric effect can thus be understood as the electrostriction biased by the spontaneous polarization. The second term, $Q_{33}P_s^2$, describes the residual, spontaneous strain. The last term, $Q_{33}\varepsilon_r^2\varepsilon_0^2 E^2$, is referred to as the pure electrostrictive contribution. For ferroelectric materials this term is small and typically disregarded.

As shown in Appendix 6.B, the relative dielectric constant slowly increases with increasing remanent polarization. We take an average value of 1500. For Q_{33} we use the reported value of 0.02 $\mathrm{m}^4/\mathrm{N}^2$ [184]. The slope of Fig. 6.2b, $2Q_{33}\varepsilon_0\varepsilon_r$, then is calculated as 5 10^{-10} m^2/N, about half the extracted experimental value. Therefore, about half of the piezoelectric charge coefficient is intrinsic, due to electrostriction biased by the spontaneous polarization, and the other half is extrinsic due to *e.g.* domain wall motion.

6.5.2. SCALING OF THE STORED ELECTRICAL ENERGY

To validate the scaling of the stored energy per unit volume, U_{open}, with sample dimension, applied force and piezoelectric constants, *c.f.* Eq. 6.16, we first used piezoceramic PZ27 as a model system. As discussed in paragraph 6.5.1, the polarization is set by varying the maximum value of the applied AC voltage over the piezoelectric capacitor. For each set value, the piezoelectric charge coefficient, d_{33}, was measured and, by using the independently measured dielectric constant, the piezoelectric voltage coefficient, g_{33}, was calculated. In the developed piezometer system the open circuit output voltage was measured under sinusoidal excitation. The peak to peak value of the applied force and output voltage were obtained in the frequency domain by using a fast Fourier transform. Only the set frequency was used, and all other signals were disregarded. Four capacitors with different layer thickness and electrode area were used. The stored electrical energy was calculated from the open circuit output voltage, capacitance and sample dimensions, *c.f.* Eq. 6.19.

The stored electrical energy, per unit volume and per pulse, is presented on a double logarithmic scale as a function of $d_{33}g_{33}$ in Fig. 6.3a-d. Each figure corresponds to a different capacitor, and each point represents a different intermediate polarization state. Comparison of Fig. 6.3a with Fig. 6.3b, and of Fig. 6.3c with Fig. 6.3d, shows that the stored energy is independent of the thickness of the capacitors. Comparison of Fig. 6.3a with Fig. 6.3c, and of Fig. 6.3b with Fig. 6.3d, shows that the stored energy scales inversely with the electrode area. Furthermore, the dashed lines in Fig. 6.3a,d are calculated using $U_{open} = \frac{1}{2}dg(F/A_{sample})^2$, *c.f.* Eq. 6.9. Without any adjustable fit constants, for all capacitors and intermediate polarization states a perfect agreement is obtained.

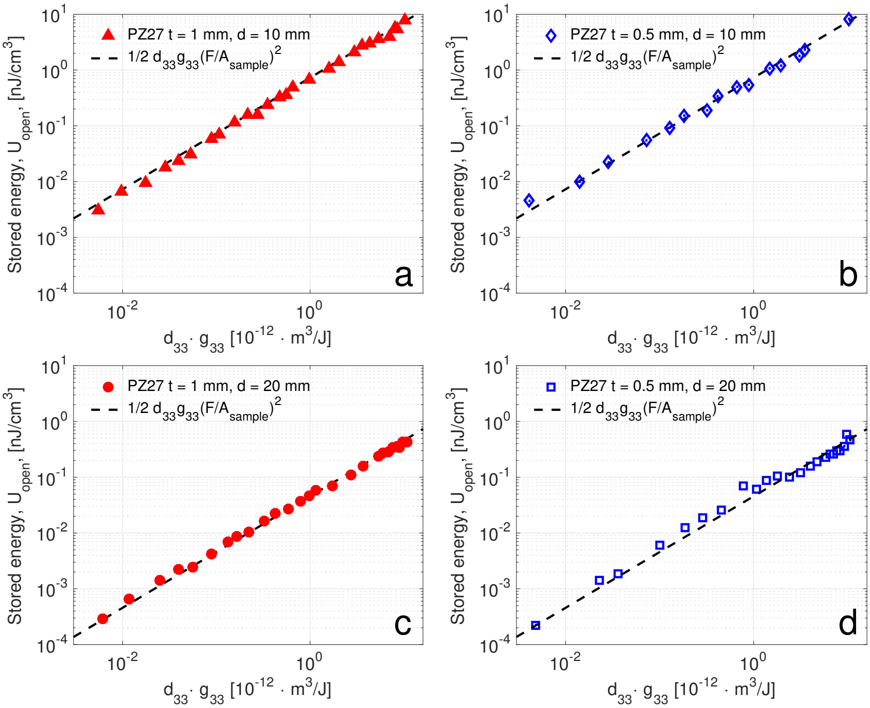

Figure 6.3: Stored electrical energy as relates to figure of merit. (a) Stored electrical energy generated per pulse, U_{open}, as a function of the intermediate figure of merit, $d_{33}g_{33}$, of a PZ27 ceramic disk, of 1 mm thickness and 10 mm diameter, due to a sinusoidal excitation, F, of 3 N peak to peak. The dashed line is the verification of the measured U_{open}, calculated using Eq. 6.9, or $\frac{1}{2}d_{33}g_{33}(F/A_{sample})^2$. (b) The corresponding U_{open} of a PZ27 disk of 0.5 mm thickness and 10 mm diameter. (c) The corresponding U_{open} of a PZ27 disk of 1 mm thickness and 20 mm diameter. (d) The corresponding U_{open} of a PZ27 disk of 0.5 mm thickness and 20 mm diameter.

To verify that the perfect agreement not only holds for PZ27, but is generic for any piezoelectric capacitor, we repeated the measurements using a wide variety of piezoelectric materials. We used bulk β-phase PVDF; random 0-3 composites consisting of KNLN in PDMS and PZT in an ionomer or epoxy matrix; a 1-3 composite comprising PZT in epoxy; and quasi 1-3 composites comprising dielectrophoretically aligned PZT or KNLN in an epoxy matrix. All capacitors, but the 30 μm thick PVDF film, had a similar thickness of 1 mm, and an electrode diameter of 10 mm. The open circuit output voltage was measured under sinusoidal force of 3 N peak to peak. The stored electrical energy per unit volume, per pulse, is presented as a function of the independently extracted values of $d_{33}g_{33}$ in Fig. 6.4a. The dashed line is calculated using Eq. 6.9. A perfect agreement is obtained, similar to the intermediate polarization states of PZ27.

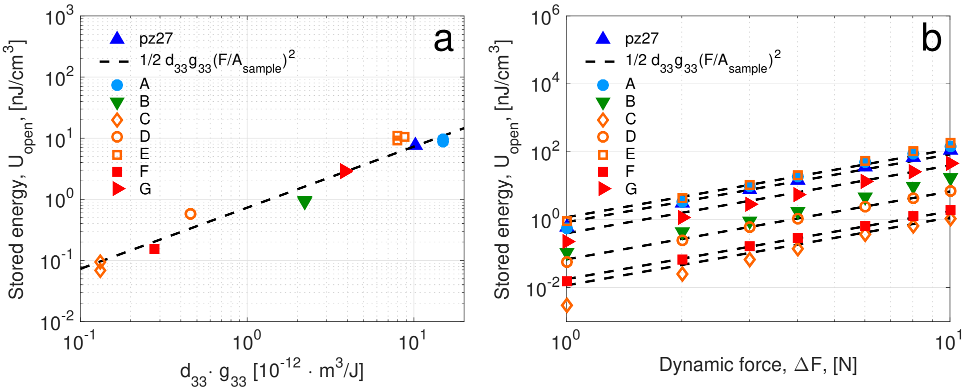

Figure 6.4: Figure of merit as relates to the stored electrical energy of a variety of piezoelectric material classes. (a) Stored electrical energy per volume, per pulse, as a function of the figure of merit ($d_{33}g_{33}$). The dashed line is the verification of U_{open}, calculated using Eq. 6.9, or $\frac{1}{2}d_{33}g_{33}(F/A_{sample})^2$, for a given sinusoidal force, ΔF, of 3 N peak to peak and sample area, A, of 78.5 mm^2, which corresponds to a diameter of 10 mm.
(b) Stored electrical energy per volume, per pulse, as a function of the peak to peak value of the applied sinusoidal force, ΔF. The dashed lines represent the calculation of $\frac{1}{2}d_{33}g_{33}(F/A_{sample})^2$ for each corresponding figure of merit, $d_{33}g_{33}$, and sample area, A.

As a final confirmation we deliberately varied the applied dynamic force between 1.0 N to 10 N peak to peak. The stored electrical energy is presented as a function of applied force on a double logarithmic scale in Fig. 6.4b. For each material investigated, the stored electrical energy increases with the applied force squared.

In summary, we experimentally validated that the stored electrical energy per unit volume, per pulse, is independent of the thickness of the capacitor. The energy scales with the inverse of the electrode area, which confirms that the stored energy does not depend on the area of the caliber, as long as it is smaller than the metallized electrode area. The stored energy is proportional to the applied force squared and to the product of the piezoelectric constants $d_{33}g_{33}$, which was varied over three orders of magnitude, from 10^{-2} pm^3/J to 10 pm^3/J. This implies that the expression derived for the stored energy per pulse, $U_{open} = \frac{1}{2}d_{33}g_{33}(F_{peak\ to\ peak}/A_{sample})^2$ holds for any piezoelectric material, irrespective of chemical composition or microstructure.

6.5.3. STORED ELECTRICAL ENERGY AND INPUT MECHANICAL ENERGY

In this work, the maximum stored electrical energy, per pulse, has consistently been in the order of nJ/cm^3. However, output powers of vibrational energy harvesters are commonly reported in the order of mW/cm^3. The discrepancy is due to the boundary conditions of the mechanical load, as will be discussed below.

We measured the stored electrical energy of different material classes in the simple boundary condition of a clamped disk. This is experimentally the only way to reliably compare a variety of piezoelectric materials under identical conditions. However, we note that this clamped condition is the least efficient at transferring the applied load into elastic strain energy. The calculated elastic strain energy of a clamped plate, of dimensions 1 x 1 x 0.1 cm, is shown in Fig. 6.5a as a function of applied force. At 10 N, only 5.95 nJ of elastic strain energy is induced. We derive an electromechanical coupling coefficient, k^2, of 0.36, by dividing the measured stored electrical energy over the calculated mechanical strain energy of the PZ27 disk. This value is in perfect agreement with the measured value, as shown in Appendix 6.B, and with reported values for PZT piezoceramics. Hence, we can conclude that the calculated strain energy in a clamped disk is a good approximation for the actual strain energy.

To increase the stored electrical energy of the piezoelectric material, the mechanical boundary conditions must be changed to induce more elastic strain energy per applied force. To this end we calculated the stored mechanical energy for a fixed volume of piezoelectric material, by varying only the shape and clamping conditions. For six different configurations, the strain energy as a function of applied force is presented in Fig. 6.5a. Details of the calculations can be found in Appendix 6.C.

In the first example, we changed the clamped plate into a simply supported plate of the

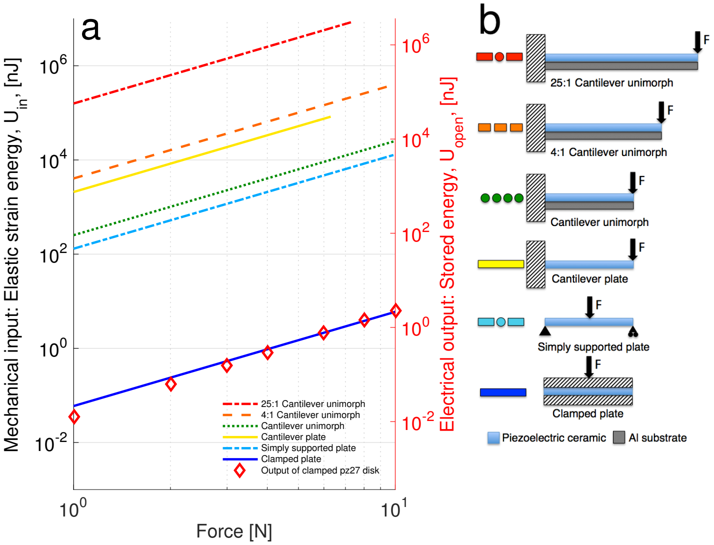

Figure 6.5: Calculated mechanical input energy and electrical output energy of 0.1 cm^3 volume of piezoelectric material, in six boundary conditions. (a) Elastic strain energy of common piezoelectric energy harvesting components. The open diamond markers represent the measured stored electrical energy of a clamped PZ27 disk, reproduced from Fig. 6.4. (b) Graphical representations of the boundary conditions of the analytically calculated piezoelectric plates. From bottom to top: a clamped plate, a simply supported plate, a cantilever plate, a cantilever unimorph, a 4:1 cantilever unimorph where the length of the plate is 4 times its width, and a 25:1 cantilever unimorph with length 25 times its width. The depictions of the cantilever unimorphs with altered geometric ratios are not to scale. The unimorph substrate is scaled such that the neutral axis of the stress is at the bottom of the piezoelectric layer.

same dimensions. As the plate can bend in the center, the strain energy immediately increases by three orders of magnitude, as shown by the dash-dotted light blue curve in Fig. 6.5a.

To get even more bending, we exchanged the simply supported plate by a cantilever plate. The strain energy is now even 4.5 orders of magnitude larger, as shown by the yellow, mid-range solid curve in Fig. 6.5a. The curve abruptly ends at 6.3 N of force, since applying higher forces exceeds the critical tensile stress, X_{crit}, of 34.2 MPa at which the expected probability of failure of this ceramic is 1 % [185]. Soft PZT ceramics can withstand higher compressive strain than tensile strain, so to ensure the full volume of the piezoelectric ceramic material is in compression, a unimorph configuration is used.

To calculate the strain energy of the unimorph, we take the same volume of piezoelectric material and assume it is perfectly bonded to an Al plate of equal width and length. To ensure that the piezoelectric plate is in compression, the thickness of the Al plate is chosen such that the neutral axis of the unimorph coincides with the interface between the piezoelectric plate and Al substrate. The unimorph configuration induces about an order of magnitude less strain energy than the cantilever plate, as can be seen from the dotted curve in Fig. 6.5a. However, although the stored energy is slightly less, the unimorph can withstand higher absolute strain.

Still more elastic strain energy can be induced in the same volume of piezoelectric material by changing the geometric ratio of the cantilever unimorph, *i.e.*, making it longer and less wide (shown by the top two curves in Fig. 6.5a). We note that the critical *compressive* strain, is reached at 7.4 N in the cantilever unimorph with a 25:1 geometric ratio. This type of component configuration more closely resembles the piezoelectric harversters used in literature. For example, at 1 N of applied force, the cantilever unimorph with a geometric ratio of 25:1 achieves 1.6 mJ/cm^3 of strain energy. Assuming the electromechanical coupling is unaffected by the change in boundary conditions from a clamped plate to a cantilever unimorph, the stored electrical energy is expected to be about 0.58 mJ/cm^3. When the piezoelectric component is actuated at 10 Hz, under the same measurement conditions used in this work, the stored electrical power would then be 5.8 mW/cm^3. We note that this order of magnitude perfectly fits the estimations for the generated power per unit volume [151, 152]. Furthermore, optimization of the strain development leads to a 10^6 fold increase in harvested energy density.

6.5.4. HARVESTED OUTPUT ENERGY

To support the analysis above, we measured not only the stored electrical energy, but also the harvested output energy. There are many methods to transfer stored electrical energy to the outside world, such as rectifying diode rings or inductive coils. Here we did not optimize the electrical-electrical conversion, but used a resistive load. The piezoelectric capacitor was excited with sinusoidal impact as described above. The output power was measured and plotted as a function of the resistive load. A parabola was obtained, with a maximum power point occurring when the impedance of the resistive load, $R_{load\ optimal}$, was equal to the impedance of the piezoelectric capacitor.

The ratio of output power over the stored electrical power in open circuit conditions, $U_{out,max}/U_{open}$, is presented in Fig. 6.6 as a function of the electromechanical coupling coefficient, k^2. The ratio $U_{out,max}/U_{open}$ was taken $(V_{max\ power\ point}/V_{open\ circuit})^2$ and values of k^2 were calculated from Eq. 6.6. The power ratio is about 0.12 at low values of k^2 and increases to about 0.45 at values of k^2 approaching unity. The solid line is calculated as $1/(4-2k^2)$, as derived from the analytical derivation of the maximum output energy in Section 6.2.4, *c.f.* Eq. 6.16. The deviation is a factor of two. The reason is that the calculated maximum output energy assumes 100 % efficiency for the conversion of output energy into the electrical energy of the circuit. For the resistive load used here we calculate that this transfer efficiency is about 50 %, see Appendix 6.D. Taking this factor into account, the dashed line is calculated, and a good agreement is obtained, validating that the output energy of an energy harvester per unit volume per pulse, $U_{out,max}$, is given as $1/(4-2k^2)\cdot 1/2dgX^2$, as analytically derived in Eq. 6.16.

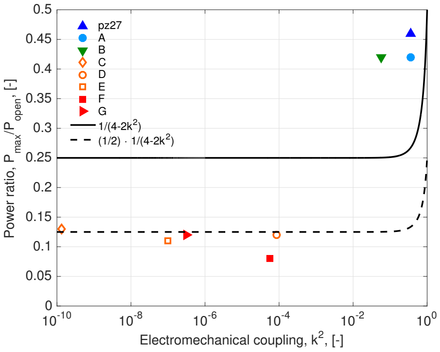

Figure 6.6: Maximum output energy over stored electrical energy in open circuit conditions as a function of electromechanical coupling coefficient, k^2. The solid line is calculated as $1/(4-2\cdot k^2)$, while the dashed line is calculated as $(1/2)\cdot 1/(4-2\cdot k^2)$.

6.6. CONCLUSIONS

We have analytically derived that for an energy harvester, comprising a piezoelectric capacitor with mechanical load, the maximum output energy per unit volume per impact pulse is given by $1/(4-2k^2)\cdot 1/2dgX^2$. A sensitive piezometer system was developed that with high accuracy could measure the output energy under sinusoidal impact excitation. The output energy was measured for intermediate polarization states of a PZT piezoceramic, and for a wide variety of ferroelectric materials. The experimentally measured output energy could perfectly be described, over more than three orders of magnitude. The prefactor $1/(4-2k^2)$ varies only between 1/4 and 1/2 meaning that the figure of merit of a piezoelectric energy harvester is not k^2, as until now generally accepted, but dg.

APPENDICES

6.A. MAXIMUM TRANSMISSION COEFFICIENT OF A PIEZOELECTRIC HARVESTER

THE harvester can be optimized to extract the maximum amount of stored energy, as analyzed above, but it can also be optimized to obtain the maximum transmission coefficient, λ_{max}. The transmission coefficient is the ratio between output work, *c.f.* Eq. 6.11, and input electrical energy, *c.f.* Eq. 6.13, and reads:

$$\begin{aligned}\lambda &= -\frac{1}{2}(dE+sX)X/\frac{1}{2}(\varepsilon_r\varepsilon_0 E+dX)E \\ &= -(dg+sg^2)/(\varepsilon_r\varepsilon_0+dg)\end{aligned} \tag{6.A1}$$

where g is taken as X/E. Following Ref. [174, 175], the value of g where the transmission coefficient is maximum, is obtained from $d\lambda/dg$ is zero and derived as:

$$g_{max} = (X/E)_{max} = (\varepsilon_r\varepsilon_0/d)\left(-1\pm\sqrt{(1-k^2)}\right) \tag{6.A2}$$

We take only the positive sign, as the negative sign leads to a second derivate smaller than zero. The limiting values for $k \to 0$ and $k \to 1$ are:

$$lim_{k=0}g_{max} = -\frac{1}{2}(\varepsilon_r\varepsilon_0/d)k^2 = -d/2s \tag{6.A3}$$

$$lim_{k=1}g_{max} = -(\varepsilon_r\varepsilon_0/d) = -d/s \tag{6.A4}$$

Meaning that the maximum transmission coefficient is obtained at low values of k^2 when the strain induced by the external load is half of the strain generated by the electric field, and for values of k^2 approaching unity the strain induced by the external load is equal to the strain generated by the electric field. Putting the value for g_{max} in the transmission coefficient leads to:

$$\lambda_{max} = -\left(dg-\frac{1}{d}(2\varepsilon_r\varepsilon_0 sg+\varepsilon_r\varepsilon_0 d)\right)/(\varepsilon_r\varepsilon_0+dg) \tag{6.A5}$$

which can be rewritten as:

$$\begin{aligned}\lambda_{max} &= -(dg(\frac{2}{k^2}-1)+\varepsilon_r\varepsilon_0)/\left(\varepsilon_r\varepsilon_0\sqrt{(1-k^2)}\right) \\ &= \frac{2}{k^2}-1-\frac{2}{k^2}\cdot\sqrt{(1-k^2)} \\ &= \left(1/k-\sqrt{((1/k)^2-1)}\right)^2 = \left(1/k+\sqrt{((1/k)^2-1)}\right)^{-2}\end{aligned} \tag{6.A6}$$

where we have used:

$$\left(1/k-\sqrt{((1/k)^2-1)}\right)\cdot\left(1/k+\sqrt{((1/k)^2-1)}\right)=1 \tag{6.A7}$$

At small values of k^2, λ_{max} can be approximated as:

$$\lambda_{max}=\left(1/k+\sqrt{((1/k)^2-1)}\right)^{-2}\approxeq k^2/(4-2k^2) \tag{6.A8}$$

which is equal to the transmission coefficient derived for a maximum output energy, $c.f.$ Eq. 6.14.

The electrical input energy for the maximum transmission coefficient is calculated using Eq. 6.A2 for g_{max} as:

$$U_{elec}=k^2\sqrt{(1-k^2)}\left(-1+\sqrt{(1-k^2)}\right)^{-2}\cdot\frac{1}{2}sX^2=\sqrt{(1-k^2)}/\lambda_{max}\cdot\frac{1}{2}sX^2 \tag{6.A9}$$

which leads to the corresponding output energy:

$$U_{output}=\lambda_{max}U_{elec}=\sqrt{(1-k^2)}\cdot\frac{1}{2}sX^2 \tag{6.A10}$$

For low values of k^2, below about 0.6, the maximum transmission coefficient is the same as the transmission coefficient for maximum output energy, *viz.* $k^2/(4\text{-}2k^2)$. Furthermore, the expressions for both input and output energy are similar. Maximum output energy and maximum transmission coefficient are obtained when the strain of the mechanical load is half the electrically generated stress, *i.e.* X/E is equal to $-2d/s$.

At very high values of k^2, approaching 1, there is a difference. The maximum transmission coefficient goes to unity instead of $\frac{1}{2}k^2$. However, the maximum transmission coefficient is realized when the strain of the load is about equal to the strain due to the electric field. The total strain, and, hence, the output power both go to zero, as described by Eq. 6.A10. Therefore, this situation is practically irrelevant. A classical problem, the maximum transmission coefficient is unity but under that constraint you cannot harvest energy. At high k^2 don't go for the maximum transmission coefficient but simply harvest the maximum output energy.

6.B. PIEZOELECTRIC PERFORMANCE OF A PZ27 DISK AS A FUNCTION OF POLING STATE

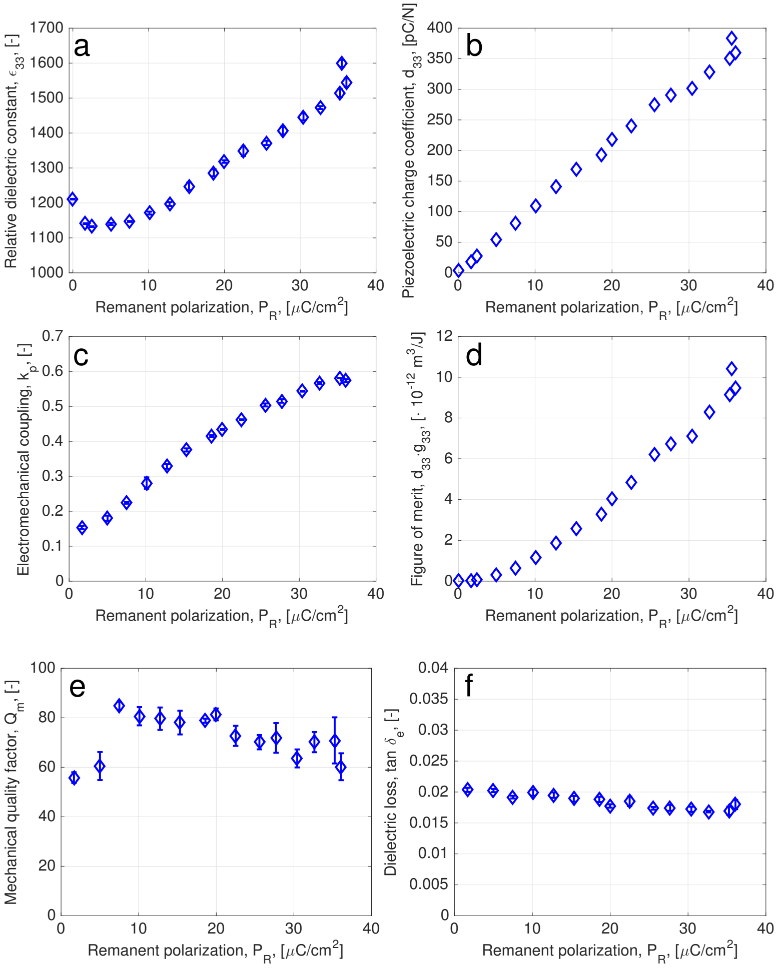

Figure B1: Electrical performance of a thermally de-poled PZ27 ceramic disk as a function of poling state, signified by the ferroelectric remanent polarization, P_R. (a) Relative dielectric constant, ε_r. (b) Piezoelectric charge coefficient, d_{33}. (c) Electromechanical coupling, k_p. (d) Figure of merit, $d_{33}g_{33}$. (e) Mechanical quality factor, Q_m. and (f) Dielectric loss, $tan\,\delta_e$.

6.C. CALCULATIONS OF THE ELASTIC STRAIN ENERGY AS A FUNCTION OF BOUNDARY CONDITIONS

FOR a square plate of dimensions of length, L, equal to breadth, b, of 10 mm and thickness, t, of 1 mm, the formula for the elastic strain energy, U, is given for each boundary condition described in the text.

For a clamped plate, U is calculated as:

$$U = \frac{F^2 t}{2AY_{PZ27}} \tag{6.C1}$$

where F is the applied force, A is the area and Y_{PZ27} is the Young's modulus of the PZ27 plate. The U of a clamped disk is also calculated from Eq. 6.C1.

Closed form solutions for a plate of the geometric ratios examined here are not available for simply supported and cantilever boundary conditions. Thus approximations were used, based on the approaches presented in Young and Budynas [186].

We approximated simply supported and cantilever plates as wide beams. In this case the stiffness needs to be corrected by replacing the Young's modulus with $Y/(1-\nu^2)$, where ν is Poisson's ratio. This approximation is, strictly speaking, only valid if the plate is loaded by a line load.

For the simply supported beam loaded in a point by a concentrated load, Young and Budynas [186] suggest using an effective width. This adjustment is applied, increasing the calculated strain energy by a factor of 1/0.568, compared to the value found using regular beam theory.

For a cantilever plate under point loading Young and Budynas [186] present a method that has been validated only for cases where the width of the plate (*i.e.* measured along the clamped side) is greater than 4 times the length (the dimension perpendicular to the clamped edge). Using this method results in a difference in calculated strain energy of about a factor 2 at the maximum applied force, when compared to treating the plate as a beam with the adjusted Young's modulus given above.

Since these approximations contain an error of at most about a factor 2, the present analysis is considered accurate enough to support the argument in this paper; that changing the boundary conditions of the piezoelectric plate is sufficient to change the applied strain energy for a given force by many orders of magnitude.

Using the well-known equation of deflection of a simply supported beam [187], and the corrected Young's modulus [186], the strain energy is given by:

$$U = \left(\frac{1-\nu^2}{Y_{PZ27}}\right)\left(\frac{F^2 L^3}{96I}\right), I = \frac{bt^3}{12} \tag{6.C2}$$

where I is the area moment of inertia.

For the cantilever plate, the strain energy also follows from standard beam theory [187] with the corrected Young's modulus:

$$U = \left(\frac{1-\nu^2}{Y_{PZ27}}\right)\left(\frac{F^2L^3}{6I}\right) \tag{6.C3}$$

The unimorph configuration chosen here is composed of a PZ27 plate perfectly bonded to an Al plate of equal width. The Al plate thickness is given by [187]:

$$t_{Al} = t_{PZ27}\sqrt{Y_{PZ27}/Y_{Al}} \tag{6.C4}$$

This ensures that the neutral axis of the unimorph coincides with the interface between the piezo and Al material. In this way the full volume of the piezo material experiences compressive stress.

To calculate the strain energy of this unimorph configuration, we analytically transform the bimaterial beam into an equivalent beam made entirely of Al. To compensate for the difference in Young's modulus between the PZ27 ceramic and Al, the width of the part of the beam formerly made of piezoceramic is increased, by a factor Y_{PZ27}/Y_{Al}.

For a unimorph geometry a difference in the Poisson's ratio of the two materials will cause non-uniform strain in thickness direction, resulting in in-plane stresses [186]. The plate will be somewhat stiffer than when the Poisson's ratios are the same, somewhat lowering the strain energy, for a given force. We note that the difference in the Poisson's ratio of Al (0.33) and PZ27 ceramics (0.35) is small, therefore the effect on the strain energy, for a given force, is minor.

The equations above for the strain energy of plates remain valid for the unimorph configuration, with the following modifications: the properties of Al are used for Y and ν, and I is replaced with:

$$I = \left(\frac{Y_{PZ27}}{Y_{Al}}\right)\left(\frac{bt^3_{PZ27}}{3}\right)\left(\frac{bt^3_{Al}}{3}\right) \tag{6.C5}$$

The strain, x, of the piezoelectric material then follows from:

$$x = \frac{X(1-\nu^2)}{Y_{PZ27}} \tag{6.C6}$$

where X is the stress. In a clamped plate and disk the stress is given by $X = F/A$. The maximum stress in the simply supported plate, cantilever plate and cantilever unimorph is given by: $X_{max} = \frac{M}{I}y$, where I is the same as above, M is the internal moment, and y is the perpendicular distance from the neutral axis to a point farthest away from the neutral axis, where X_{max} acts.

6.D. CONVERSION EFFICIENCY OF PIEZOELECTRIC ENERGY HARVESTING WITH A RESISTIVE LOAD

A RESISTIVE load, R_{load}, is placed in parallel to the piezoelectric capacitor to harvest the stored electrical energy. The corresponding electric circuit is presented in Fig. D1. In this case, the piezoelectric capacitor is treated as a current source, I_{in}, actuated with an applied force over time, $F(\omega t) = F_{max} f(\omega t)$, where $f(\omega t)$ is a periodic function (for example, $sin(\omega t)$), where t is the time and ω the angular frequency. The developed current, I_{in}, is the sum of the current due to the internal capacitance, I_{cap}, and the external load, I_{load}.

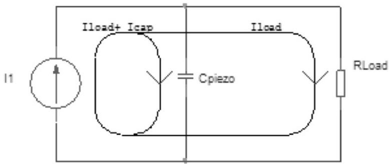

Figure D1: Electric circuit of a piezoelectric capacitor in parallel with a resistive load.

The harvested power output, P, of the circuit is related to the square of the output voltage, $V_{harvested}$, and the value of the resistive load through:

$$P = \frac{V^2_{harvested}}{R_{load}} = \frac{\left(\left|\frac{I_{in}R_{load}}{1+j\omega C_{piezo}}\right|\right)^2}{R_{load}} \tag{6.D1}$$

where C_{piezo} is the internal capacitance of the piezoelectric material, and j is $\sqrt{-1}$.

As an example, the power output of a PZ27 ceramic, actuated with a sinusoidal excitation at 10 Hz and 3 N peak to peak, is presented in Fig. D2a. The piezoelectric disk has a capacitance of 1145 pF. The calculated power output (Eq. 6.D1) takes the form of a parabola, at values of the resistive load between 10^6 and 10^8 Ω. A good agreement is obtained between the measured values and the calculation. The maximum power point is calculated at a resistive load of 13.9 MΩ. It occurs when the value of the resistive load, R_{load} optimal, is equal to the impedance of the piezoelectric capacitor, at $R_{load\ optimal} = \omega C_{piezo}$. This is confirmed by calculating the power as a function of the ratio between the resistive load and the impedance of the internal capacitance, presented in Fig. D2b.

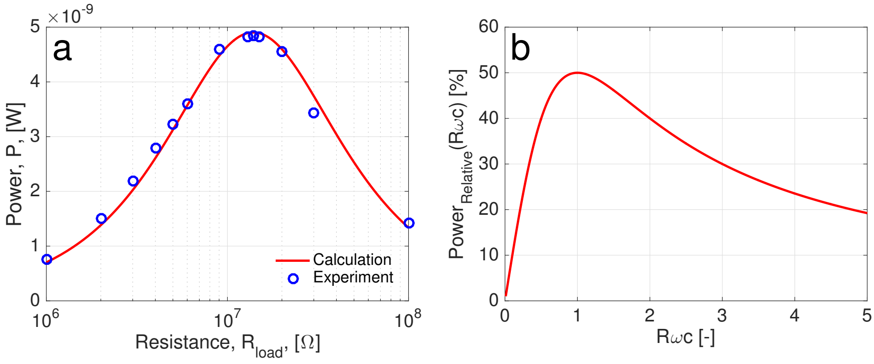

Figure D2: Energy harvesting output of a piezoelectric capacitor. (a) The power output of a PZ27 ceramic as a function of the resistive load, actuated with a sinusoidal excitation at 10 Hz, and 3 N peak to peak. The red line is calculated with Eq. 6.D1. The open circles represent measurements of a PZ27 ceramic disk. (b) The dependence of the relative power output on the ratio between the applied resistive load, R, and the impedance of the internal capacitance, $Z = 1/j\omega C$, calculated with Eq. 6.D1, with normalized x-axes to $R_{load}\omega C$.

To identify the electrical-electrical conversion efficiency, the power obtained with the resistive load can be compared to the internal power in open circuit, P_{open}, where $V_{open}(\omega t)$ is the voltage in open circuit $V_{open}(\omega t) = V_{max} f(\omega t)$.

$$P_{open} = \frac{\left(\frac{V_{open}}{\sqrt{2}}\right)^2}{\omega C_{piezo}} \tag{6.D2}$$

The term ‘open circuit power’ is thermodynamically not defined. However, here we used this artificial term to clearly distinguish between the internal energy stored in the piezoelectric transducer, P_{open}, and the energy that can be externally dissipated in the load, $P_{harvested}$.

The maximum power is obtained when $R\omega C_{piezo}$ is 1, or the value of the resistive load is equal to $1/\omega C_{piezo}$, and is equal to 50% P_{open}.

In summary, at $R_{load} = 1/\omega C_{piezo}$ the relationship between the open circuit voltage (taken from Eq. 6.D2) and the harvested voltage (taken from Eq. 6.D1) reduces to:

$$V_{harvested} = \frac{1}{\sqrt{2}} V_{open} \tag{6.D3}$$

The powers scale with the square of the voltage, meaning that:

$$P_{harvested} = \left(\frac{1}{\sqrt{2}}\right)^2 P_{open} = \frac{1}{2} P_{open} \tag{6.D4}$$

Or, half of the internal open circuit power is transferred to harvested power when using a resistive load.

SUMMARY

THE main objective of this thesis was to develop new piezoelectric ceramic polymer composites that maintain the ease of manufacturing of random composites and could function as a human touch sensor, while simultaneously exploring their potential as energy harvesters.

In **Chapter 2** a range of polydisperse $[K_{0.5}Na_{0.5}]_{(1-x)}Li_xNbO_3$ (KNLN) microcube powders were prepared with the principle aim to identify the optimal composition and processing scheme for enhancing the piezoelectric voltage sensitivity, g, in aligned ceramic polymer composites. Five powders were prepared with 0 to 12 mol.% of Li, in steps of 3, and calcined first at 1050 °C for 3 h and then at 950 °C for 20 h. The KNLN powders with 9 and 12 mol.% of Li had a tetragonal perovskite crystal structure, while the powders from 0 to 6 mol.% were orthorhombic. 10 vol.% of piezoceramic microcubes were randomly dispersed in an epoxy matrix and aligned, in the poling direction, by dielectrophoresis. The relative dielectric constant, ε_r, and dielectric loss, $tan\ \delta_e$, of the composites was hardly affected by variations in Li content and microstructure. Tetragonal compositions contained both fractured particles and a minor non-perovskite second phase which diminished the piezoelectric charge coefficient, d, in those composites. The piezoelectric charge coefficients, d, were markedly higher on the orthorhombic side of the phase diagram. As the d of random orthorhombic composites was independent of Li content, it was striking that a peak could be identified at 3 mol.% of Li in aligned composites. It was inferred that the larger particle size of the microcubes at 3 mol.% of Li was the reason for the increased d in aligned composites, due to the smaller number of polymer interfaces per chain. Yet, no clear conclusions could be drawn since, particle size, degree of polydispersity and the electrical properties of the microcubes varied with Li content. For the first time, the electromechancial coupling of 10 vol.% aligned piezoelectric particle composites could be measured via frequency response analysis.

In **Chapter 3** piezoelectric, flexible films were fabricated by dispersing the lead-free piezoceramic $K_{0.485}Na_{0.485}Li_{0.03}NbO_3$ (KNLN) microcube powder, identified in Chapter 2, into an elastomeric PDMS matrix. Before curing the films, the particles were aligned using a dielectrophoretic field. The dielectric constant of the composite films was almost independent of the microstructure, dominated by that of the PDMS matrix and increases linearly with filler fraction. On the other hand, upon aligning, the piezoelectric charge coefficient, d, increased more than ten fold, up to 17 pC/N. Quantitative analysis showed that the origin was a reduction of the inter-particle distance to under 1.0 μm in the aligned bi-continuous chains. The piezoelectric voltage coefficient, g, exhibited a maximum value of 220 mV.m/N, at a volume fraction of only 10 %. This value was more than one order of magnitude higher than that obtained for randomly dispersed particle composites and comparable to values reported for the piezoelectric polymers PVDF and P(VDF-

TrFE). The composite films were implemented in a touch sensor. The high sensitivity of the sensor was demonstrated under a controlled dynamical change of applied force via measuring the open circuit voltage, and by finger tapping a load matched and amplified flexible touch patch. These biocompatible, piezoelectric KNLN composite films combine the best of both worlds; the coercive field and the Curie temperature are dominated by that of the KNLN ceramics, while due to the low loading levels the mechanical properties resemble those of PDMS.

In **Chapter 4** a new method to upscale the dielectrophoretic alignment of ceramic particles in a polymer matrix was developed. Piezoelectric lead zirconium titanate (PZT) particles were aligned, perpendicular to the poling direction, in a urethane dimethacrylate (UDMA) matrix. The dielectrophoretic alignment field was set between an Al electrode track and a moving doctor blade. The in-plane aligned composite films were photocured during tape casting. The piezoelectric charge coefficient and relative dielectric constant of thickness direction poled, in-plane aligned composites was identical to randomly dispersed and tape casted composites. The required time for spherical PZT particles to align in this UDMA matrix was shown to be incompatible with the speed required to reliably cast and cure composite films. Adding a DC bias to the dielectrophoretic alignment field to induce in-plane poling while tape casting did not noticeably affect the piezoelectric charge coefficient, even though the DC bias was effective at poling composites fabricated with a stationary electric field. A touch sensing component consisting of a random composites with 50 vol.% of PZT filler, prepared at a speed of 0.5 mm/s, was fabricated for a responsive placemat technology demonstrator.

In **Chapter 5** the shear mode piezoelectric charge coefficient of ceramic-polymer composites was characterized for the first time. Rings and disks of 0 to 30 vol.% PZT particles in an epoxy matrix were prepared to study the shear and tensile response to strain, respectively. The shear mode piezoelectric charge coefficient was quantitatively examined with adjusted established analytical models and a newly developed finite element reduced volume element model (FE-RVE) in COMSOL.The FE-RVE simulations showed close agreement with the experimental data and demonstrated that, next to particle morphology, particle orientation within the particulate composite was a contributing factor to the macroscopic shear mode behavior. The shear, d_{15} mode, piezoelectric charge coefficient was shown to be 1.2 times larger than the longitudinal d_{33} mode, which is consistent with monolithic PZT ceramics. While the absolute energy harvesting level of the composites loaded in shear remained relatively low, its performance was better than that of the same composite loaded in longitudinal tension or compression.

In **Chapter 6** it was analytically derived that for an energy harvester, comprising a piezoelectric capacitor with mechanical load, the maximum output energy, per unit volume, per impact pulse is given by $1/(4-2k^2)\cdot 1/2dgX^2$, where X is the applied stress, k is the electromechanical coupling factor and dg the figure of merit for piezoelectric energy harvesters. A sensitive piezometer system was developed that, with high accuracy, was used to measure the output energy under sinusoidal impact excitation. Both the open circuit voltage and short circuit current could be measured of clamped piezoelec-

tric components subjected to dynamic loads up to 20 N, in a variety of waveforms. The output energy was measured for intermediate polarization states of a soft PZT piezoceramic, and for a wide variety of ferroelectric materials. The polarization state of the soft PZT ceramic was controlled by iteratively poling thermally depolarized disks in a Radiant High Voltage Tester. The relative dielectric constant, piezoelectric charge coefficient, electromechanical coupling and figure of merit increased with the remanent polarization, while the mechanical quality factor and dielectric loss decreased. The measured electrical output energy was compared to the analytically derived mechanical input energy in the disk, and the difference was confirmed to be equal to k^2. The experimentally measured output energy could perfectly be described, over more than three orders of magnitude, by the derived expression $1/(4-2k^2)\cdot 1/2dgX^2$. In the limits of k, the prefactor $1/(4-2k^2)$ varies only between 1/4 and 1/2 meaning that the figure of merit of a piezoelectric energy harvester is not k^2 but dg.

SAMENVATTING

HET doel van het onderzoek als beschreven in dit proefschrift was om te komen tot nieuwe piëzo-elektrische composieten bestaande uit (geordende) keramische deeltjes in een passende flexibele polymerenmatrix. De composieten zouden geschikt moeten zijn voor 'touch based' sensoren en relatief eenvoudig geproduceerd moeten kunnen worden. Het proefschrift beschrijft niet alleen de ontwikkeling en prestaties van de nieuwe materialen maar gaat ook in op enige fundamentele fysische aspecten van het omzetten van mechanische energie in elektrische energie in dergelijke composieten.

In **Hoofdstuk 2** is gezocht naar de optimale samenstelling van $[\mathrm{K}_{0.5}\mathrm{Na}_{0.5}]_{(1-x)}\mathrm{Li}_x\mathrm{NbO}_3$ (KNLN) poeders, met een variabel Li gehalte varïerend van $x = 0.00$ tot $x = 0.12$, om te komen tot composieten met zo hoog mogelijke piëzo-elektrische spanningscoëfficiënt, g. De KNLN poeders met 9 en 12 mol% Li hadden een tetragonale perovskiet kristalstructuur, terwijl de poeders met een Li gehalte van 6% of lager een orthorhombisch kristalstructuur hadden. De piëzokeramische poeders werden voorafgaande aan uit uitharden van de epoxy matrix uitgelijnd door middel van diëlectroforese bij een vaste volume fractie van 10 vol.%. De waardes van de relatieve diëlektrische constante, ε_r, en het dilectrische verlies, $tan\ \delta_e$, bleken nauwelijks af te hangen van het Li-gehalte of de microstructuur van de uitgelijnde deeltjescomposieten. De piëzo-elektrische ladingscoëfficiënten, d, waren duidelijk hoger voor composieten gemaakt met orthorhombische deeltjes met samenstellingen dicht bij de fasegrens. Opvallend genoeg ontbrak dit optimum in composieten waarbij de deeltjes quasi-homogeen en ongeordend in de matrix verdeeld waren. Een sluitende verklaring voor de waargenomen afhankelijkheden kon niet gegeven worden omdat de gemiddelde deeltjesgrootte , deeltjesgrootteverdeling en intrinsieke piëzo-elektrische eigenschappen van de verschillende poeders niet onafhankelijk van elkaar gevarieerd konden worden. Qua methodologie was dit de eerste keer dat de elektromechanische koppelfactor van getextureerde piëzo-elektrische composieten gemeten is middels een frequentieresponsanalyse.

In **Hoofdstuk 3** worden flexibele piëzo-elektrische films bestaande uit de in Hoofdstuk 2 beschreven loodvrije (KNLN)piëzo-keramische deeltje en een PDMS-matrix gepresenteerd . Wederom waren de deeltjes middels een diëlektroforetisch veld uitgelijnd voordat crosslinking van de matrix plaatsvond. De diëlektrische constant van de composietfilms was werd gedomineerd door de diëlektrische constante van de PDMS-matrix en nam lineair toe met de volumefractie KNLN poeder en was bijna onafhankelijk van de microstructuur. Daarentegen nam de piëzo-elektrische ladingscoëfficiënt, d, bij uitlijning van de deeltjes meer dan tien keer toe, tot 17 pC/N. Uit semi-kwantitatieve analyse bleek dat de verbetering het gevolg was van een verkleining van de gemiddelde afstand tussen de deeltjes in de uitgelijnde bi-continue ketens tot onder 1,0 μm. De piëzo-elektrische spanningscoëfficiënt, g , vertoonde een maximale waarde van 220 mV.m/N, bij een volumefractie van slechts 10 vol% KNLN poeder. Deze waarde was meer dan een ordegrootte hoger dan die verkregen voor een composiet met quasi-homogeen verdeelde deeltjes. De verkregen maximale waarde is vergelijkbaar met die voor piëzo-elektrische polymeren PVDF en P(VDF-TrFE). De optimale films werden door het aanbrengen van elektrodes omgebouwd tot een druksensor. De hoge gevoeligheid van de sensor bleek uit een grote dynamische verandering van de open klemspanning bij handmatige belasting van de films met lichte vingerdruk. Deze lood-vrije,piëzo-elektrische KNLN - PDMS composietfilms combineren twee wenselijke sensor karakteristieken; De hoge piëzo-elektrische gevoeligheid en de hoge maximale gebruikstemperatuur worden bepaald door de KNLN fractie en de grote flexibiliteit en taaiheid bij kamertemperatuur en daarboven worden bepaald door de PDMS matrix.

In **Hoofdstuk 4** werd een nieuwe methode ontwikkeld om de diëlektroforetische uitlijning van keramische loodzirkoniumtitanaat (PZT) deeltjes in een urethaan dimethylacrylaat (UDMA) film op te schalen. In de opstelling werd een dielectroforetisch veld aangelegd tussen een Aluminium onder-electrode en het bewegende ‘doctorblade’ waarmee het niet-uitgeharde polymeer-keramiek mengsel op een ingestelde filmdikte van 100 μm gestreken werd. Vrijwel gelijktijdig met het aanbrengen van de vervorming werd het polymeer-keramiek mengsel uitgehard middels blootstelling aan blauw licht teneinde de beoogde horizontale uitlijning van de deeltjes ‘in te vriezen’. De waardes van de piëzo-elektrische ladingscoëfficiënt en de relatieve dielektrische constante bleken na het polen even laag als die van niet-uitgelijnde composiet films. Daaruit bleek dat de tijd benodigd om deze PZT-deeltjes met hun lage vormfactor in deze UDMA-matrix topologisch uit te lijnen veel langer was dan de maximale productietijd waarbij films van homogene dikte en struktuur via het ‘doctor-blade’ concept gemaakt kunnen worden. Het combineren van een gelijkspanningsveld en het diëlektroforetische wisselspanningsveld teneinde de deeltjes gelijktijdig uit te lijnen en te polen tijdens de filmproductie, bleek een te verwaarlozen effect op de piëzo-elektrische ladingscoëfficiënt te hebben, hoewel deze benadering bij stapsgewijze productie wel bleek te werken. De beste combinatie van piëzo-elektrisch en mechanisch gedrag werd verkregen bij hoge PZT vulgraden en een werkende druksensor kon worden vervaardigd op basis van een ongetextureerde composiet film met een vulgraad van 50 vol% PZT.

In **Hoofdstuk 5** werd voor zover bekend voor de eerste keer de piëzo-elektrische ladingscoëfficiënt van keramische-polymeercomposieten onder een afschuifbelasting gemeten en geanalyseerd. Daartoe werden dunne ring- en schijfvormige preparaten van een epoxy met daarin 0 tot 30 vol% PZT bereid, welke daarna zowel onder trek als afschuiving gemeten onder bepaling van het resulterende elektrische signaal. De piëzo-elektrische ladingscoëfficiënt onder trek en onder afschuiving als functie van de vulgraad werden berekend middels aangepaste analytische modellen en een nieuw ‘finite element reduced volume element’ (FE-RVE) model in COMSOL. De resultaten van de FE-RVE-simulaties kwamen goed overeen met de experimentele data en toonden aan dat, naast deeltjesmorfologie, de deeltjesoriëntatie binnen de composiet een belangrijke bijdrage levert aan het macroscopische gedrag. De waarde van de piëzo-elektrische ladingscoëfficiënt, onder afschuiving, de d_{15}-modus, bleek 20% hoger dan de waarde onder uniaxiale trek, de d_{33}-modus. Deze verhouding is consistent met de verhouding zoals die gemeten is aan monolithische PZT-keramiek. Ook al was het absolute 'energy-harvesting' niveau van de composieten onder een afschuifbelasting relatief laag, toch bleek de prestatie beter te zijn dan die van identieke composieten belast onder uniaxiale trek of druk.

In **Hoofdstuk 6** is het analytisch afgeleid dat om energie te oogsten, door middel van een met mechanische belasting, de maximale elektrische energie per sensor volume per opgelegde impuls, welke geoogst kan worden uit een mechanisch belaste piëzo-elektrische condensator wordt gegeven door $1/(4-2k^2)\cdot 1/2dgX^2$, waar X de opgelegde mechanische drukspanning, k de elektromechanische koppelfactor, en dg de efficiency factor van een piëzo-elektrische energieopnemer. Er werd een gevoelig piëzometersysteem ontwikkeld dat onder nauwkeurig gecontroleerde omstandigheden gebruikt werd om de extraheerbare elektrische energie te meten bij een opgelegde sinusvormige belasting met een amplitude tot 20 N. In de opstelling wordt zowel de open klemspanning gemeten als de kortsluitstroomsterkte. De elektrische energieafdracht werd voor diverse polarisatiecondities gemeten aan een 'zachte' PZT variant alsmede aan een grote diversiteit van ferro-elektrische materialen. De polarisatietoestand van het zachte PZT-keramiek werd gevarieerd door iteratief polen van thermisch gedepolariseerde schijfvormige preparaten in een Radiant High Voltage Tester. De relatieve diëlektrische constante, de piëzo-elektrische ladingscoëfficiënt, de elektromechanische koppeling en het product dg namen toe met de 'remanente polarisatie', terwijl de mechanische kwaliteitsfactor k en het diëlektrische verlies daalden. Ook werd bevestigd dat het verschil tussen de gemeten uitgaande elektrische en de analytisch afgeleide ingaande mechanische energie in de schijf gelijk is aan k^2. De experimenteel gemeten elektrische energie als functie van de ingaande mechanische energie kon voor deze brede groep van materialen, over meer dan drie ordes van grootte, perfect beschreven worden met de afgeleide uitdrukking $1/(4-2k^2)\cdot 1/2dgX^2$. Voor alle mogelijke waarden van k varieert de factor $1/(4-2k^2)$ slechts tussen 1/4 en 1/2, waardoor de presentatiefactor van een piëzo-elektrische energieopnemer niet k^2 is maar dg.

REFERENCES

[1] A. Meitzler, D. Berlincourt, G. Coquin, F. Welsh, H. Tiersten, and A. Warner, *IEEE standards on piezoelectricity ANSI/IEEE Std 176*, Tech. Rep. (The Institute of Electrical and Electronics Engineers, Inc., New York, New York, USA, 1987).

[2] M. G. Lippmann, *On the principle of the conservation of electricity,* Philosophical Magazine Series 5 **12**, 151 (1881).

[3] J. Holterman and P. Groen, *An introduction to piezoelectric materials and applications* (Stichting Applied Piezo, Apeldoorn, the Netherlands, 2013).

[4] E. Wainer, *High titania dielectrics,* Transactions of the Electrochemical Society **89**, 331 (1946).

[5] T. Ogawa, *On barium titanate ceramics,* Busseiron Kenkyu **6** (1947), (in Japanese).

[6] B. Vul, *High and ultrahigh dielectric constant materials,* Electrichestvo **3**, 12 (1946), (in Russian).

[7] V. L. Stuber, *Lead free high aspect ratio piezoelectric composite energy harvesters,* Master's thesis, Delft University of Technology (2017).

[8] T. Rödig, A. Schönecker, and G. Gerlach, *A survey on piezoelectric ceramics for generator applications,* Journal of the American Ceramic Society **93**, 901 (2010).

[9] B. Jaffe, W. R. Cook Jr., and H. Jaffe, *Piezoelectric ceramics* (Academic Press, London, United Kingdom and New York, USA, 1971).

[10] A. L. Kholkin, N. A. Pertsev, and A. V. Goltsev, *Chapter 2: Piezoelectricity and crystal symmetry,* in *Piezoelectric and Acoustic Materials for Transducer Applications* (Springer Science+Business Media, LLC 2008, 2008) pp. 17–38.

[11] X.-h. X.-H. Du, J. Zheng, U. Belegundu, and K. Uchino, *Crystal orientation dependence of piezoelectric properties of lead zirconate titanate near the morphotropic phase boundary,* Applied Physics Letters **72**, 2421 (1998).

[12] K. Uchino, *Glory of piezoelectric perovskites,* Sci. Technol. Adv. Mater **16**, 46001 (2015).

[13] M. Davis, M. Budimir, D. Damjanovic, and N. Setter, *Rotator and extender ferroelectrics: Importance of the shear coefficient to the piezoelectric properties of domain-engineered crystals and ceramics,* Journal of Applied Physics **101**, 054112 (2007).

[14] E. Sawaguchi, G. Shirane, and Y. Takagi, *Phase transition in lead zirconate,* Journal of the Physical Society of Japan **6**, 333 (1951).

[15] B. Jaffe, *Piezoelectric transducers using lead titanate and lead zirconate,* (1955), uS Patent 2,708,244.

[16] W. Liu and X. Ren, *Large piezoelectric effect in pb-free ceramics,* Phys. Rev. Lett. **103**, 257602 (2009).

[17] P. K. Panda and B. Sahoo, *PZT to lead free piezo ceramics: a review,* Ferroelectrics **474**, 128 (2015).

[18] T. R. Shrout and S. J. Zhang, *Lead-free piezoelectric ceramics: Alternatives for PZT?* Journal of Electroceramics **19**, 113 (2007).

[19] J. Rödel, K. G. Webber, R. Dittmer, W. Jo, M. Kimura, and D. Damjanovic, *Transferring lead-free piezoelectric ceramics into application,* Journal of the European Ceramic Society **35**, 1659 (2015).

[20] Y. Guo, K.-i. Kakimoto, and H. Ohsato, *Phase transitional behavior and piezoelectric properties of* $(Na_{0.5}K_{0.5})NbO_3$-$LiNbO_3$ *ceramics,* Applied Physics Letters **85**, 4121 (2004).

[21] S. Wongsaenmai, S. Ananta, and R. Yimnirun, *Effect of Li addition on phase formation behavior and electrical properties of* $(K_{0.5}Na_{0.5})NbO_3$ *lead free ceramics,* Ceramics International **38**, 147 (2012).

[22] J.-F. Li, K. Wang, F.-Y. Zhu, L.-Q. Cheng, and F.-Z. Yao, $(K,Na)NbO_3$*-based lead-free piezoceramics: Fundamental aspects, processing technologies, and remaining challenges,* Journal of the American Ceramic Society **96**, 3677 (2013).

[23] Y. Saito, H. Takao, T. Tani, T. Nonoyama, K. Takatori, T. Homma, T. Nagaya, and M. Nakamura, *Lead-free piezoceramics,* Nature **432**, 84 (2004).

[24] S. A. S. Piezotech, *Piezoelectric Films Technical Information*, Tech. Rep. (Hesingue, France, 2012).

[25] H. Kawai, *The piezoelectricity of poly(vinylidene fluoride),* Japanese Journal of Applied Physics **8**, 975 (1969).

[26] T. Furukawa, *Piezoelectricity and pyroelectricity in polymers,* IEEE Transactions on Electrical Insulation **24**, 375 (1989).

[27] I. Katsouras, K. Asadi, M. Li, T. B. van Driel, K. S. Kjær, D. Zhao, T. Lenz, Y. Gu, P. W. M. Blom, D. Damjanovic, M. M. Nielsen, and D. M. de Leeuw, *The negative piezoelectric effect of the ferroelectric polymer poly(vinylidene fluoride),* Nature Materials **15**, 78 (2016).

[28] T. Kitayama and S. Sugawara, *Piezoelectric and pyroelectric properties of polymer-ferroelectric composites,* Professional Report Gr. Inst. Elec. Comm. Eng. Japan , CPM72 (1972), (in Japanese).

[29] E. K. Akdogan, M. Allahverdi, and A. Safari, *Piezoelectric Composites for Sensor and Actuator Applications,* IEEE transactions on ultrasonics, ferroelectrics, and frequency control **52**, 746 (2005).

[30] R. E. Newnham, D. P. Skinner, and L. E. Cross, *Connectivity and piezoelectric-pyroelectric composites,* Materials Research **13**, 525 (1978).

[31] C. Dias, D. Das-Gupta, Y. Hinton, and R. Shuford, *Polymer/ceramic composites for piezoelectric sensors,* Sensors and Actuators A: Physical **37-38**, 343 (1993).

[32] A. Pelaiz-Barranco and P. Marin-Franch, *Piezo-, pyro-, ferro-, and dielectric properties of ceramic/polymer composites obtained from two modifications of lead titanate,* Journal of Applied Physics **97**, 034104 (2005).

[33] G. Sa-Gong, A. Safari, S. J. Jang, and R. E. Newnham, *Poling flexible piezoelectric composites,* Ferroelectrics Letters Section **5**, 131 (1986).

[34] T. Yamada, T. Ueda, and T. Kitayama, *Piezoelectricity of a high-content lead zirconate titanate/polymer composite,* Journal of Applied Physics **53**, 4328 (1982).

[35] H. Banno and S. Saito, *Piezoelectric and dielectric properties of Composits of synthetic rubber and* $PbTiO_3$ *and PZT,* Japanese Journal of Applied Physics **22**, 67 (1983).

[36] K. A. Klicker, *Piezoelectric composite with 3–1 connectivity for transducer applications*, Ph.D. thesis, Pennsylvania State University (1980).

[37] C. P. Bowen, R. E. Newnham, and C. A. Randall, *Dielectric properties of dielectrophoretically assembled particulate-polymer composites,* Journal of Materials Research **13**, 205 (1998).

[38] S. A. Wilson, G. M. Maistros, and R. W. Whatmore, *Structure modification of 0-3 piezoelectric ceramic/polymer composites through dielectrophoresis,* Journal of Applied Physics D: Applied Physics **38**, 175 (2005).

[39] D. A. van den Ende, B. F. Bory, W. A. Groen, and S. van der Zwaag, *Improving the* d_{33} *and* g_{33} *properties of 0-3 piezoelectric composites by dielectrophoresis,* Journal of Applied Physics **107**, 024107 (2010).

[40] N. K. James, D. B. Deutz, R. K. Bose, S. van der Zwaag, and W. A. Groen, *High piezoelectric voltage coefficient in structured lead-free* $(K,Na,Li)NbO_3$ *particulate-epoxy composites,* Journal of the American Ceramic Society **99**, 3957 (2016).

[41] S. P. Beeby, M. J. Tudor, and N. M. White, *Energy harvesting vibration sources for microsystems applications,* Measurement Science and Technology **17**, R175 (2006).

[42] B. P. D. Mitcheson, M. Ieee, E. M. Yeatman, S. M. Ieee, G. K. Rao, S. M. Ieee, A. S. Holmes, and T. C. Green, *Energy harvesting from human and machine motion for wireless electronic devices,* Proceedings of the IEEE **96**, 1457 (2008).

[43] K. A. Cook-Chennault, N. Thambi, M. A. Bitetto, and E. B. Hameyie, *Piezoelectric energy harvesting: A green and clean alternative for sustained power production,* Bulletin of Science, Technology & Society **28**, 496 (2008).

[44] H. Li, C. Tian, and Z. D. Deng, *Energy harvesting from low frequency applications using piezoelectric materials,* Applied Physics Reviews **1**, 041301 (2014).

[45] S. Bauer and F. Bauer, *Piezoelectric polymers and their applications,* in *Piezoelectricity: Evolution and Future of a Technology* (Springer Berlin Heidelberg, Berlin, Heidelberg, 2008) pp. 157–177.

[46] S. Bauer, R. Gerhard-Multhaupt, and G. M. Sessler, *Ferroelectrets: Soft electroactive foams for transducers,* Physics Today **57**, 37 (2004).

[47] A. Mellinger, M. Wegener, W. Wirges, R. R. Mallepally, and R. Gerhard-Multhaupt, *Thermal and temporal stability of ferroelectret films made from cellular polypropylene/air composites,* Ferroelectrics **331**, 189 (2006).

[48] W. Li, D. Torres, T. Wang, C. Wang, and N. Sepúlveda, *Flexible and biocompatible polypropylene ferroelectret nanogenerator (FENG): On the path toward wearable devices powered by human motion,* Nano Energy **30**, 649 (2016).

[49] C. K. Jeong, K.-I. Park, J. Ryu, G.-T. Hwang, and K. J. Lee, *Large-area and flexible lead-free nanocomposite generator using alkaline niobate particles and metal nanorod filler,* Advanced Functional Materials **24**, 2620 (2014).

[50] Q.-t. Xue, Z. Wang, H. Tian, Y. Huan, Q.-Y. Xie, Y. Yang, D. Xie, C. Li, Y. Shu, X.-H. Wang, and T.-L. Ren, *A record flexible piezoelectric KNN ultrafine-grained nanopowder-based nanogenerator,* AIP Advances **5**, 017102 (2015).

[51] M. K. Gupta, S.-W. Kim, and B. Kumar, *Flexible high-performance lead-free* $Na_{0.47}K_{0.47}Li_{0.06}NbO_3$ *microcube-structure-based piezoelectric energy harvester,* ACS Applied Materials & Interfaces **8**, 1766 (2016).

[52] C. Yang and C.-P. Fritzen, *Piezoelectric paint: characterization for further applications,* Smart Materials and Structures **21**, 045017 (2012).

[53] J. H. Jung, C.-Y. Chen, B. K. Yun, N. Lee, Y. Zhou, W. Jo, L.-J. Chou, and Z. L. Wang, *Lead-free* $KNbO_3$ *ferroelectric nanorod based flexible nanogenerators and capacitors.* Nanotechnology **23**, 375401 (2012).

[54] J.-H. Seol, J. S. Lee, H.-N. Ji, Y.-P. Ok, G. P. Kong, K.-S. Kim, C. Y. Kim, and W.-P. Tai, *Piezoelectric and dielectric properties of* $(K_{0.44}Na_{0.52}Li_{0.04})(Nb_{0.86}Ta_{0.10}Sb_{0.04})O_3$*-PVDF composites,* Ceramics International **38**, S263 (2012).

[55] D. T. Le, N. B. Do, D. U. Kim, I. Hong, I.-W. Kim, and J. S. Lee, *Preparation and characterization of lead-free* $(K_{0.47}Na_{0.51}Li_{0.02})(Nb_{0.8}Ta_{0.2})O_3$ *piezoceramic/epoxy composites with 0-3 connectivity,* Ceramics International **38**, S259 (2012).

[56] Z.-Y. Shen, J.-F. Li, R. Chen, Q. Zhou, and K. K. Shung, *Microscale 1-3-type (Na,K)NbO$_3$-based Pb-free piezocomposites for high-frequency ultrasonic transducer applications,* Journal of the American Ceramic Society **94**, 1346 (2011).

[57] D. A. van den Ende, W. A. Groen, and S. van der Zwaag, *Robust piezoelectric composites for energy harvesting in high-strain environments,* Journal of Intelligent Material Systems and Structures **24**, 2262 (2012).

[58] X. Fang, J. He, and Y. Zhang, *Preparation and Characterization of Large-Area and Flexible Lead Zirconate Titanate / Polyvinyl-Butyral / Additives Composite Films for Piezoelectric Sensor Application,* Sensors and Materials **28**, 681 (2016).

[59] K. N. Kim, J. Chun, S. a. Chae, C. W. Ahn, I. W. Kim, S.-W. Kim, Z. L. Wang, and J. M. Baik, *Silk fibroin-based biodegradable piezoelectric composite nanogenerators using lead-free ferroelectric nanoparticles,* Nano Energy **14**, 87 (2015).

[60] *Morgan Advanced Materials Techincal Datasheet PZT500 Series,* (2013).

[61] J. Rödel, W. Jo, K. T. P. Seifert, E.-M. Anton, T. Granzow, and D. Damjanovic, *Perspective on the Development of Lead-free Piezoceramics,* Journal of the American Ceramic Society **92**, 1153 (2009).

[62] G. T. Davis, *Piezoelectric and Pyroelectric Polymers,* in *Polymers for Electronic and Photonic Applications*, edited by C. Wong (Academic Press Limited, London, UK, 1992) pp. 435–461.

[63] C. J. Dias and D. K. Das-Gupta, *Inorganic ceramic / polymer ferroelectric composite electrets,* IEEE Transactions on Dielectrics and Electrical Insulation **3**, 706 (1996).

[64] D. B. Deutz, N. T. Mascarenhas, S. van der Zwaag, and W. A. Groen, *Enhancing energy harvesting potential of (K,Na,Li)NbO$_3$-epoxy composites via Li substitution,* Journal of the American Ceramic Society **100**, 1108 (2017).

[65] D. B. Deutz, N. T. Mascarenhas, J. B. J. Schelen, D. M. de Leeuw, S. van der Zwaag, and W. A. Groen, *Flexible piezoelectric touch sensor by alignment of lead-free alkaline niobate microcubes in PDMS,* Advanced Functional Materials **27**, 1700728 (2017).

[66] D. B. Deutz, N. T. Mascarenhas, S. van der Zwaag, and W. A. Groen, *Poling piezoelectric (K,Na,Li)NbO$_3$-polydimethylsiloxane composites,* Ferroelectrics (2017), 10.1080/00150193.2017.1360110, in press.

[67] D. B. Deutz, E. Tempelman, S. van der Zwaag, and W. A. Groen, *Piezoelectric lead zirconium titanate composite touch sensors for integration with flexible OLED technology,* Ferroelectrics **480**, 1 (2015).

[68] F. Van Loock, D. B. Deutz, S. van der Zwaag, and W. A. Groen, *Exploring the piezoelectric performance of PZT particulate-epoxy composites loaded in shear,* Smart Materials and Structures **25**, 085039 (2016).

[69] D. B. Deutz, J.-A. Pascoe, J. B. J. Schelen, S. van der Zwaag, D. M. de Leeuw, and W. A. Groen, *Analysis and experimental validation of the figure of merit for piezoelectric energy harvesters,* Scientific Reports (2017), under review.

[70] N. T. Mascarenhas, *Highly flexible lead-free piezoelectric composites for vibration damping and noise cancellation applications*, Master's thesis, Delft University of Technology (2015).

[71] C. R. Bowen, H. A. Kim, P. M. Weaver, and S. Dunn, *Piezoelectric and ferroelectric materials and structures for energy harvesting applications,* Energy & Environmental Science **7**, 25 (2014).

[72] M. Matsubara, T. Yamaguchi, K. Kikuta, and S.-I. Hirano, *Effect of Li substitution on the piezoelectric properties of potassium sodium niobate ceramics,* Japanese Journal of Applied Physics **44**, 6136 (2005).

[73] Y. Wang, D. Damjanovic, N. Klein, E. Hollenstein, and N. Setter, *Compositional inhomogeneity in Li- and Ta-modified (K,Na)*NbO_3 *ceramics,* Journal of the American Ceramic Society **90**, 3485 (2007).

[74] D. Liu, H. Du, F. Tang, F. Luo, D. Zhu, and W. Zhou, *Effect of heating rate on the structure evolution of* $(K_{0.5}Na_{0.5})NbO_3$–$LiNbO_3$ *lead-free piezoelectric ceramics,* Journal of Electroceramics **20**, 107 (2007).

[75] Y. Wang, D. Damjanovic, N. Klein, and N. Setter, *High-temperature instability of Li- and Ta-Modified (K,Na)*NbO_3 *piezoceramics,* Journal of the American Ceramic Society **91**, 1962 (2008).

[76] X. Vendrell, J. García, F. Rubio-Marcos, D. Ochoa, L. Mestres, and J. Fernández, *Exploring different sintering atmospheres to reduce nonlinear response of modified KNN piezoceramics,* Journal of the European Ceramic Society **33**, 825 (2013).

[77] K. Han, A. Safari, and R. E. Riman, *Colloidal processing for improved piezoelectric properties of flexible 0-3 ceramic-polymer composites,* Journal of the American Ceramic Society **74**, 1699 (1991).

[78] D. M. Reed, T. T. Srinivasan, Q. C. Xu, and R. E. Newnham, *Effect of particle size on the dielectric and piezoelectric properties of* $PbTiO_3$*-polymer composites,* in *IEEE 7th International Symposium on Applications of Ferroelectrics* (IEEE, 1990) pp. 324–327.

[79] A. S. Karapuzha, N. K. James, S. van der Zwaag, and W. A. Groen, *On the use of non-MPB lead zirconium titanate (PZT) granules for piezoelectric ceramic–polymer sensorial composites,* Journal of Materials Science: Materials in Electronics **27**, 9683–9689 (2016).

[80] J. Khaliq, D. B. Deutz, J. A. C. Frescas, P. Vollenberg, T. Hoeks, S. van der Zwaag, and P. Groen, *Effect of the piezoelectric ceramic filler dielectric constant on the piezoelectric properties of PZT-epoxy composites,* Ceramics International **43**, 2774 (2017).

[81] T. Holland and S. Redfern, *Unit cell refinement from powder diffraction data: The use of regression diagnostics,* Mineralogical Magazine **61**, 65 (1997).

[82] K. Wang, J.-F. Li, and N. Liu, *Piezoelectric properties of low-temperature sintered Li-modified (Na,K)NbO$_3$ lead-free ceramics,* Applied Physics Letters **93**, 092904 (2008).

[83] T. Gururaja, W. Schulze, L. Cross, R. Newnham, B. Auld, and Y. Wang, *Piezoelectric composite materials for ultrasonic transducer applications. Part I: Resonant rod-polymer composites,* IEEE Transactions on Sonics and Ultrasonics **SU-32**, 481 (1985).

[84] T. B. Jones, *Electromechanics of particles* (Cambridge University Press, 1995).

[85] M. Gutiérrez, H. Khanbareh, and S. van der Zwaag, *Computational modeling of structure formation during dielectrophoresis in particulate composites,* Computational Materials Science **112**, 139 (2016).

[86] L. Pardo, J. Mendiola, and C. Alemany, *Theoretical treatment of ferroelectric composites using Monte Carlo calculations,* Journal of Applied Physics **64**, 5092 (1988).

[87] E. A. Dijkstra, *Ultrasonic distance detection in spinal cord stimulation,* Ph.D. thesis, University of Twente (2003).

[88] J. F. Tressler, S. Alkoy, and R. Newnham, *Piezoelectric sensors and sensor materials,* Journal of Electroceramics **2**, 257 (1998).

[89] K. Uchino, *Introduction to Piezoelectric Actuators and Transducers,* International Center for Actuators and Transducers, Pennsylvania State University , 40 (2003).

[90] H. A. Sodano, D. J. Inman, and G. Park, *A review of power harvesting from vibration using piezoelectric materials (2003-2006),* The Shock and Vibration Digest **36**, 197 (2004).

[91] I. Graz, M. Krause, S. Bauer-Gogonea, S. Bauer, S. P. Lacour, B. Ploss, M. Zirkl, B. Stadlober, and S. Wagner, *Flexible active-matrix cells with selectively poled bifunctional polymer-ceramic nanocomposite for pressure and temperature sensing skin,* Journal of Applied Physics **106** (2009).

[92] C. Rendl, P. Greindl, M. Haller, M. Zirkl, B. Stadlober, and P. Hartmann, *PyzoFlex: Printed piezoelectric pressure sensing foil,* in *Piezoelectricity: Evolution and Future of a Technology* (2012) pp. 509–518.

[93] M. C. Araújo, C. Costa, and S. Lanceros-Méndez, *Evaluation of dielectric models for ceramic/polymer composites: Effect of filler size and concentration,* Journal of Non-Crystalline Solids **387**, 6 (2014).

[94] A. Jain, K. J. Prashanth, A. K. Sharma, A. Jain, and P. N. Rashmi, *Dielectric and piezoelectric properties of PVDF-PZT composites: A review,* Polymer Engineering and Science **55**, 1589 (2015).

[95] C. K. Wong and F. G. Shin, *Role of interfacial charge in the piezoelectric properties of ferroelectric 0-3 composites,* Journal of Applied Physics **97**, 1 (2005).

[96] M. Cakmak, S. Batra, and B. Yalcin, *Field assisted self-assembly for preferential through thickness ("Z-direction") alignment of particles and phases by electric, magnetic, and thermal fields using a novel roll-to-roll processing line,* Polymer Engineering & Science **55**, 34 (2015).

[97] H. Khanbareh, *Expanding the functionality of piezo-particulate composites*, Ph.D. thesis, Delft University of Technology (2016).

[98] D. A. van den Ende, S. E. van Kempen, X. Wu, W. A. Groen, C. A. Randall, and S. van der Zwaag, *Dielectrophoretically structured piezoelectric composites with high aspect ratio piezoelectric particle inclusions,* Journal of Applied Physics **111**, 124107 (2012).

[99] F. A. Rueggeberg, *State-of-the-art: Dental photocuring–A review.* Dental materials **27**, 39 (2011).

[100] J. G. Leprince, W. M. Palin, M. A. Hadis, J. Devaux, and G. Leloup, *Progress in dimethacrylate-based dental composite technology and curing efficiency,* Dental materials : official publication of the Academy of Dental Materials **29**, 139 (2013).

[101] C. Park and R. E. Robertson, *Aligned microstructure of some particulate polymer composites obtained with an electric field,* Journal of Materials Science **33**, 3541 (1998).

[102] A. R. Von Hippel, *Dielectrics and Waves* (John Wiley and Sons, New York, USA, 1954).

[103] D. A. van den Ende, H. J. van de Wiel, W. A. Groen, and S. van der Zwaag, *Direct strain energy harvesting in automobile tires using piezoelectric PZT-polymer composites,* Smart Materials and Structures **21**, 015011 (2012).

[104] M. Kim, J. Dugundji, and B. L. Wardle, *Effect of electrode configurations on piezoelectric vibration energy harvesting performance,* Smart Materials and Structures **24**, 045026 (2015).

[105] F. Van Loock, *Exploring the opportunities of piezoelectric composites for shear strain-driven energy harvesting,* Master's thesis, Delft University of Technology (2014).

[106] S. R. Anton and H. A. Sodano, *A review of power harvesting using piezoelectric materials (2003–2006),* Smart Materials and Structures **16**, R1 (2007).

[107] C. Dagdeviren, B. D. Yang, Y. Su, P. L. Tran, P. Joe, E. Anderson, J. Xia, V. Doraiswamy, B. Dehdashti, X. Feng, B. Lu, R. Poston, Z. Khalpey, R. Ghaffari, Y. Huang, M. J. Slepian, and J. A. Rogers, *Conformal piezoelectric energy harvesting and storage from motions of the heart, lung, and diaphragm,* Proceedings of the National Academy of Sciences of the United States of America **111**, 1927 (2014).

[108] T. Becker, M. Kluge, J. Schalk, K. Tiplady, C. Paget, and U. Hilleringmann, *Autonomous sensor nodes for aircraft structural health monitoring,* IEEE Sensors Journal **9**, 1589 (2009).

[109] H. S. Kim, J.-H. Kim, and J. Kim, *A review of piezoelectric energy harvesting based on vibration,* International Journal of Precision Engineering and Manufacturing **12**, 1129 (2011).

[110] Y. Wang, K. Ren, and Q. M. Zhang, *Direct piezoelectric response of piezopolymer polyvinylidene fluoride under high mechanical strain and stress,* Applied Physics Letters **91**, 222905 (2007).

[111] C. Andrews, Y. Lin, H. Tang, and H. A. Sodano, *Influence of aspect ratio on effective electromechanical coupling of nanocomposites with lead zirconate titanate nanowire inclusion,* Journal of Intelligent Material Systems and Structures **22**, 1879 (2011).

[112] N. K. James, D. A. van den Ende, U. Lafont, S. van der Zwaag, and W. A. Groen, *Piezoelectric and mechanical properties of structured PZT–epoxy composites,* Journal of Materials Research **28**, 635 (2013).

[113] C. K. Wong, Y. M. Poon, and F. G. Shin, *Explicit formulas for effective piezoelectric coefficients of ferroelectric 0-3 composites,* Journal of Applied Physics **90**, 4690 (2001).

[114] V. Kulkarni, R. Ben-Mrad, S. E. Prasad, and S. Nemana, *A shear-mode energy harvesting device based on torsional stresses,* Mechatronics, IEEE/ASME Transactions on **19**, 801 (2014).

[115] J. Zhao, X. Zheng, L. Zhou, Y. Zhang, J. Sun, W. Dong, S. Deng, and S. Peng, *Investigation of a* d_{15} *mode PZT-51 piezoelectric energy harvester with a series connection structure,* Smart Materials and Structures **21**, 105006 (2012).

[116] M. H. Malakooti and H. A. Sodano, *Shear mode energy harvesting of piezoelectric sandwich beam,* in *SPIE Smart Structures and Materials+ Nondestructive Evaluation and Health Monitoring* (International Society for Optics and Photonics, 2013) pp. 86881R–86881R.

[117] H. Berger, S. Kari, U. Gabbert, R. Rodriguez-Ramos, J. Bravo-Castillero, R. Guinovart-Diaz, F. J. Sabina, and G. A. Maugin, *Unit cell models of piezoelectric fiber composites for numerical and analytical calculation of effective properties,* Smart Materials and Structures **15**, 451 (2006).

[118] Z. Hashin and S. Shtrikman, *A variational approach to the theory of the elastic behaviour of multiphase materials,* Journal of the Mechanics and Physics of Solids **11**, 127 (1963).

[119] T. Furukawa, K. Fujino, and E. Fukada, *Electromechanical properties in the composites of epoxy resin and PZT ceramics,* Japanese Journal of Applied Physics **15**, 2119 (1976).

[120] R. Hill, *Elastic properties of reinforced solids: some theoretical principles,* Journal of the Mechanics and Physics of Solids **11**, 357 (1963).

[121] M. L. Dunn and M. Taya, *Micromechanics predictions of the effective electroelastic moduli of piezoelectric composites,* International Journal of Solids and Structures **30**, 161 (1993).

[122] D. A. van den Ende, P. de Almeida, and S. van der Zwaag, *Piezoelectric and mechanical properties of novel composites of PZT and a liquid crystalline thermosetting resin,* Journal of Materials Science **42**, 6417 (2007).

[123] C. T. Sun and R. S. Vaidya, *Prediction of composite properties from a representative volume element,* Composites Science and Technology **56**, 171 (1996).

[124] H. Moulinec and P. Suquet, *A numerical method for computing the overall response of nonlinear composites with complex microstructure,* Computer Methods in Applied Mechanics and Engineering **157**, 69 (1998).

[125] G. M. Odegard, *Constitutive modeling of piezoelectric polymer composites,* Acta Materialia **52**, 5315 (2004).

[126] B. Chambion, L. Goujon, L. Badie, Y. Mugnier, C. Barthod, C. Galez, S. Wiebel, and C. Venet, *Optimization of the piezoelectric response of 0–3 composites: a modeling approach,* Smart Materials and Structures **20**, 115006 (2011).

[127] T. Mori and K. Tanaka, *Average stress in matrix and average elastic energy of materials with misfitting inclusions,* Acta metallurgica **21**, 571 (1973).

[128] Y. Lin and H. A. Sodano, *A double inclusion model for multiphase piezoelectric composites,* Smart Materials and Structures **19**, 035003 (2010).

[129] J. D. Littell, C. R. Ruggeri, R. K. Goldberg, G. D. Roberts, W. A. Arnold, and W. K. Binienda, *Measurement of epoxy resin tension, compression, and shear stress-strain curves over a wide range of strain rates using small test specimens,* Journal of Aerospace Engineering **21**, 162 (2008).

[130] Y. Motola, L. Banks-Sills, and V. Fourman, *A note on tensile testing of poled and unpoled piezoelectric ceramics,* Strain **45**, 85 (2009).

[131] S. Ghosh, K. Lee, and S. Moorthy, *Multiple scale analysis of heterogeneous elastic structures using homogenization theory and voronoi cell finite element method,* International Journal of Solids and Structures **32**, 27 (1995).

[132] V. Kouznetsova, W. A. M. Brekelmans, and F. P. T. Baaijens, *An approach to micro-macro modeling of heterogeneous materials,* Computational Mechanics **27**, 37 (2001).

[133] Z. Xia, Y. Zhang, and F. Ellyin, *A unified periodical boundary conditions for representative volume elements of composites and applications,* International Journal of Solids and Structures **40**, 1907 (2003).

[134] S. Kari, H. Berger, R. Rodriguez-Ramos, and U. Gabbert, *Numerical evaluation of effective material properties of transversely randomly distributed unidirectional piezoelectric fiber composites,* Journal of Intelligent Material Systems and Structures **18**, 361 (2006).

[135] M. A. Trindade and A. Benjeddou, *Finite element homogenization technique for the characterization of d 15 shear piezoelectric macro-fibre composites,* Smart Materials and Structures **20**, 075012 (2011).

[136] *Understanding mechanical properties of epoxies for modeling finite element analysis Epoxy Technology Inc. Technical Datasheet,* (2012).

[137] N. E. Tobaben, J. P. Domann, P. M. Arnold, and E. A. Friis, *Theoretical model of a piezoelectric composite spinal fusion interbody implant.* Journal of biomedical materials research. Part A **102**, 975 (2014).

[138] Z. Wang, J. Zhu, X. Y. Jin, W. Q. Chen, and C. Zhang, *Effective moduli of ellipsoidal particle reinforced piezoelectric composites with imperfect interfaces,* Journal of the Mechanics and Physics of Solids **65**, 138 (2014).

[139] G. Hayward, J. Bennett, and R. Hamilton, *A theoretical study on the influence of some constituent material properties on the behavior of 1-3 connectivity composite transducers,* The Journal of the Acoustical Society of America **98**, 2187 (1995).

[140] R. S. Dahiya and M. Valle, *Appendix A Fundamentals of piezoelectricity* (Springer, 2013).

[141] I. L. Guy, S. Muensit, and E. M. Goldys, *Extensional piezoelectric coefficients of gallium nitride and aluminum nitride,* Applied Physics Letters **75**, 4133 (1999).

[142] J. J. Cupal, *Dielectric, piezoelectric, and electromechanical coupling constants of zinc oxide crystals,* Proceedings of the IEEE **56**, 225 (1968).

[143] S. Muensit, G. E. M, and G. I. L, *Shear piezoelectric coefficients of gallium nitride and aluminum nitride,* Applied Physics Letters **75**, 3965 (1999).

[144] S. A. Wilson, R. P. J. Jourdain, Q. Zhang, R. A. Dorey, C. R. Bowen, M. Willander, Q. U. Wahab, M. Willander, M. A.-h. Safaa, O. Nur, E. Quandt, C. Johansson, E. Pagounis, M. Kohl, J. Matovic, B. Samel, W. van der Wijngaart, E. W. H. Jager, D. Carlsson, Z. Djinovic, M. Wegener, C. Moldovan, R. Iosub, E. Abad, M. Wendlandt, C. Rusu, and K. Persson, *New materials for micro-scale sensors and actuators: An engineering review,* Materials Science and Engineering: R: Reports **56**, 1 (2007).

[145] S. Priya and D. J. Inman, *Energy harvesting technologies* (Springer, New York, NY, USA, 2009).

[146] M. Umeda, K. Nakamura, and S. Ueha, *Analysis of the transformation of mechanical impact energy to electric energy using piezoelectric vibrator,* Japanese Journal of Applied Physics **35**, 3267 (1996).

[147] M. Ferrari, V. Ferrari, M. Guizzetti, and D. Marioli, *An autonomous battery-less sensor module powered by piezoelectric energy harvesting with RF transmission of multiple measurement signals,* Smart Materials and Structures **18**, 085023 (2009).

[148] G. Park, T. Rosing, M. D. Todd, C. R. Farrar, and W. Hodgkiss, *Energy harvesting for Structural Health Monitoring sensor networks,* Journal of Infrastructure Systems **14**, 64 (2008).

[149] M. Renaud, P. Fiorini, R. van Schaijk, and C. van Hoof, *Harvesting energy from the motion of human limbs: the design and analysis of an impact-based piezoelectric generator,* Smart Materials and Structures **21**, 049501 (2012).

[150] N. S. Schenck and J. A. Paradiso, *Energy scavenging with shoe-mounted piezoelectrics,* IEEE Micro **16**, 30 (2001).

[151] E. Lefeuvre, A. Badel, A. Benayad, L. Lebrun, C. Richard, and D. Guyomar, *A comparison between several approaches of piezoelectric energy harvesting,* Journal de Physique IV France **128**, 177 (2005).

[152] S. Roundy, P. K. Wright, and J. Rabaey, *A study of low level vibrations as a power source for wireless sensor nodes,* Computer Communications **26**, 1131 (2003).

[153] S. Priya, *Advances in energy harvesting using low profile piezoelectric transducers,* Journal of Electroceramics **19**, 167 (2007).

[154] H. W. Kim, A. Batra, S. Priya, K. Uchino, D. Markley, R. Newnham, and H. F. Hofmann, *Energy harvesting using a piezoelectric "cymbal" transducer in dynamic environment,* Japanese Journal of Applied Physics **43**, 6178 (2004).

[155] J. H. Cho, R. F. Richards, D. F. Bahr, C. D. Richards, and M. J. Anderson, *Efficiency of energy conversion by piezoelectrics,* Applied Physics Letters **89**, 104107 (2006).

[156] J. Ajitsaria, S. J. Choe, D. Shen, and J. D. Kim, *Modeling and analysis of a bimorph piezoelectric cantilever beam for voltage generation,* Smart Materials and Structures **16**, 447 (2007).

[157] A. Erturk and D. J. Inman, *An experimentally validated bimorph cantilever model for piezoelectric energy harvesting from base excitations,* Smart Materials and Structures **18**, 025009 (2009).

[158] C. Mo, J. Davidson, and W. W. Clark, *Energy harvesting with piezoelectric circular membrane under pressure loading,* Smart Materials and Structures **23**, 045005 (2014).

[159] P. J. Cornwell, *Enhancing power harvesting using a tuned auxiliary structure,* Journal of Intelligent Material Systems and Structures **16**, 825 (2005).

[160] S. Roundy and Y. Zhang, *Toward self-tuning adaptive vibration-based microgenerators,* Smart Materials, Nano-, and Micro-Smart Systems **5649**, 373 (2005).

[161] E. S. Leland and P. K. Wright, *Resonance tuning of piezoelectric vibration energy scavenging generators using compressive axial preload,* Smart Materials and Structures **15**, 1413 (2006).

[162] H. Xue, Y. Hu, and Q. M. Wang, *Broadband piezoelectric energy harvesting devices using multiple bimorphs with different operating frequencies,* IEEE Transactions on Ultrasonics, Ferroelectrics, and Frequency Control **55**, 2104 (2008).

[163] H. Sodano, D. J. Inman, and G. Park, *Generation and storage of electricity from power harvesting devices,* Journal of Intelligent Material Systems and Structures **16**, 67 (2005).

[164] D. Guyomar, G. Sebald, S. Pruvost, M. Lallart, A. Khodayari, and C. Richard, *Energy harvesting from ambient vibrations and heat,* Journal of Intelligent Material Systems and Structures **20**, 609 (2008).

[165] G. K. Ottman, H. F. Hofmann, A. C. Bhatt, and G. A. Lesieutre, *Adaptive piezoelectric energy harvesting circuit for wireless remote power supply,* IEEE Transactions on Power Electronics **17**, 669 (2002).

[166] C. D. Richards, M. J. Anderson, D. F. Bahr, and R. F. Richards, *Efficiency of energy conversion for devices containing a piezoelectric component,* Journal of Micromechanics and Microengineering **14**, 717 (2004).

[167] W.-S. Jung, M.-J. Lee, M.-G. Kang, H. G. Moon, S.-J. Yoon, S.-H. Baek, and C.-Y. Kang, *Powerful curved piezoelectric generator for wearable applications,* Nano Energy **13**, 174 (2015).

[168] R. Patel, Y. Tanaka, S. McWilliam, H. Mutsuda, and A. A. Popov, *Model refinements and experimental testing of highly flexible piezoelectric energy harvesters,* Journal of Sound and Vibration **368**, 87 (2016).

[169] R. A. Islam and S. Priya, *High-energy density ceramic composition in the system* $Pb(Zr,Ti)\,O_3$-$Pb[(Zn,Ni)_{1/3}Nb_{2/3}]O_3$, Journal of the American Ceramic Society **89**, 3147 (2006).

[170] H. K. H. Kim, S. Priya, H. Stephanou, and K. Uchino, *Consideration of impedance matching techniques for efficient piezoelectric energy harvesting,* IEEE Transactions on Ultrasonics, Ferroelectrics and Frequency Control **54**, 1851 (2007).

[171] C. H. Choi, I. T. Seo, D. Song, M. S. Jang, B. Y. Kim, S. Nahm, T. H. Sung, and H. C. Song, *Relation between piezoelectric properties of ceramics and output power density of energy harvester,* Journal of the European Ceramic Society **33**, 1343 (2013).

[172] J. Liang and W.-H. Liao, *Energy flow in piezoelectric energy harvesting systems,* Smart Materials and Structures **20**, 15005 (2011).

[173] S. Roundy, *On the effectiveness of vibration-based energy harvesting,* Journal of Intelligent Material Systems and Structures **16**, 809 (2005).

[174] K. Uchino, *Ferroelectric devices & piezoelectric actuators*, 10th ed. (DEStech Publications Inc., Lancaster, PA, USA, 2017).

[175] Q. M. Wang, X. H. Du, B. Xu, and L. Eric Cross, *Electromechanical coupling and output efficiency of piezoelectric bending actuators,* IEEE Transactions on Ultrasonics, Ferroelectrics, and Frequency Control **46**, 638 (1999).

[176] D. Damjanovic, *Stress and frequency dependence of the direct piezoelectric effect in ferroelectric ceramics,* Journal of Applied Physics **82**, 1788 (1997).

[177] N. K. James, U. Lafont, S. van der Zwaag, and W. A. Groen, *Piezoelectric and mechanical properties of fatigue resistant, self-healing PZT–ionomer composites,* Smart Materials and Structures **23**, 055001 (2014).

[178] D. Zhao, I. Katsouras, K. Asadi, W. A. Groen, P. W. M. Blom, and D. M. De Leeuw, *Retention of intermediate polarization states in ferroelectric materials enabling memories for multi-bit data storage,* Applied Physics Letters **108** (2016).

[179] M. E. Lines and A. M. Glass, *Principles and applications of ferroelectrics and related materials* (Oxford University Press, 1977).

[180] M. Stengel, N. A. Spaldin, and D. Vanderbilt, *Electric displacement as the fundamental variable in electronic-structure calculations,* Nature Physics **5**, 304 (2009).

[181] A. F. Devonshire, *CIX. Theory of barium titanate— Part II,* The London, Edinburgh, and Dublin Philosophical Magazine and Journal of Science: Series 7 **42**, 1065 (1951).

[182] R. E. Newnham, V. Sundar, R. Yimnirun, J. Su, and Q. M. Zhang, *Electrostriction: Nonlinear electromechanical coupling in solid dielectrics,* The Journal of Physical Chemistry B **101**, 10141 (1997).

[183] F. Li, L. Jin, Z. Xu, and S. Zhang, *Electrostrictive effect in ferroelectrics: An alternative approach to improve piezoelectricity,* Applied Physics Reviews **1**, 011103 (2014).

[184] F. Li, L. Jin, and R. Guo, *High electrostrictive coefficient Q_{33} in lead-free $Ba(Zr_{0.2}Ti_{0.8})O_3$-$x(Ba_{0.7}Ca_{0.3})TiO_3$ piezoelectric ceramics,* Applied Physics Letters **105**, 232903 (2014).

[185] O. Guillon, F. Thiebaud, and D. Perreux, *Tensile fracture of soft and hard PZT,* International Journal of Fracture **117**, 235 (2002).

[186] W. C. Young and R. G. Budynas, *Roark's formulas for stress and strain*, 7th ed. (McGraw-Hill, New York, NY, USA, 2002).

[187] R. C. Hibbeler, *Mechanics of materials*, SI 2nd ed. (Prentice Hall, Singapore, 2005).

ACKNOWLEDGEMENTS

> *People will forget what you said,*
> *people will forget what you did,*
> *but people will never forget how you made them feel.*
>
> Maya Angelou

After four years of fun and Friday afternoon experiments at Novel Aerospace Materials, I just can't believe that this thesis is finished. It certainly wouldn't be here without the help and encouragement of many, many people, a few of which I'd like to acknowledge here. The first is my promotor, Pim Groen. You first approached me to pursue a PhD at NovAM way back in 2012, over drinks in Toulouse. Then, and now, I feel fortunate to have been your student. From day one you've been a source of knowledge and advice. Your enthusiasm for science is contagious, and it always inspired me to delve a little deeper, try a little harder and do just... one... more... experiment. I'm grateful for your informal approach to supervision. No matter the question, you always had some idea of how we could approach it. I know I will miss our "quick experiments" trying out new ideas together in the lab and brainstorming what to do next.

Thank you, Sybrand van der Zwaag, my second promotor, for always making sure I kept an eye on my project management. You kept me from getting too detail oriented at the start, and overlooking details at the end of my PhD. I've always been struck by how quickly you give feedback on manuscripts and posters, which inspired me to treat my own students with equal respect. You set out a plan for how my PhD would go at our very first PhD meeting, and I never thought I would make it, but you know what? You were right. I am sure I will miss the carefree and fun scientific environment you set out at NovAM. Elly, thanks for opening your home to me and welcoming me into the NovAM family.

Shanta Visser, thanks for keeping me grounded, making me go outside every now and then, and making sure my two promotors always had time in their agendas for me.

Ben Schelen, thank you for helping me make the most beautiful piezometer in the world. I can't count the number of times that I sent you a last minute request to clarify some minor point of how piezoelectric signal processing should work. And you magicked the answer seemingly out of nowhere every time. I'm pretty sure you helped me fix and improve just about every tool I used in the lab. I already miss the impromptu lessons you've been giving me in circuits and signals.

Dago de Leeuw was instrumental in getting this thesis done so quickly. I showed you a graph, and we built a whole chapter around it. I'm still amazed. Thank you for giving me a last minute course in scientific writing and critical thinking. You never accepted a piecemeal or half-thought through explanation and set the bar for my work that much higher. Also, thanks for ‘concomitantly’.

Erik Tempelman, thank you for giving me the opportunity to pursue my PhD in the LTM project. Thanks to you I got to see my material (almost) make it into real product demonstrators. LTM was a wonderful experience, not least because of all the people in the consortium. Special thanks to: Eric Biermann, Bertieneke Visser, Gert van der Keuken, James Burchill, James Lamb, Mark Miodownik, Sarah Wilkes, Hanne-Louise, Menno van Rijn, Anneke Stolk and Robert Abbel for making each project meeting a real event. And for the licorice’s of the world.

Frans Oostrum, Johan Boender, Rob, Ed, Misja, Hans Weerheim, Piet Droppert, Ben Norder, Ruud Hendrikx, Dirk Wilmer, thanks for helping me with all the testing and troubleshooting and building and designing for my crazy experiments all these years.

Frederik, Neola, Vincent, Guillaume this thesis would not be here without you. It was a joy and a privilege to teach you. Now it’s your turn!

I’m pretty sure I won the officemate lottery with Martino, Jimmy, and Srikanth. I learned so much from the three of you, from project planning, through obscure cultural oddities, to the optimal number of LinkedIn friends. Thanks for the science, thanks for our impromptu office lunches and thanks for the Star Wars.

Casper, Anna, Jasper, Mitesh, Stanley, Zeljka, Slavisa, Mina, Roesbeh, Nora, Sophie-Ann, Fre, Wouter, Wouter, Hermes, Nijesh, Neena, Maria, Maarten, Mladen, Ricardo, Inga, Christian, Michiel, Hussein, Maruti, Arianna, John-Alan, Freek, Niels, Mayank, Nikos, Taylor, and everyone else who joined the NovAM coffee breaks, VriMiBo’s, Sinterklaas parties, ASM events and NovAM uitjes: Thanks for making me slow down, and relax from time to time.

Thanks Ronald Veldhuizen and Asha ten Broeke for the writing tips when I needed them most. I’ll always remember: *You don’t have to write, but you can’t do anything else!*

Dominic, Ben, Patricia, Matthijs, Rogier, Marjolein, Petertje, Hugo, Eva, Rianne, Sven, Stephanie, William, Ariane, Rik, Falko, Sietske, Maurien, Tim, Brian, Andrew, Juliana, Kinge, Eric, Arthur, Onno, Ellen, Cesar, Priscilla, Mitesh, Kajal, Jacquelien, Danjel, Kaitlin, Robin, Simone, Heiti, Mempie, Papa en Mama, bedankt voor je geduld en liefde in de laatste jaren terwijl ik egoistisch doorploegde aan mijn titel.

En Jelmer:

わたしは、あなたを愛しています

Most of all, thanks for the inspiration and ideas.
Auketau.

Curriculum Vitæ

Daniella Deutz

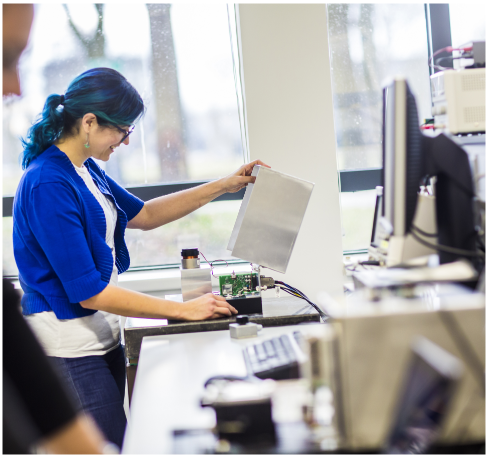

16-08-1985	Born in Charleston, South Carolina, United States of America.

Education

1997–2003	High School Buist Academy, Charleston, South Carolina, United States of America (1997) Stedelijk Gymnasium Leiden, the Netherlands (1997–2003)
2004–2013	M.Sc. in Aerospace Engineering Delft University of Technology, the Netherlands
2013–2017	Ph.D. in Aerospace Engineering Delft University of Technology, the Netherlands *Thesis:* Flexible Piezoelectric Composites *Promotor:* Prof. dr. Pim Groen *Promotor:* Prof. dr. ir. Sybrand van der Zwaag

LIST OF PUBLICATIONS

PEER REVIEWED JOURNALS

8. **D. B. Deutz**, J.-A. Pascoe, J. B. J. Schelen, S. van der Zwaag, D. M. de Leeuw and W. A. Groen, *Analysis and experimental validation of the figure of merit for piezoelectric energy harvesters*, Scientific Reports, (2017), *under review*.

7. **D. B. Deutz**, N. T. Mascarenhas, S. van der Zwaag, and W. A. Groen, *Poling piezoelectric (K,Na,Li)NbO$_3$ - polydimethylsiloxane composites*, Ferroelectrics, (2017), *in press*.

6. **D. B. Deutz**, N. T. Mascarenhas, J. B. J. Schelen, D. M. de Leeuw, S. van der Zwaag, and W. A. Groen, *Flexible piezoelectric touch sensor by alignment of lead-free alkaline niobate microcubes in PDMS*, Advanced Functional Materials, **27**(24), 1700728 (2017).

5. J. Khaliq, **D. B. Deutz**, J. A. C. Frescas, P. Vollenberg, T. Hoeks, S. van der Zwaag and P. Groen, *Effect of filler dielectric constant on the piezoelectric properties of quasi 1-3 epoxy - PZT composites and aging behaviour*, Ceramics International, **43**(2), 2774-2779 (2017).

4. **D. B. Deutz**, N. T. Mascarenhas, S. van der Zwaag, and W. A. Groen, *Enhancing energy harvesting potential of (K,Na,Li)NbO$_3$-epoxy composites via Li substitution*, Journal of the American Ceramic Society, **100**(3), 1108-1117 (2017).

3. N. K. James, **D. B. Deutz**, R. K. Bose, S. van der Zwaag, and P. Groen, *High piezoelectric voltage coefficient in structured lead-free (K,Na,Li)NbO$_3$ particulate-epoxy composites*, Journal of the American Ceramic Society, **99**(12), 3957-3963 (2016).

2. F. Van Loock, **D. B. Deutz**, S. van der Zwaag, and W. A. Groen, *Exploring the piezoelectric performance of PZT particulate-epoxy composites loaded in shear*, Smart Materials and Structures, **25**(8), 085039 (11pp) (2016).

1. **D. B. Deutz**, E. Tempelman, S. van der Zwaag, and W. A. Groen, *Piezoelectric lead zirconium titanate composite touch sensors for integration with flexible OLED technology*, Ferroelectrics, **480**(1), 1-9 (2015).

SELECTED CONFERENCE CONTRIBUTIONS

7. **D. B. Deutz**, N. T. Mascarenhas, S. van der Zwaag, W. A. Groen, *Flexible piezoelectric (K,Na,Li) NbO$_3$ polymer composites*, Joint ISAF/ECAPD/PFM Conference, Darmstadt, Germany, 21 - 25 August 2016.

6. **D. B. Deutz**, N. T. Mascarenhas, N. K. James, M. Fernandez, S. van der Zwaag, W. A. Groen, *Flexible piezoelectric composites*, Nationale Keramische Vereniging (NKV), Nijmegen, the Netherlands, 12 May 2016.

5. **D. B. Deutz**, C. A. Randall, S. van der Zwaag, W. A. Groen, *Tackling upscaling of structured piezoelectric ceramic-polymer composites*, International Conference on Electroceramics (ICE), State College, Penn State, USA, 13 - 16 May 2015.

4. **D. B. Deutz**, A. K. Shaji, N. K. James, H. Khanbareh, S. van der Zwaag, W. A. Groen, *New functional materials based on structured electroceramic composites*, International Conference on Electroceramics (ICE), State College, Penn State, USA, 13 - 16 May 2015.

3. **D. B. Deutz**, E. Tempelman, S. van der Zwaag, W. A. Groen, *Piezoelectric composite touch sensors for integration with flexible OLED technology*, International Conference on Adaptive Structures and Technologies (ICAST), The Hague, The Netherlands, 6 - 8 October 2014.

2. F. Van Loock, **D. B. Deutz**, S. van der Zwaag, W. A. Groen, *Characterization of piezoelectric composites for shear strain-driven energy harvesting applications*, International Conference on Adaptive Structures and Technologies (ICAST), The Hague, The Netherlands, 6 - 8 October 2014.

1. **D. B. Deutz**, E. Tempelman, S. van der Zwaag, W. A. Groen, *Design driven development of piezoelectric touch-sensitive luminous flexible plastics*, European Conference on Applications of Polar Dielectrics (ECAPD), Vilnius, Lithuania, 7 - 11 July 2014.